

Design and Self Assembly of Conjugated Oligomers for Electronic Device Applications

A Dissertation
Presented to the Faculty of the Graduate School
of
Yale University
in Candidacy for the Degree of
Doctor of Philosophy

by
Diana Rachel Lombardi

Dissertation Director: Prof. Mark A. Reed

May 1997

UMI Number: 9733947

**Copyright 1996 by
Lombardi, Diana Rachel**

All rights reserved.

**UMI Microform 9733947
Copyright 1997, by UMI Company. All rights reserved.**

**This microform edition is protected against unauthorized
copying under Title 17, United States Code.**

UMI
300 North Zeeb Road
Ann Arbor, MI 48103

Copyright © 1996 by Diana Rachel Lombardi

All Rights Reserved

Abstract

Design and Self Assembly of Conjugated Oligomers for Electronic Device Applications

Diana Rachel Lombardi

Yale University

1997

The primary motivation for exploring the electronic properties of polymers is the possibility of combining the processability and mechanical properties of polymers (plastics) with interesting and possibly novel electrical properties. When a carrier is transported through a conducting polymer film, it travels along the polymer chains, and between chains; the interchain component of the transport limits the bulk mobility. If one can isolate a single chain of the polymer, this component may be eliminated; thus much higher mobilities may be achieved. Ideally, one would like to place a well defined polymer chain designed for optimum electrical performance between two electrodes in complete isolation, to allow for full characterization of its electrical properties.

This thesis describes work toward the implementation of a single molecule device. The synthesis and characterization of highly specialized molecules (oligomers) is presented; data on our experimental system are discussed within the theoretical construct. The experimental system relies on a thermodynamically driven self ordering process to self assemble the long conjugated oligomers to a gold surface. The assembly has been studied to achieve the oriented arrangement of single functional molecules. Coupling and attachment of a molecule to the macroscopic world was pursued through the microfabrication of sub-10 nm gap electrodes. The process developed to deposit the difunctionalized oligomers and electrically address a single molecule is described.

Acknowledgments

I thank my advisor, Professor Mark A. Reed, for the opportunity to pursue this interdisciplinary and challenging project, and for supporting my efforts to broaden my horizons. His legacy is his 'just do it' attitude.

I thank Professor David L. Allara for allowing me to spend time in his lab at Pennsylvania State University, and for his faith in my ability to contribute to his research. I also thank his students, Tim Dunbar and Carole Mars, for their unending patience with this physicist's chemistry.

I thank Professor James Tour at the University of South Carolina for the organic compounds studied, and the support and encouragement of his students and postdoc over the years: Jay Lamba, Timothy Burgin, Darren Pearson, LeRoy Jones III.

My undying gratitude to Professor Victor Henrich (no 'd'), for his patience with this non-physics project. His direct comments kept me focused on the questions. I appreciate his time and energy, and especially his support.

Many, many thanks to Professors Robert Wheeler and Stanley Mroczkowski for being invaluable sounding boards. Their encouragement helped me to keep some perspective throughout my studies at Yale.

The following people kept things running and more importantly lent an ear above and beyond the call of duty: Arlene Ciociola, Larry Forster, Sandi Vitale.

To my friends- there are no words for all they gave me: Janice Cheung, Mark Amman, John, Deb and Jacob Huber, Alfred Kwok and his motivational meter, David Toledano,

Stephan Friedrich, Whye-Kei Lye, Maria Gherasimova, Mandar Deshpande, Gabel Chong.

To my sisters, for believing in me even when they had no idea what I was doing or why.

I thank the National Science Foundation for financial support and professional recognition, and the Defense Advanced Research Project Agency for financial support.

I dedicate this thesis to my father and mother, for teaching me the importance of truth, and for instilling in me the confidence to persevere.

Table of Contents

List of Figures	vii
List of Tables	ix
List of Abbreviations	x
1. Introduction	1
References	6
2. Conjugated Systems for Electronic Applications	7
§ 2.1 Polymers, Oligomers, and their Electronic Properties	8
§ 2.2 Optimizing Electrical Properties of Polymers	13
§ 2.3 Ethyl Substituted Thiophene Ethynylenes with Phenylthioacetate Endgroups	24
§ 2.4 Charge Transport on Oligomers	31
§ 2.5 Summary and Conclusion	34
References	37
3. Self Assembly of Thiolated Conjugated Rigid-Rod Oligomers	43
§ 3.1 Unfunctionalized TE _n Assembly	48
§ 3.2 Monofunctionalized TE _n S Assembly	58
§ 3.3 Monofunctionalized TE _n Sac Assembly	65
§ 3.4 Auger Electron Spectroscopy Data Analysis	69
§ 3.5 TE Insertion into C8	74
§ 3.6 Summary and Conclusions	78
References	80

4. Device Fabrication	82
§ 4.1 Vertical Process for <10nm Gaps	83
§ 4.2 Planar Gaps Process	97
§ 4.3 Compatibility of Microfabrication Processing and Self Assembly	104
§ 4.4 Summary and Conclusion	112
References	113
 5. Solution Depositions of Difunctionalized TE Oligomers on Microfabricated Electrodes	 114
§ 5.1 Solution Deposition of STE17S	115
§ 5.2 Summary and Conclusion	124
Reference	125
 6. Conclusion	 126
References	130

List of Figures

2.1.1	Electronic parameters for an organic molecule.	10
2.1.2	Molecular orbitals for ethane, ethylene, acetylene.	12
2.1.3	Polymers polymethylene, polyene, polyyne.	12
2.2.1	Structural conformations of polyacetylene.	14
2.2.2	Monomer and polymer of polythiophene, polyparaphenylene.	15
2.2.3	Vinylene based diblock copolymers.	17
2.2.4	Ethynylene based diblock copolymers.	21
2.2.5	Type I, II organic heterostructures.	23
2.3.1	Difunctionalized α,ω -phenyl thioacetate, β -ethyl thiophene ethynylene.	25
2.3.2	Optical absorption data for unfunctionalized oligomers.	28
2.3.3	Optical absorption maxima for (S)TE _n (S, SAc).	29
2.3.4	Optical absorption data for functionalized octamers.	30
2.4.1	Excited state structures for conjugated polymers.	33
3.1.1	Ellipsometric thickness as a function of number of rings, TE oligomers.	51
3.1.2	IR spectra from isotropic TE4 and TE4 ML.	54
3.1.3	Schematic of TE4 and IR spectra of acetylenes of TE4.	55
3.2.1	IR spectra from isotropic TE4SAc and TE4(S,SAc) ML.	62
3.4.1	Experimental AES data for S, C, Au atomic percents.	73
3.5.1	Ellipsometric thickness of C8 ML as a function of time in TEn(S) solution.	77
4.1.1	Schematic views of metal-insulator-metal multilayer for cleave process.	89
4.1.2	Photolithography masks for fabricating cleave structures.	90

4.1.4	SEM of cleaved junction showing gold tearing.	92
4.1.5	Edge-on SEM of blanket depositions showing irregular tearing.	93
4.1.6	AFM of cleaved junction; schematics of junction, AFM.	94
4.1.7	Schematic of three electrode version of cleave structure for gating.	95
4.1.8	SEM of e-beam written top electrode.	96
4.2.1	SEMs of lateral e-beam defined gap structure.	101
4.2.2	Schematic of angled deposition procedure.	102
4.2.3	E-beam lithography pattern for lateral gaps.	103
4.3.1	High frequency region of IR spectra from PR/C16 experiment.	109
4.3.2	High frequency region of IR spectra from PMMA/C16 experiment.	110
4.3.3	AES results from processing compatibility experiment.	111
5.1.1	Original version of deposition cell.	119
5.1.2	Final version of deposition cell.	120
5.1.3	Results of Raman analysis on solution after 7 day deposition.	121
5.1.4	Results of AES analysis on die after 7 day deposition.	122
5.1.5	Current as a function of time for gaps in STE17S solution.	123

List of Tables

2.1	Electronic parameters for homo-, heteropolymers.	35
2.2	Experimental optical absorption results on α,ω -phenyl thioacetate, β -ethyl thiophene ethynylene.	36
3.1.1	Experimental results from ML of TEn.	50
3.2.1	Experimental results from ML of TEnS.	60
3.3.1	Experimental results from ML of TEnSAc.	67
3.4.1	AES results for TEn(S,SAc).	72
3.5.1	Results for TEn(S) insertion into C8 ML.	76
4.3.1	Matrix of processing variations tested for effect on ML formation.	108
4.3.2	Results of AES on microfabricated die.	108

List of Abbreviations

Å	Angstrom
Ac	acetate
ACE	acetone
AES	Auger electron spectroscopy
AFM	atomic force microscopy
Ag	silver
AlO _x	aluminum oxide
AM1	Austin Model 1
Ar	argon
At %	atomic percent
Au	gold
BW	bandwidth
C	carbon
C ₂ H ₆	ethane
C ₂ H ₄	ethylene
C ₂ H ₂	acetylene
C8	octanethiol
C ₈ H ₁₇ SH	octanethiol
C16	hexadecanethiol
CB	conduction band
CH ₂	methylene or ethyl
CH ₃	methyl
cm	centimeter

cm^2/Vs	centimeter squared per Volt-second
cos	cosine
Cu	copper
Δ	delta, ellipsometric angle
d	ellipsometric thickness
DBA	donor-bridge-acceptor
DI	deionized water
DMPPV	donor methoxy poly phenylene vinylene
DPV	diphenyl vinylenes
e	natural log
EA	electron affinity
E_g	energy gap
$E(\mathbf{k})$	the dispersion relation
E_{max}	energy corresponding to first optical absorption maximum
E_{res}	resonance energy
EtOH	ethanol
eV	electron Volt
fcc	face centered cubic
fs	femtoseconds
FWHM	full width at half maximum
GAIR	grazing angle infrared
GaAs	gallium arsenide

H	hydrogen
HCl	hydrochloric acid
HOMO	highest occupied molecular orbital
Hz	Hertz
i	complex number, square root of -1
I-V	current-voltage
I	intensity
I ₀	initial intensity
IP	ionization potential
IPA	isopropyl alcohol
IR	infrared
kΩ	kilo-ohms
KBr	potassium bromide
kcal	kilocalorie
keV	kiloelectron Volts
λ	attenuation length
L	modeled molecular length
LB	Langmuir Blodgett
LUMO	lowest unoccupied molecular orbital
μl	microliter
μm	micron
MIBK	methyl isobutyl ketone
MIM	metal-insulator-metal

mm	millimeter
MO	molecular orbital
mol	mole
n	index of refraction; ratio; or integer
N ₂	nitrogen
NH ₄ OH	ammonium hydroxide
Ni	nickel
nm	nanometer
NMR	nuclear magnetic resonance
OCH ₃	methoxy
π	pi
P3MeT	β-methyl polythiophene
PA	polyacetylene
PDA	polydiacetylene
PE	polyethylene
PEt ₂ T	β,β'-ethyl polythiophene
PMe ₂ T	β,β'-methyl polythiophene
PMMA	poly methyl methacrylate
PPP	poly (p-phenylene)
PPV	poly (phenylene vinylene)
PR	photoresist
PT	polythiophene
Pt	platinum
PTE	poly (thiophene ethynylene)

PTV	poly (thiophene vinylene)
θ	theta, angle
rpm	revolutions per minute
σ_d	doped conductivity
σ_i	intrinsic conductivity
S	sulfur
SAM	self assembled monolayer
S/cm	siemens per centimeter
SCOCH ₃	thioacetate
SEM	scanning electron microscopy
Si	silicon
SiN _x	silicon nitride
SiO ₂	silicon dioxide
STM	scanning tunneling microscopy
τ	tau, time constant
$t_{ }$	intrachain transfer integral
t_{\perp}	interchain transfer integral
tan	tangent
TE _n	thiophene ethynylene n-mer
TE _n S	functionalized thiophene ethynylene n-mer
TE _n SAc	functionalized, not deprotected, thiophene ethynylene n-mer
THF	tetrahydrofuran
TMS	trimethylsilane

VB	valence band
VEH	valence effective hamiltonian
XPS	X-ray photoelectron spectroscopy
ψ	psi, ellipsometric angle
Zn	zinc
∞	infinity

"..and now reader, –bestir thyself– for though we will always lend thee proper assistance in difficult places, as we do not, like some others, expect thee to use the arts of divination to discover our meaning, yet we shall not indulge thy laziness where nothing but thy own attention is required; for thou art highly mistaken if thou dost imagine that we intended when we begun this great work to leave thy sagacity nothing to do, or that without sometimes exercising this talent thou wilt be able to travel through our pages with any pleasure or profit to thyself."

Henry Fielding

Chapter One. Introduction

Molecular electronics is not news. Electron transfer in biological systems garnered attention in the early 1940's. Organic molecules store and transport electrons and energy:¹ it is logical to explore their use for electronic device applications. An article in the October, 1979 edition of *Scientific American* reviews progress in the study of "Linear-Chain Conductors".² In 1975, a polymer called polyacetylene (PA) was obtained in the form of crystalline free-standing films with a metallic luster when a student accidentally added 1000 times the prescribed amount of catalyst to a reaction.³ The discovery that the electrical conductivity of PA can be enhanced by many orders of magnitude following doping⁴ stimulated extensive experimental studies of PA and started the renaissance of the field of conducting polymers. The primary motivation for exploring the electronic properties of polymers is the possibility of combining the processability and mechanical properties of polymers (plastics) with interesting and possibly novel electrical properties.⁵ Proposed applications for conducting polymers include rechargeable batteries, antistatic coatings, and biological and chemical sensors. The bulk of the work on polymer device applications has

been done with thin films of a particular class of polymer called conjugated for its sharing of loosely bound electrons along the polymer chains. Research areas include light emitting diodes⁶ for optical applications and field effect transistors⁷ for transport.

All conjugated polymers are semiconductors with wide band gaps (a few eV).⁸ Conductivities of a few times 10^2 S/cm have been obtained in PA;⁹ copper has a bulk conductivity of 10^5 S/cm. The higher mobilities measured in conducting polymers are of the order of 10 cm²/Vs (PA);¹⁰ mobilities in solid state devices can be 10^6 cm²/Vs. What limits the carrier's mobility in a conducting polymer film? A conducting polymer is generally composed of chain segments of varying lengths. When a carrier is transported through a conducting polymer, it travels along the chains, and between chains. These different mechanisms may be characterized by transfer integrals parallel (intrachain, $t_{||}$) and perpendicular (interchain, t_{\perp}) to the chain direction, respectively. An average value of $t_{||}$ for conducting polymers is 2.5 eV.¹¹ The value of t_{\perp} is generally an order of magnitude or more smaller.¹² The interchain component of the transport limits the bulk mobility. If one can isolate a single chain of the polymer, this component can be eliminated; thus much higher mobilities may be achieved.

The interchain - intrachain competition has been presented as a limitation to performance. It is also a limitation to the furthering of knowledge about the system. It is difficult to develop a well defined model for the various transport components based on the characteristics of disordered, multicomponent systems. It would be much more productive (and satisfying) to the scientist to isolate and fully characterize the various mechanisms independently. Ideally, one would like to create a well defined polymer chain, one designed for optimum electrical performance. This chain would be placed between two electrodes in complete isolation, to allow for full characterization of its electrical properties. The original embodiment of this single molecule construct is attributed to Aviram and

Ratner,¹³ who discussed a rectifying electronic device based on a single molecule as the active electronic element in 1974.

This thesis describes the quest for an electronic device where the active element is a single, isolated organic polymer chain. The following stages are necessary to implement this experiment: synthesis and characterization of highly specialized molecules; oriented arrangement of single functional molecules; coupling and attachment of a molecule to the macroscopic world; and electrically addressing a single molecule. The chapters of this thesis address these issues individually, in the stated order.

Chapter Two describes the design, synthesis and characterization of a conjugated molecular system for electronic applications. Quantum chemistry models are at a sufficiently sophisticated level to predict molecular electronic properties, and the impact of various design choices available to the synthetic chemist on those properties. The systematic theoretical analyses of various conjugated systems provide the tool to interpret their electronic behavior, and the understanding to iterate on the designs wisely. Organic synthetic chemistry, responsible for making the polymer systems, must be appreciated for its variable parameters, and its time-intensive process of realizing a design. Once the organic system is designed and synthesized, optical absorption studies provide information on the electron transport properties. Data on our experimental system are presented, and discussed within the theoretical construct. Expectations for electronic transport through these systems are discussed.

Various methods of assembling molecules on surfaces for electronic characterization have been explored. These include, but are not limited to: thin film formation by spin coating, Langmuir Blodgett (LB) depositions, vapor depositions, and electropolymerization. These methods all deal with bulk films. There may be ordering in the film as with the LB method, but isolating a single molecule and placing it within reach

of electrical leads requires either great luck,¹⁴ or another method. We have chosen to have the molecules spontaneously assemble by relying on a thermodynamically driven self ordering process, as described in Chapter Three. The implementation of this self assembly as designed in our experimental system relies heavily on a knowledge base that has been developed on a different system, *n*-alkanethiols on gold. While the specific driving interaction of sulfur-gold bonding is preserved in our system, there are many differences between our long conjugated rigid rod molecules, and the shorter, more labile alkanethiols which have been extensively characterized. The surface chemist appreciates the variety of factors relevant to the success of this assembly: the size of the molecule, the steric hindrance it provides to itself and its neighbors, the chain interactions that may help or hinder the endgroup assembly. All of these factors provide possible stumbling blocks to the successful self assembly of a long conjugated thiol to a gold surface. The assembly of such molecules has not been well characterized in the past. We therefore must start with the interaction of these molecules with a clean gold surface, and determine which, if any, of the characteristics of the well known *n*-alkanethiol system remain constant and which must be determined anew for the conjugated system. The orientation of the molecular adsorbate has practical implications for making a continuous contact across two electrodes, both physically and electronically.

Chapter Four describes the approach to making electrical contact to a molecule 10 nm long. Two distinct microfabrication processes are presented. The first is a vertical process that takes advantage of the nanometer-scale control of microfabrication processing. This approach has many distinct fabrication advantages; its ultimate limitation was a materials issue that led to inconsistent electrode surfaces. The second, planar, approach relies on electron-beam lithography and angled metal depositions. Sub-10 nm gaps have been consistently achieved. To confirm that the gaps microfabrication processing was not incompatible with the oligomer self assembly mechanism, a series of surface assembly

experiments similar to those described in Chapter Three were performed. Although certain fabrication processes were problematic for assembly, the processing history of the gaps did not inhibit self assembly in the gaps region.

The process developed to deposit the difunctionalized oligomers onto microfabricated gaps is described in Chapter Five. Materials issues were important in combining the constraints of microfabrication and the organic system. These gaps were electrically monitored *in situ* during the depositions; the results of the analyses of these depositions prompted the surface studies described in Chapter Three.

Chapter Six discusses applications of the infrastructure developed in this thesis work to molecular electronics, then waxes philosophical on possible future directions.

As a physicist (by training and inclination) working with electrical engineers (by affiliation) doing chemistry (out of necessity and curiosity), I caution the reader. This project is inherently multi- and interdisciplinary. I have tried to present the chemistry in comprehensible terms to the physicists and engineers, and the physics in intuitive terms for all. Regardless, thy sagacity shall not be idle... Each chapter represents work in a different field; each chapter therefore is presented in the manner appropriate to the literature of its area. The basic terms are defined. So, –bestir thyself– and remember, be it deprotonation or ionization, taking away a hydrogen atom is just that.

References

- ¹ M.A. Fox, W.E. Jones Jr., D.M. Watkins, *Chem. & Eng. News* 3/15/93, p. 38.
- ² A.J. Epstein, J.S. Miller, *Scientific American* October, 1979, p. 52.
- ³ T. Ito, H. Shirakawa, S. Ikeda, *J. Polym. Sci. Polym. Chem. Ed.* **12**, 11 (1974).
- ⁴ C.K. Chiang, C.R. Fincher, Y.W. Park, A.J. Heeger, H. Shirakawa, E.J. Louis, S. Gau, A.G. MacDiarmid, *Phys. Rev. Lett.* **39**, 1098 (1977).
- ⁵ An excellent review including applications for conducting polymers can be found in "Conjugated and Conducting Polymers" by Schott & Nechtschein in Organic Conductors J.-P. Farges, Ed. (1994, Marcel Dekker, Inc.). Another source is R.B. Kaner, A.G. MacDiarmid in *Scientific American*, Feb., 1988, p. 106.
- ⁶ J.H. Burroughs, D.D.C. Bradley, A.R. Brown, R.N. Marks, K. Mackay, R.H. Friend, P.L. Burns, A.B. Holmes, *Nature* **347**, 539-41 (1990).
- ⁷ A. Tsumura, H. Koezuka, T. Ando, *Appl Phys. Lett.* **49**, 1210-1212 (1986).
- ⁸ With the exception of SN, a semimetal: V.V. Walatka Jr., M.M. Labes, J.H. Perlstein, *Phys. Rev. Lett.* **31**, 1139-1142 (1973).
- ⁹ S. Pekker, A. Janossy, in Handbook of Conducting Polymers, T.A. Skotheim, Ed. (1986, Dekker, NY) p. 45.
- ¹⁰ H.A. Mizes, E.M. Conwell, *Phys. Rev. Lett.* **70**, 1505-1508 (1993).
- ¹¹ H.A. Mizes, E.M. Conwell, *Phys. Rev. Lett.* **70**, 1505-1508 (1993); M. Schott, M. Nechtschein, in Organic Conductors, J.-P. Farges, Ed. (1994, Dekker, NY) p. 495.
- ¹² M. Schott, M. Nechtschein, in Organic Conductors, J.-P. Farges, Ed. (1994, Dekker, NY) p. 495.
- ¹³ A. Aviram, M.A. Ratner, *Chem. Phys. Lett.* **29**, 277-283 (1974).
- ¹⁴ Luck has been exploited, in the form of carbon nanotubes dispersed in an aerosol and fortuitously precipitated onto a lithographically patterned substrate: G.M. Whitesides, C.S. Weisbecker, in Novel Forms of Carbon II (MRS, Pittsburgh, 1994).

Chapter Two. Conjugated Systems for Electronic Applications

In this chapter, the electronic properties of bulk conducting polymers and single chain oligomers are discussed. To achieve the use of a single organic molecule for electronic transport, the following are necessary: available electronic states must exist and extend throughout the molecule; once a carrier accesses these states, it must be able to travel through them without recombination; and the states must be accessible to a carrier in the metal electrode. The first two conditions will be addressed in the context of the electrical properties of the backbone. The last will be discussed with respect to the backbone-endgroup-metal interface. The basis for the formation of molecular orbitals in conjugated polymers is presented, starting with simple molecules, and extending the argument to long polymer chains. The properties of polyacetylene are presented and used to motivate arylene-based polymer and copolymer formation. A comparison is made between arylene-vinylene and arylene-ethynylene systems, based on experimental data and Valence Effective Hamiltonian pseudopotential calculations. The chemical means of controlling the electronic properties of polymer systems are briefly reviewed. Finally, the experimental system to be studied is introduced in the context of the preceding construct. Expectations for electronic transport properties are discussed in terms of the excited state of the polymer chain, and electron transfer rates. We conclude that the experimental system is not well suited to electron transport.

§ 2.1 Polymers, Oligomers, and their Electronic Properties

Polymers are synthesized by joining one molecular unit to itself a number of times. This repeated unit is the equivalent of the unit cell in the solid state; it is referred to as a monomer. Many monomers joined together form a polymer chain. The polymers used for bulk applications may be chemically or electro-chemically synthesized.¹ Due to the statistical nature of these synthetic processes, chains of varying length and morphology are usually formed. Chain synthesis may be prematurely terminated by errors in coupling, or the chains may bifurcate, or simply form with defects in their backbones. This lack of precision is a detriment to researchers trying to study their properties. Recent advances in chemical synthesis have led to precisely controlled processes that produce well defined chains.² The chemist can now produce a chain of exactly 1, 2, 3, to n repeat units; these specific products are called monomer, dimer, trimer, n -mer, etc. Chains of low molecular weight are called oligomers. The practical limit n is compound dependent; in general, n has not exceeded 20 due to solubility and process yield constraints. These processes are often time consuming due to the extensive purification required after each step, which in addition contributes to low yield. A well defined system (i.e., a system with a well defined number of repeat units) can be unambiguously characterized, and trends in behavior may be modeled. Many physical properties of conjugated oligomers vary as a function of their length. Therefore, experimental results from oligomers may be used to predict the electrical behavior of the corresponding polymers,³ and *vice versa*.

The literature contains many references to the use of band gap engineering in polymer device design, for instance to optimize carrier dynamics.⁴ The relevant electronic parameters include the energy gap (E_g), ionization potential (IP), and bandwidth (BW) (see Figure 2.1.1). For organic molecules, E_g is defined as the difference in energy between the highest occupied molecular orbital (the equivalent of the valence band, termed HOMO) and the lowest unoccupied molecular orbital (conduction band, or LUMO). Optical

absorption experiments are used to study the electronic structure of conducting polymers; the energy at which the first absorption maximum occurs is often quoted for comparison to the E_g predicted theoretically, and for comparison between polymer systems. On occasion in the literature, the onset of absorption is reported as E_g ; the onset and the first maximum can differ by 0.4 eV or more. In the case of the optical absorption measurements performed on oligomers in solvent, the molecular vibrational and rotational states give rise to fine structure in the absorption spectrum; these features are broadened by the solvent-solute interaction, and are further enhanced by the use of a polar solvent, such as that used in the experiments reported here. The assignment of the energy of the onset of absorption as the true E_g therefore is questionable.

Qualitatively, delocalization characterizes how well the valence electrons of a monomer are shared by the neighboring monomers. The electron in the HOMO/LUMO may be thought of as a wave packet propagating along the chain; delocalization characterizes the spatial extent of the wave packet. The higher the overlap of the orbitals, the better the electrons in them are shared, and the easier charge is transported along the backbone from one end to the other. The bandwidth of the HOMO is relevant as a measure of the extent of the delocalization in the system. It can also be correlated to the mobility of the carriers in the band through the effective mass, and the probability of a carrier in the band scattering. As the unit cell dimension increases, the bandwidth decreases. Bandwidths of the HOMO show a qualitative correlation to conductivities achieved in polymers upon acceptor doping.⁵ Ionization potential and electron affinity ($EA = IP - E_g$) provide the relative energy level positions for combining materials, as well as determining whether a particular dopant is capable of ionizing (or partially ionizing) a polymer chain.

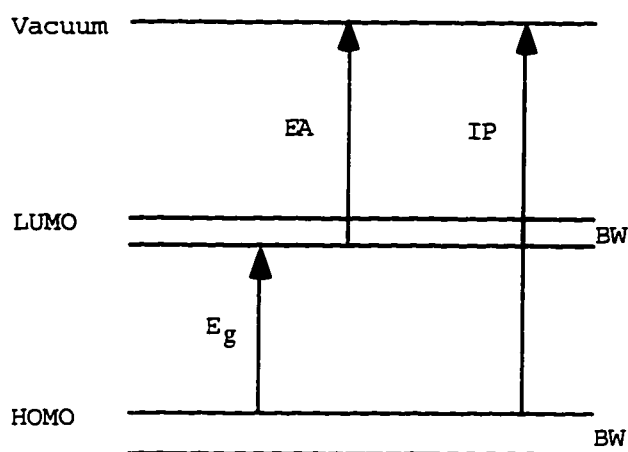


Figure 2.1.1 The relationship of IP, E_g, and EA to vacuum level is shown for an organic molecule.

The molecular orbitals (MO) of a molecule are created by the overlap of the atomic orbitals of its constituents as they are brought together in space. Carbon is the predominant element in the systems discussed; it will be used to illustrate bonding. MO's for carbon-based polymers are created by the overlap of the 2s and three 2p orbitals of the C atom. The strength of the bond is determined by the effectiveness of the overlap. The s-atomic orbitals combine head-on to form a σ MO. Sigma bond electrons are confined to the bond axis between two atoms. They are shared only by the two bonded atoms and do not contribute to delocalization. The p-atomic orbitals are oriented in the x, y, and z directions (the bond axis between atoms is defined as the x axis for this discussion). Sigma bonds may also be formed by p-type atomic orbitals meeting head-on. The π MO's are created by p-type atomic orbitals that meet side-on. The orbital overlap for π MO's is not as efficient as for σ MO's; therefore, the electrons in π orbitals are less tightly bound than those in the σ orbitals, and may be shared by neighbors along the chain from either side. When neighboring π MO's overlap on a chain, the chain is described as conjugated. A characteristic usually associated with π conjugation is a planar configuration, adopted to

maximize overlap between π atomic orbitals. The ideal conjugated chain for conduction would have wide MO's extending the length of the chain to facilitate transport of a carrier from one end to the other.

The atomic orbitals of C may be hybridized in several ways; those that create p_z orbitals available for overlap with the p_z orbitals of neighboring atoms are relevant here. To illustrate the various hybridizations of a carbon chain, compare the simple 2-carbon molecules: ethane (C_2H_6), ethylene (C_2H_4), and acetylene (C_2H_2). (See Figure 2.1.2.) In ethane, the C atom is sp^3 hybridized, leading to 4 bonding σ MO; the C has 4 single bonds. The C-C single bond distance is 1.54 Å. In ethylene, the C is sp^2 hybridized. The C=C double bond includes 1 σ and 1 π MO, and 2 σ between the C and 2 H's. The C=C double bond distance is 1.330 Å. Acetylene has a C \equiv C triple bond, and a single bond between C and H. The triple bond consists of 1 σ bond and 2 π bonds; the remaining C-H bond is a σ bond. The C \equiv C triple bond distance is 1.203 Å. The electrons in a triple bond reside closer to the nuclei, producing shorter and stronger bonds. These patterns may be extended to linear chains. A chain of single bonded C is a polymethylene; alternating single-double bonds is a polyene; and a chain of alternating single-triple bonds is polyyne (see Figure 2.1.3). Note that these are structurally derived names. The same compound may also be named for the source monomer. For example, the acetylene molecule contains a triple bonded C. Polyacetylene is a polyene, with alternating single and double bonds; its precursor is acetylene.

A comparison of E_g for each of these polymers illustrates the effect of bonding on electrical properties (see Table 2.1). For polyethylene, a particular type of polymethylene, $E_g=9$ eV; recent experimental verification has been reported based on electronic characterization of metal-molecule-metal structures.⁶ Polyacetylene (PA), a type of polyene, has a band gap of 1.8 eV. Polyyne's are predicted to have $E_g\sim 2.7$ eV.⁷ Polyethylene's bulk intrinsic conductivity is $\sigma_i=2\times 10^{-16}$ S/cm,⁸ consistent with the narrow

BW of the σ HOMO band; it is impossible to dope PE to conductivity due to its negative electron affinity.⁹ The intrinsic conductivity of bulk PA as prepared by the Shirikawa method is $\sigma_i=10^{-5}$ S/cm,¹⁰ and it has been acceptor doped to $\sigma_d=10^3$ S/cm.¹¹ A single report for bulk polyynes was found in the literature.¹² They report intrinsic conductivity of $\sigma_i=10^{-8}$ S/cm, and acceptor doped $\sigma_d=10^{-1}$ S/cm. However, the data presented are taken on a sample of stereospecifically chlorinated PA converted to polyynes by exposure to an organic strong base. It is not clear that the conversion proceeded to completion. No purification process was described. Hence the results may represent a hybrid PA/carbyne sample; they should be interpreted as an upper limit for the true value for polyynes.

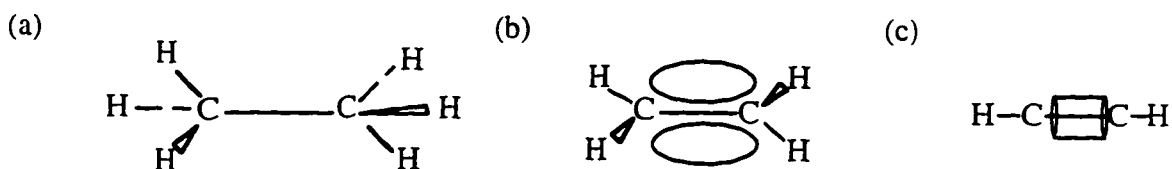


Figure 2.1.2 MO for (a) ethane, (b) ethylene, and (c) acetylene.

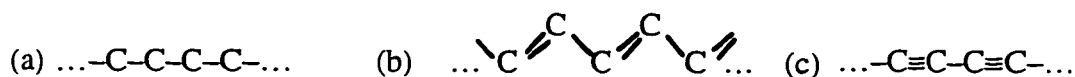


Figure 2.1.3 Polymers (a) polymethylene, (b) polyene, and (c) polyyne.¹³

§ 2.2 Optimizing Electrical Properties of Polymers

A theoretical approach that has been very successful in modeling conjugated systems and predicting their electronic structure is the Valence Effective Hamiltonian (VEH) pseudopotential method.¹⁴ This approach was developed by Nicolas and Durand¹⁵ and applied to polymers by André¹⁶ and Brédas.¹⁷ The VEH method is particularly useful for accurately predicting IP, E_g , and BW.¹⁸ The initial input into the VEH calculation is an optimized geometry, generally calculated on oligomers by the semiempirical Austin Model. AM1.¹⁹ From our discussion of bonding in simple molecules, we may appreciate the importance of the input geometry; the interatomic distances determine the orbital overlap, and therefore the bond energies. The VEH calculation is based on the use of an effective Fock operator that includes kinetic and potential energy terms. The effective atomic potentials are parametrized on simple molecules (ethane, butadiene, and acetylene for C and H; thiophene and dimethylsulfide for S) from *ab initio* calculations on their valence orbitals. This parametrization implicitly includes nuclear attraction, Coulomb repulsion and exchange. The potentials reflect the chemical environment of the atom in the polymer, rather than an isolated atom. The coefficients and 1-electron energies thus obtained are used to solve for the polymer. The output of a VEH calculation is $E(\mathbf{k})$, the dispersion relation for the band structure. From this information, the electronic parameters E_g , BW, and IP are extracted. Theoretical IP values are scaled down by 1.9 eV to correct for the polarization energy²⁰ and possible shortcomings of the model. The density of states may be constructed as well, for comparison to valence photoelectron spectra.²¹ The advantages of the VEH method are that it is completely theoretical and yields *ab initio* quality results, but needs only to evaluate single-electron integrals and is therefore much cheaper and faster than running self-consistent field approximation iterative cycles.

Polyacetylene (PA, a polyene, see Figure 2.1.3b) is the simplest conjugated backbone. There are three common structures for PA, depicted in Figure 2.2.1. The all-

trans configuration shown previously (Figure 2.1.3b) is energetically preferred; the others will be of interest to the later discussion. VEH results for PA have been reported.²² The HOMO is a broad π band originating in the C 2p_z atomic orbitals. Its calculated bandwidth is about 6 eV, while the LUMO is 6.7 eV wide. Photoelectron spectroscopy data confirm these results. The π -bands for all three configurations are almost identical in shape, width, and absolute energetic position. The conformation appears to substantially affect only the σ -electrons.²³ From the large HOMO and LUMO BW, one might expect that PA would achieve high conductivities with either n- or p-type doping; PA has been acceptor doped to 10³ S/cm, and donor doped to 10² S/cm.²⁴ The calculated E_g =1.34 eV, very close to the onset of optical absorption at 1.4 eV; experimentally, the first optical absorption maximum occurs at 1.8 eV. The low E_g and wide bandwidths of PA highly recommend it for transport applications. The major impediment to the implementation of PA-based devices is the polymer's lack of processability, and its thermal and environmental instability.

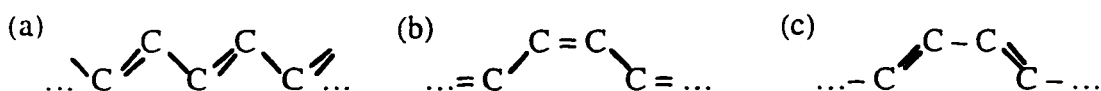


Figure 2.2.1 Various structural conformations of PA: (a) *trans*, (b) *cis-transoid*, and (c) *trans-cisoid*.

Polyenes are subject to a variety of isomerization and addition reactions. The incorporation of aromatics stabilizes the backbone while maintaining the polyene nature. Amongst the many aromatic systems available, poly(α,α' -thiophene)²⁵ (PT) and poly(*p*-phenylene)²⁶ (PPP) are discussed here; PT because it relates to the experimental system studied, and PPP due to the wealth of information available in the literature. The monomer

of PT is the heterocycle, thiophene (see Figure 2.2.2a). The monomer of PPP is the phenyl ring (see Figure 2.2.2b). Both systems retain the alternating single-double bond character of the polyene backbone; the HOMO of PT has zero coefficients on the sulfur orbitals by symmetry, although a sulfur contribution to the LUMO is predicted.²⁷ The HOMO of PT resembles the *cis*-transoid configuration of PA, shown in Figure 2.2.1b. Both PT and PPP are thermally and environmentally stable. The thiophene ring exhibits less aromaticity than the phenyl ring, as characterized by the resonance energy of the rings: for thiophene, $E_{\text{res}}=30$ kcal/mol, and phenylene, $E_{\text{res}}=40$ kcal/mol.²⁸ The charge more loosely held on the thiophene ring is available for more extensive delocalization along the backbone.²⁹ The single bond joining the rings is shorter (1.48 vs. 1.507 Å) and exhibits more π -contribution (6.4% vs. 5.3%) in bithiophene than in biphenyl.³⁰ When the thiophene rings are coupled α - β' rather than α - α' , there is no evidence of delocalization among the monomers. This behavior is evidence for the importance of the chain geometry for optimized MO overlap between monomers.

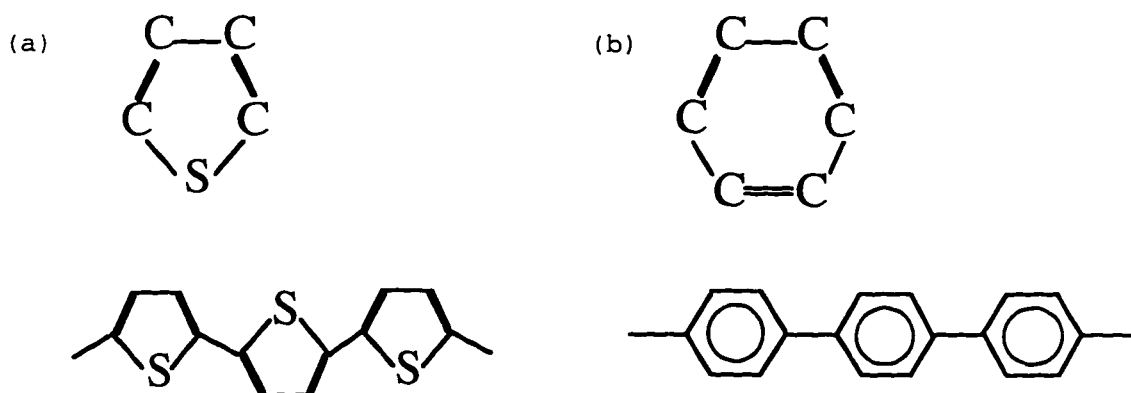


Figure 2.2.2 (a) Monomer and polymer of poly(α,α' -thiophene). (b) Monomer and polymer of poly(*p*-phenylene).

The price of stabilizing the polyene backbone via cyclization is extracted in the delocalization. Due to steric interactions of the rings' sidegroups, which may be as small as a single hydrogen atom, the rings may be forced out of planarity to reduce the

interactions. At the same time, the energy gained by the electrons being delocalized drives the backbone toward planarity. (PA will adopt a planar configuration to maximize π overlap and gain 3.7 kcal/mol in delocalization energy.) The net effect of these competing forces can be a slight twist of each ring about the single bond that joins the two rings, leading to reduced MO overlap and decreased delocalization along the chain. Each monomer is characterized by its molecular orbitals, or site energy. The extent of the overlap between sites that dictates how well the electrons are shared between neighbors may be referred to as the site-to-site energy, or transfer integral. Intuitively, as the overlap between neighboring monomers decreases (or the transfer integral decreases), the BW will decrease and E_g will increase. As a result of this torsion angle, the delocalization length saturates, i.e., the electrons are confined to a certain number of monomers despite the addition of others to the chain. The effect of torsion on the electronic properties of PPP and PT has been modeled. The ionization potential and band gap for PPP and PT are found to vary as the cosine of the rings' relative angles.³¹ The torsion angle in PPP has been measured by crystallographic methods to be 22.7° on oligomers at room temperature.³² The conjugation extends about 3-5 rings in PPP.³³ PT is predicted to favor a *trans* coplanar arrangement, with the heteroatoms alternating sides of the chain, as depicted in Figure 2.2.2a.³⁴ Experimentally, in the gas phase, steric hindrance induces a torsion angle of 30° between rings in bithiophene, although in the solid state, the molecule adopts a planar configuration.³⁵ Experimentally, the delocalization of PT saturates at about 6 rings. The incorporation of the aromatic systems increases the polymer's stability over PA, but causes the delocalization along the backbone to saturate due to steric effects.

To minimize the steric effects of neighboring rings, diblock copolymers may be made. Copolymer refers to the combination of two different monomers, A and B; diblock indicates that they are combined in the ratio of one monomer each to make the new unit cell (A+B), as opposed to, for example, combining (3A+2B) to create a unit cell. Such a combination would still be a copolymer, and may have its own particular advantages.

which will be discussed later. As long as the monomers are combined in a regular fashion, there is no localization over either moiety.³⁶ As mentioned, crystallographic data on PPP indicates a torsion angle of 22.7° between consecutive rings. If the phenyl rings are now spaced by a vinylene unit ($C=C$), the diblock copolymer is called poly (phenylene vinylene) or PPV (see Figure 2.2.3b). The experimentally determined torsion angle for PPV is $7 \pm 6^\circ$.³⁷ Calculations on the diblock copolymer poly (thiophene vinylene) (see Figure 2.2.3a) indicate that the lack of geometric steric effects allows the system to assume a planar configuration.³⁸ The torsion angle is not the only relevant parameter of the new polymer, however. The IP and E_g of the copolymer may be interpolated from the parents' values, while the upper limit of the BW is given by the lower BW of the two parent homopolymers.³⁹ In view of this, combining aromatics for stability with PA (a vinylene unit) for small E_g and large BW and IP is a logical approach. The modeled BW (HOMO-PPV)=2.3 eV, less than either of its parents'. The modeled E_g (PPV)=2.27 eV falls midway between the modeled values for PA and PPP. Experimental values for the first optical absorption maximum (E_{max}) are given in Table 2.1 along with VEH predictions for polymers of interest. The diblock copolymer that combines PT and PA, poly (thiophene vinylene) (PTV), is constructed in a similar manner. The modeled BW (HOMO-PTV)=2.5 eV, less than the parent homopolymers PA and PT. The modeled E_g for PA and PT are 1.34 eV and 1.6 eV respectively; PTV is predicted at 1.6 eV.⁴⁰ Diblock copolymer formation is successful at creating an environmentally stable conjugated polyene backbone with small E_g and minimal torsion between rings. The disadvantage is the narrowing of the HOMO band, indicative of reduced carrier mobility.

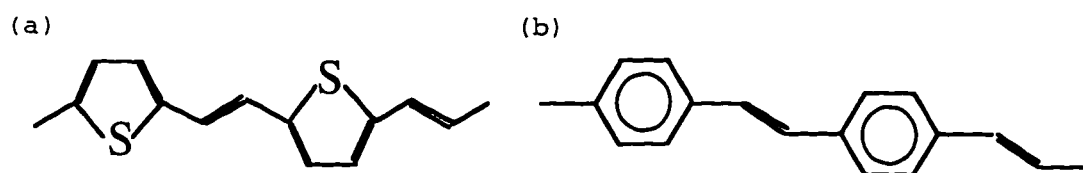


Figure 2.2.3 Diblock copolymers (a) poly (thiophene vinylene) (PTV), and (b) poly (paraphenylene vinylene) (PPV).

An alternative to the vinylene monomer for diblock copolymer formation is ethynylene, alternating single-triple bonds between C atoms. A perceived advantage to the use of a triple bond in a polymer backbone is the rigidity of the bond which may bring freedom from torsion effects, thereby enhancing delocalization. For the sake of illustration, consider first the ethylene molecule previously discussed. Each C has 2 σ bonds to its H's, and 1 σ bond in the x axis joining the C's. It also has a π bond that lies above and below the x axis, parallel to the x axis. Compare the geometry of ethylene with ethyne. A triple bonded C still has the σ bond to its neighbors (now 1 H and 1 C), and the π bond in the x direction, above and below the x axis, but it also has a π bond parallel to the x axis in front and behind the x axis. The second π bond sterically interacts with the first, lending a rigid rod nature to the backbone. The effect of the torsion angle is indeed reduced; theoretical calculations on the effect of rotation around the singly bonded C joining an acetylene to a phenyl ring predict the transfer integral between adjacent sites is reduced only by a factor of 2 with a 90° rotation⁴¹ rather than the cosine dependence seen in the homopolymer PPP. However, high conductivities have not been found for any ethynylene-based conjugated polymers.⁴²

The literature comparing the electronic behavior of ethynylenes relative to vinylenes is varied. One system studied are bridged diphenyl oligomers. In one case, the phenyl rings are bridged by vinylenes (DPV). When E_{max} is plotted as a function of n, the DPV data fall on the same line as that of H-terminated vinylene oligomers when the two phenyls are treated as equivalent to 2.7 double bonds.⁴³ This is evidence for the spatial delocalization of charge from the vinylene bridge onto the phenyl rings. A theoretical study on ethynylene bridged diphenyl oligomers indicates no difference in the bridge triple bond lengths from the presence of the phenyl rings.⁴⁴ Diffraction data on ethynylene bridged diphenyls support this conclusion.⁴⁵ Recall that the geometry of the bonds determines their electronic properties. No change in geometry indicates no substantial change in sharing of charge from isolated bonds. Electrochemical studies on alkyne-bridged phenylenediamines

show little communication between redox groups on phenyl rings separated by a dialkyne (2 consecutive triple bonds) bridge; the communication detected across the dialkyne becomes immeasurable when a phenyl is inserted between them.⁴⁶ Donor-bridge-acceptor molecules have been synthesized with porphyrins as the donor and acceptor, and polyyne and polyene spacers as the bridge. Fluorescence studies performed on these molecules with $n=0-4$ spacer repeats have indicated that electron transfer on the polyene bridge is twice as efficient as on the polyyne bridge. The transfer rate shows an exponential dependence on the distance between donor and acceptor; we may conclude that the charge transfer is via tunneling through the bridge, and that the increased efficiency of the polyene bridge may be attributed to its reduced band gap relative to the polyyne. In summary, the electrical communication across triple bond segments is less efficient than across double bond segments. This conclusion is drawn from electrochemical, optical absorption and fluorescence studies.

Diblock copolymers with a polyyne block may be constructed in the usual fashion. VEH calculations for polyyne were found in the literature: $E_g=2.7$ eV; $IP=5.5$ eV; $BW=7.3$ eV.⁴⁷ The experimental result for polyyne may be extrapolated from spectral data: $E_{max}\sim 2.17$ eV \pm .03 eV.⁴⁸ The IP may be deduced from photoelectron spectroscopy data: $IP\sim 8.50 \pm .18$ eV.⁴⁹ BW is estimated at 4.6 eV. Constructing a diblock copolymer from a thiophene monomer and a triple bond yields poly (thiophene ethynylene) or PTE (see Figure 2.2.4a). Based on the theoretical predictions, we expect its electrical properties to be: $E_g\sim 2.15$ eV, $IP\sim 5.25$ eV, $BW\leq 2.6$ eV. Experimentally $E_{max}\sim 2.7$ eV and $BW\sim 0.8$ eV.⁵⁰ The observed bandwidth for PTE should cause some concern for the efficiency of charge transfer through this state. This is supported by the data already discussed comparing sequential double bond versus triple bond bridges.

A diblock copolymer constructed from alternating vinylene ($C=C$) and ethynylene ($C\equiv C$) units is polydiacetylene (PDA, see Figure 2.2.4c). Such a construct is of interest

here because it closely resembles the backbone of an ethynylene copolymer with a smaller unit cell. Its characterization should provide information on the behavior of other ethynylene systems. VEH calculations for PDA yield $E_g=2.1$ eV, $IP=5.1$ eV, $BW=3.9$ eV.⁵¹ All parameters follow the expected trend in diblock copolymer formation. Consistent with the smaller BW, the intrinsic conductivity of PDA is less than its parents' as well: $\sigma_i \leq 10^{-12}$ S/cm. PDA is generally classified as undopable: conductivities greater than 10^{-5} S/cm have not been achieved. PDA is relatively insensitive to the effects of torsion about a single bond. As described by Brédas and Heeger,⁵² the double bond on one side remains in conjugation with the triple bond on the other as rotation about a single bond proceeds due to the cylindrical π distribution about the triple bond (see Figure 2.1.2c). Copolymer formation with PA and PDA has been explored as an avenue to heterostructures.⁵³ Although the electronic parameters have been shown to be different, the site energies have been treated as the same. The transfer integral is different to account for the transfer of p_z electrons between double and triple bonds. The low conductivity and small BW of PDA are further evidence for the unfavorable electrical properties that arise from combining double and triple bonds on a polymer chain.

The preceding experiments indicate that electron sharing through triple bonds is distinctly inferior to that through double bonds. Diblock copolymers constructed from vinylene blocks have larger BW and smaller E_g than the analogous systems constructed with ethynylenes. This may be attributed in part to the orbital mismatch of the triple bond to its neighboring monomers.⁵⁴ The electronic properties of an ethynylene based polymer indicate that it would be less advantageous than a vinylene based polymer to transport.

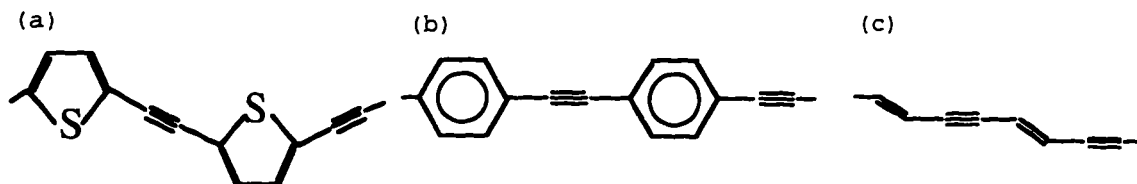


Figure 2.2.4 Ethynylene based diblock copolymers: (a) poly (thiophene ethynylene), (b) poly (phenylene ethynylene), and (c) polydiacetylene.

An additional parameter in the design of a polymer backbone is the choice of side groups on the monomer.⁵⁵ For the organic synthetic chemist, the prime motivator behind this choice may be processability; i.e., a long alkyl sidechain generally enhances the solubility of the monomer by inhibiting chain to chain interactions, and this advantage propagates through to the synthesis of longer oligomers. For heterocycles such as thiophene, a β -substituted monomer may encourage more regular polymerization by inhibiting α - β' coupling.⁵⁶ Any substitution must further be analyzed for its effect on the electrical properties of the monomer (the site energy) and by extension, the polymer. Different substituents will add (donors) or take away (acceptors) electron density from the ring. The change in electron density is reflected in the oxidation and reduction potentials of the monomers, which then extends to the ionization potential and electron affinity of the polymer, and therefore may affect the band gap. Donor groups (for example: alkyls, aminos, hydroxyls, methoxies) tend to more strongly affect the HOMO level, while acceptors (for example: halogens, nitros, CH_2Cl , CH_2Br) influence the LUMO.⁵⁷ Electron withdrawing groups decrease the electron density on the ring; as a result, the electron affinity increases, as does the ionization potential. Electron donating substituents will decrease EA and IP. For thiophene, a methyl β -substitution decreases the oxidation

potential.⁵⁸ Substituting donor methoxy (OCH₃) groups on the phenyl ring of PPV (DMPPV) results in a small (0.25 eV) reduction in E_g .⁵⁹

A substituent may also affect the delocalization through steric effects which decrease the transfer integral. X-ray studies indicate a methoxy substitution on PPV leads to a regular 3D packing, while methyl substitution leads to disordered structure.⁶⁰ The steric effects of different β -substitution on PT are seen in the E_{max} of the polymer: for P3MeT (polythiophene with a single β -substituted methyl), E_{max} =2.58 eV; for PMe₂T (PT with a double β,β' -substituted methyl), E_{max} =3.76 eV; for PEt₂T (PT with a double β,β' -substituted ethyl), E_{max} =4.43 eV.⁶¹ The change in E_{max} reflects an important loss in conjugation related to the twist of the rings along the α - α' coupling bond. The similar electronic nature of a methyl group and an ethyl group precludes this magnitude shift having a strictly site energy origin. The transfer integral may also be enhanced by substitution; certain donor-acceptor substitutions on PPV have been shown to give a rigid rod character to the molecule through the σ bond network, without strongly affecting its electrical properties.⁶² This construct may provide a favorable alternative to an ethynylene copolymer for achieving rigid rod character in a backbone without limiting the electronic properties through the triple bond characteristics.

In summary, the addition of a side group to a monomer may change the electrical properties of the polymer. The change may occur at the (monomer) site energy level through the addition or subtraction of electron density, or at the (overlap) site-to-site energy level through geometric effects which may be steric effects or changes in electron density. Substitutions may be used to enhance the electrical properties of the chain if chosen carefully.

The reliable prediction of electronic properties of a diblock copolymer from its parents' has been discussed in some detail. VEH⁶³ and Hückel⁶⁴ calculations on copolymers other than diblocks confirm that for regular arrays, E_g and IP can be linearly interpolated from the parent homopolymers. For example, a copolymer with the 3-member block phenyl-vinyl-vinyl would have E_g and IP 1/3 of the way from PA to PPP. This linear relation is indicative of the delocalization over all segments in the system. For sequences with equal parts PPP and PA but many consecutive units of either kind, localization phenomena may be expected on the units with lower IP and higher EA, in this case, on the consecutive PA units.⁶⁵ This localization has been correlated with increased charge recombination efficiency in light emitting diode structures, attributed to efficient trapping of electron-hole pairs on the sites of lower E_g and IP.⁶⁶ Bandgap engineering may also be achieved by combining monomers with different substitutions.⁶⁷ Using the tools discussed here for controlling electronic parameters, one may create the organic equivalent of type I and II superlattice devices on a single chain.⁶⁸ This concept has been amply demonstrated in the bulk⁶⁹, as already mentioned.

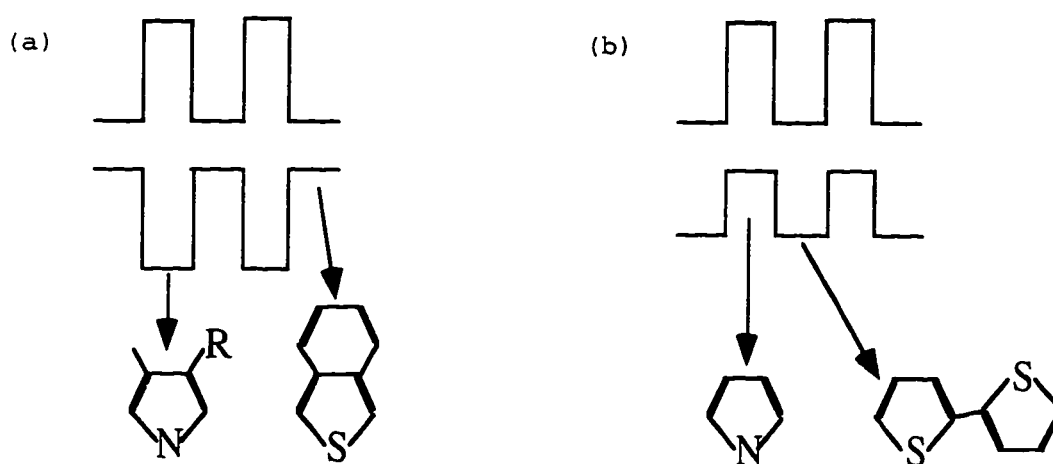


Figure 2.2.5 Band diagrams for type I (a) and II (b) heterostructures constructed from organic molecules.⁷⁰

§ 2.3 Ethyl Substituted Thiophene Ethynylenes with Phenylthioacetate Endgroups

We now have enough background to examine our experimental system. The oligomer studied is a thiophene ethynylene backbone with ethyl β -substitution on the thiophene rings (see Figure 2.3.1).⁷¹ The endgroups are phenyl thioacetates. The chemistry motivation for the endgroups will be discussed in Chapter Three on the self assembly of these molecules to gold surfaces. In this section, optical absorption experiments will be described for all length oligomers without endgroups, with one endgroup and with two endgroups – whenever samples were available. For reasons to be discussed in Chapter Three, the functionalized oligomers were treated with a base (NH_4OH) in solution to cleave the thioacetate (SCOCH_3) to a thiolate (S^-). The systems were analyzed with and without deprotecting (cleaving) the endgroup. When the oligomer was deprotected with base, the solution was neutralized with a molar equivalent of HCl before optical absorption studies in most cases. Polythiophene and its derivatives are slowly attacked by concentrated basic solutions;⁷² we may expect slow degradation of the oligomer in time. The treatment with HCl was intended to stabilize the endgroup as a thiolate and slow the base-induced degradation. The electrical parameters extracted from the optical absorption data include E_{max} and BW , and the extent of delocalization along the chain. The effect of the endgroups and substitution on the delocalization will also be described.

Optical absorption studies have been done on oligomers with $n=1, 2, 4, 8, 16$ and 17 . A variety of endgroup configurations were tested. The first optical absorption maximum and effective bandwidth (defined as the full width at half height of the absorption maximum) are shown in Table 2.2. The optical absorption data for the unfunctionalized 2, 4, and 8-mers are shown in Figure 2.3.2. E_{max} for the unfunctionalized oligomers has the expected linear relation with $1/n$, plotted in Figure 2.3.3. E_{max} for the infinite polymer is

2.65 eV, extrapolated from these data. This result is comparable to published results for a similar backbone: thiophene ethynylenes with no substitution and 1 more ring than triple bond. Experimental results on oligomers up to 5 thiophene rings yields $E_{\max}=2.69$ eV; VEH calculations predict $E_g=2.54$ eV.⁷³ A fit to data published by Tormos *et al.*⁷⁴ on the same system as Geisler *et al.* gives an extrapolated $E_{\max}=2.60$ eV. The results on our system are comparable to published results, even though the systems are different: ours has an ethyl substitution; and ours has one more triple bond than thiophene ring, while those in the literature have one more ring than triple bond.

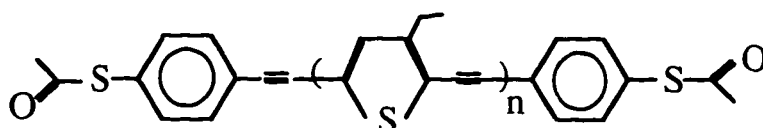


Figure 2.3.1 Difunctionalized n-mer of α,ω -phenyl thioacetate, β -ethyl thiophene ethynylene.

Optical study of the 17-mer demonstrates the localization effect of a dissimilar monomer in the backbone. Due to the synthesis process, the middle thiophene is unsubstituted. It has been established by electrochemical methods that a methyl β -substitution on the thiophene ring decreases the ionization potential of a thiophene monomer, and increases the band gap. The middle unsubstituted thiophene should look like a barrier to electrons and a well to holes. We may expect this unsubstituted ring to break up the delocalization of the backbone, and the data verify this result. The E_{\max} of the difunctionalized 17-mer is closer to the E_{\max} of the octamer (with or without endgroups) than to the 16-mer. Within a tight-binding approximation, the different electronic properties of the unsubstituted thiophene may be characterized by a different site energy than its neighbors, the ethyl β -substituted thiophenes. Site energy disorder on a molecular

chain has been predicted to reduce conductance where electron transfer would otherwise be resonant.⁷⁵

Optical absorption studies indicate that adding the phenyl thioacetate endgroup to the ethyl β -substituted thiophene ethynylene backbone does not increase the delocalization along the backbone. Figure 2.3.4 shows the optical absorption spectra for the octamer with zero, one and two endgroups. The energy of the first absorption maximum is within $\pm 1\%$ for all three oligomers. The linear relation derived from the TE_n absorption data may be used to predict E_{max} for TE_8 , TE_8S , and STE_8S . The functionalized oligomers have additional rings, phenyls, associated with the functionalization. In effect, for these oligomers, $n=9$ and 10 , if the charge on the phenyl ring were shared with the thiophene ethynylene backbone. The $E_{max}(n)$ relation predicts decreasing E_{max} for the series (2.88, 2.86, 2.84 eV); experimentally, E_{max} increases with increasing rings (2.90, 2.92, 2.93 eV). Theoretical and experimental evidence for the poor communication between phenyl and acetylene has already been discussed. The lack of a decrease in E_{max} with endgroups may further be expected from VEH calculations⁷⁶ showing that the effect of a donor on a phenyl does not propagate through to an acetylene group on the other side of the phenyl ring. The rings acts as a buffer against the π -charge transfer over the whole molecule. The delocalization on our system does not extend to the endgroups. The data show no transition in the 200-700 nm range unique to the STE_8S or TE_8S that may be attributed to the endgroup. This scenario has been treated theoretically.⁷⁷ Electron transfer for a donor-bridge-acceptor (DBA) system was modeled using a tight binding approximation. When the D/A-bridge (end-to-bridge) coupling is strong, then the wave function is delocalized along the entire molecule, and there is no decay of the D-A (end-to-end) effective coupling. If it is weak, as in our case, then the effective coupling is expected to decay exponentially with D-A distance. Based on this construct, we can expect that phenyl thioacetate

endgroups will be disadvantageous to effective coupling of a carrier in an electrode to a thiophene ethynylene backbone. We may consider our endgroups as energetic barriers to conduction from the metal to the backbone.

Data and theory indicate that the phenyl group will shield the backbone from the effects of substitution on the phenyl ring, as discussed above. If the phenyl ring were replaced by an ethyl β -substituted thiophene ring such that there were no electronic changes to disrupt the delocalization, would the thiolate bonding to the gold (S-Au) then provide a good conduit for charge transfer from the gold electrode to the thiophene ethynylene backbone? Again applying a tight-binding formalism, Mujica *et al.*⁷⁸ predict that the conductance of a molecular chain will have a strong dependence on the overlap of states between the chain and the reservoir (here, gold electrodes). If the Fermi level of the reservoir is close to the edge of the molecular orbital, the conductance will be high. We may recast this statement into the language used previously: if the transfer integral between the reservoir and the backbone is high, we may expect good electrical communication. The Au-S bond is covalent; the covalent bond indicates a high degree of charge sharing, but this bond may resemble a σ bond more than a π bond. Discrete optical transitions associated with the Au-S interface have been detected by spectroscopic ellipsometry; it is not clear whether these transitions arise from localized or delocalized states.⁷⁹ The position of these transitions relative to vacuum was not discussed. The issue of the electrical properties of the one-atom contact has been addressed in the context of scanning tunneling microscopy (STM) experiments. It is well established that the STM of molecules on a metal substrate probes electronic states formed by overlap of the molecular orbitals and the available metal states near the Fermi level.⁸⁰ For a single atom contact between metals, theoretical predictions⁸¹ and experimental results⁸² indicate a resistance of a few times 10 k Ω , depending on the atomic specie. The Au-S bond should not be this system's dominant hindrance to electronic transport.

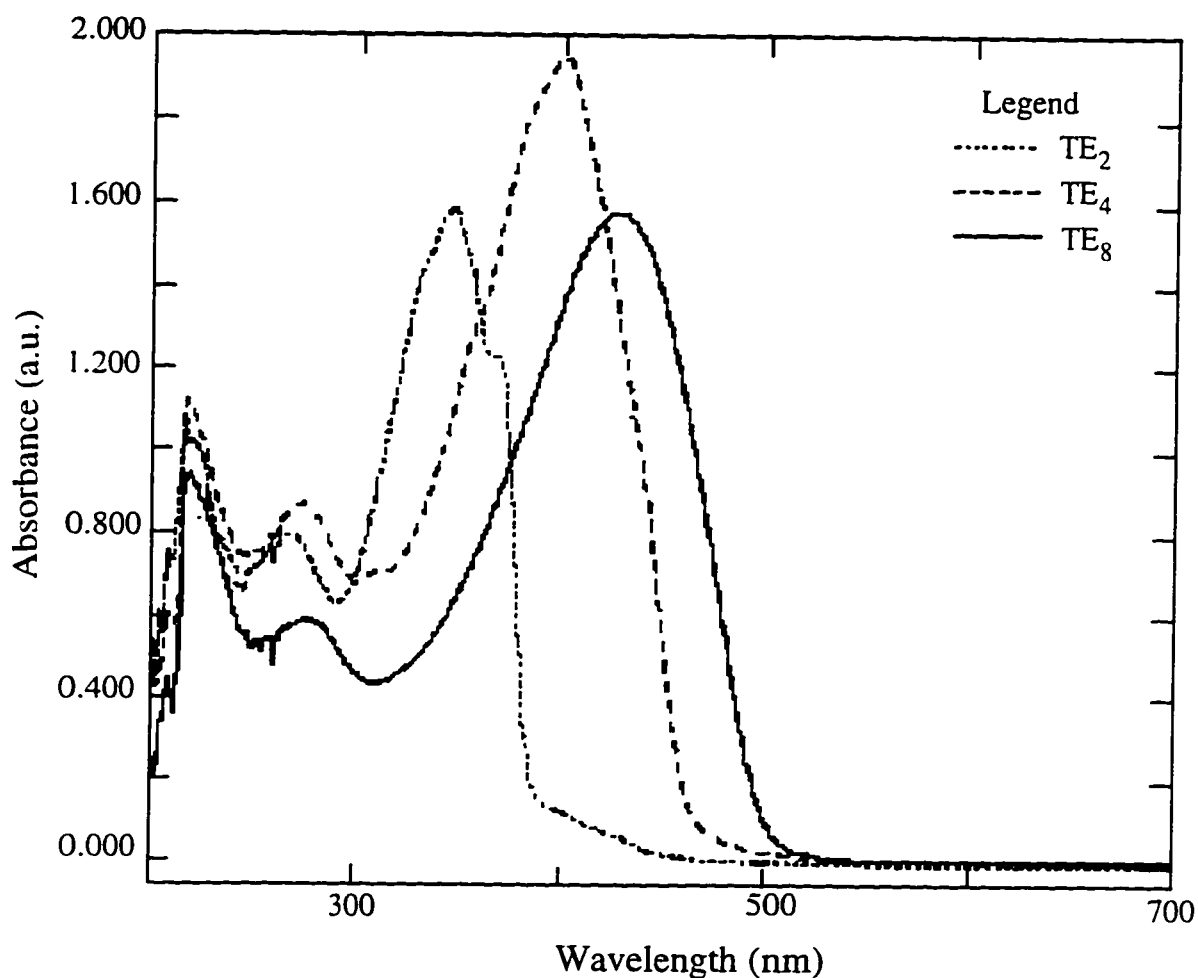


Figure 2.3.2 Optical absorption data for unfunctionalized dimer (TE₂), tetramer (TE₄), and octamer (TE₈). As the length increases, the delocalization increases, and the first optical absorption maximum shifts to lower energy. First optical absorption maxima are plotted as a function of $1/n$ (n =number of monomers) in Figure 2.3.3.

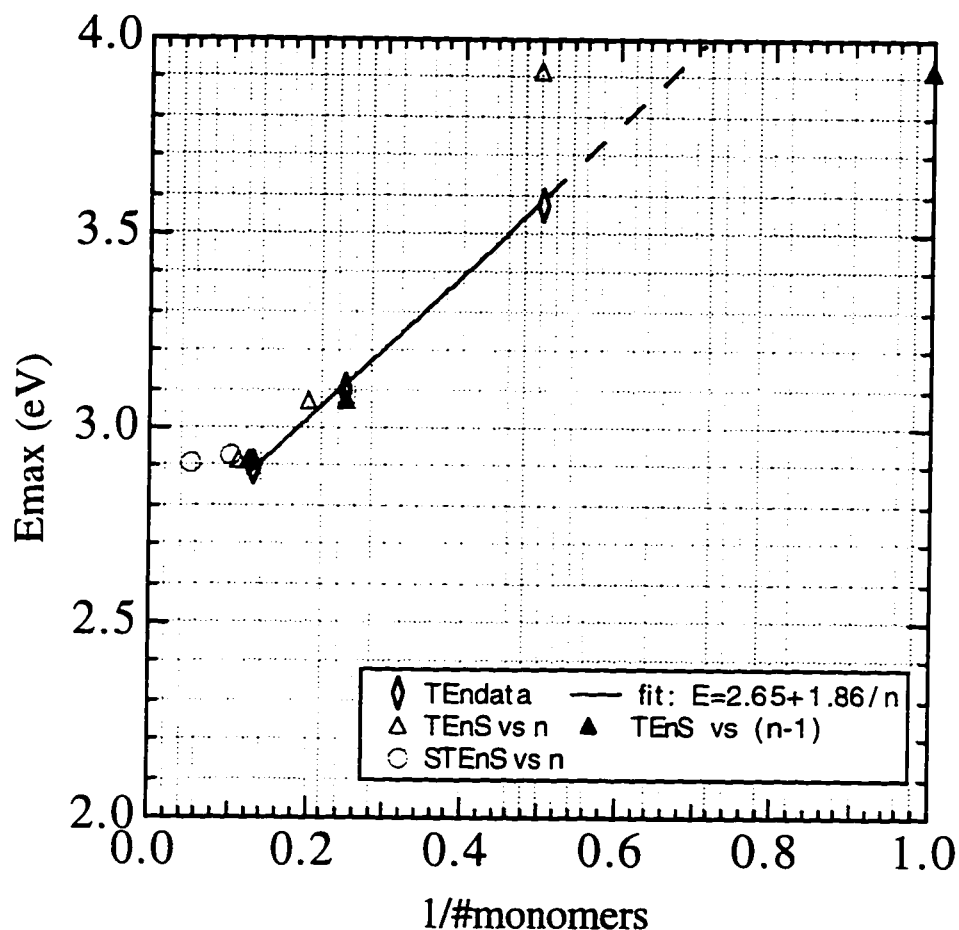


Figure 2.3.3 E_{\max} derived from optical absorption data for TE_nX . For the unfunctionalized oligomers, as the length increases, the delocalization increases, and E_{\max} decreases. The linear fit is plotted for the TE_n oligomers. Data for the monofunctionalized $TE_nS(Ac)$ are also plotted, versus the number of thiophenes in the backbone (solid markers) and versus the number of rings (thiophenes and phenylenes) (open markers). The data fall on the same line as the TE_n when n equals the number of thiophenes, indicative of poor delocalization over the phenyl rings in the endgroups. E_{\max} for the difunctionalized oligomers are plotted versus the total number of rings (open markers).

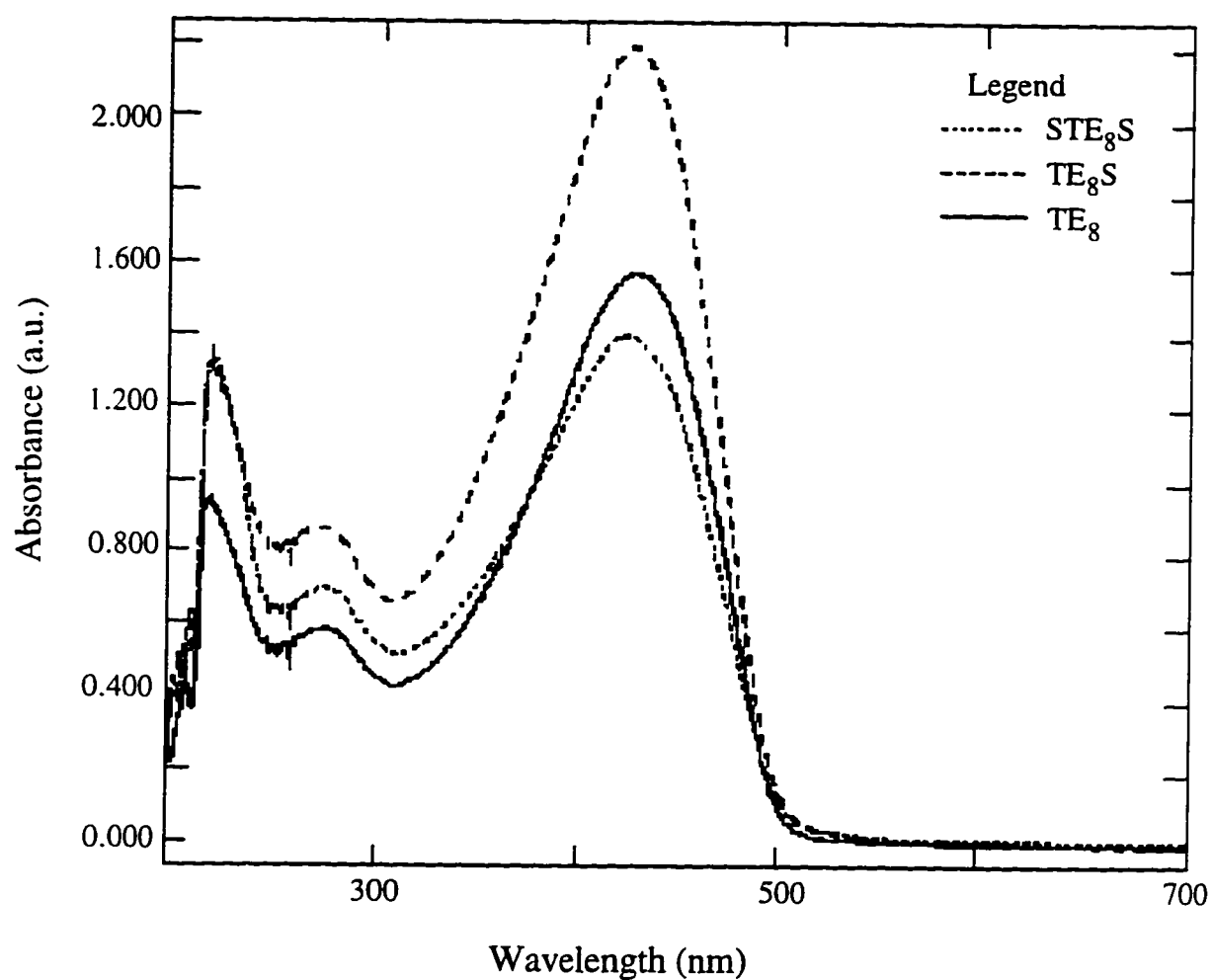


Figure 2.3.4 Optical absorption data for octamer: unfunctionalized (TE_8), monofunctionalized (TE_8S), and difunctionalized (STE_8S). As the length increases, the delocalization does not change. The electrons are not shared with the phenyl thiolate endgroups.

§ 2.4 Charge Transport on Oligomers

Conjugated polymer systems have been compared in terms of their electronic properties E_g , IP, and BW. If a charged carrier is now put onto a chain, however, there are major changes in the nuclear geometry of the chain, and hence its electronic structure. The strong response of the atomic geometry to electron excitation processes (electron-phonon coupling) is fundamental to the concept of charge transfer in organic molecules.⁸³ A single charge on a conjugated chain, together with its accompanying geometric distortion, is called a polaron. The geometric distortion associated with the excited state of an aromatic is the so-called quinoid structure (see Figure 2.4.1c). The quinoid structure has longer double bonds and shorter single bonds than its aromatic counterpart, leading to better delocalization and a more planar configuration. As a result, E_g and IP are lower, and EA is higher compared to its aromatic counterpart. PA is unique among the systems discussed here due to its degenerate ground state (see Figure 2.4.1a). The aromatic systems do not have this property. For phenylene, the energy cost to access the excited quinoid state is 0.5 eV per ring.⁸⁴ For a polyyne, the excited state is the cumulenic configuration (see Figure 2.4.1b). The energy cost for accessing this configuration is 0.34 eV per unit.⁸⁵ Evidence for the additive nature of the excitation energy over the rings involved has been presented by Beljonne *et al.*⁸⁶

The result of the changes in electronic structure associated with the polaron is a singly occupied bonding state in the energy gap just above the HOMO, and an empty antibonding state just below the LUMO. For PPP, these states are displaced into the gap by 0.2 eV each; that is, the ionization energy is lowered by 0.2 eV and the electron affinity is increased by the same amount.⁸⁷ A polaron will form when the increase in energy due to the lattice deformation is more than compensated by the lowering in ionization energy. The deformation energy is related to the spatial extent of the excitation: the more units involved in the excitation, the higher the energy cost to access the quinoid structure of each

unit (defects on a PPP chain prefer to extend over 5 rings⁸⁸). The difference in these energies corresponds to the binding energy of the polaron.⁸⁹ The additional energy cost to access the excited state must be considered when attempting to apply a simple electron-affinity model to the estimate for the energy to access the CB/LUMO of a conjugated chain. The simple band structure model no longer accurately describes the system.⁹⁰ The VEH calculations do not take into account any excited state configurations; their success at predicting E_g is thus surprising. Many of the VEH calculations address optical processes, which are much faster than electronic transport. This is the justification given for not including the excited state geometries in the calculations (together with the excellent agreement with E_{max}). Naively, one may expect that the geometric rearrangement around a charged carrier (polaron formation) would occur within a few vibrational cycles of the molecule, ~ 100 fs. It is not clear why the VEH calculations correlate so well with experimental results on E_{max} (optical absorption) and IP (valence band spectroscopy) without explicitly considering the quinoid state.

Assuming that the excited state of a thiophene ethynylene could be accessed, would the system be a good conductor? Electron transfer rates in conjugated molecules have been measured in the $10^7 - 10^9$ Hz range.⁹¹ This corresponds to currents in the picoamps range. The vibrational states of molecules are 10^{14} Hz. Obviously the molecular vibrations will have ample opportunity to interact with a carrier traversing a conjugated chain. On one hand, this geometric rearrangement is necessary for the propagation of the polaron; on the other hand, the narrow bandwidths of the ethynylene diblock copolymers may be expected to correlate with high scattering rates of carriers out of the bands, leading to recombination. Intrinsic conductivities for polyyne and PDA are low, consistent with this hypothesis. No calculations for polarons on a thiophene ethynylene chain were found in the literature, nor was experimental evidence for polarons on an ethynylene diblock copolymer, including PDA. In fact, attempts at doping PDA have resulted in very marginal increases in

conductivity ($\sigma_d \sim 10^{-6}$ S/cm). The orbital mismatch of the sp^2 - sp hybridization may be partly responsible. Note that the quinoid structure of a polyyne is harder to access than for PA. This is attributed in part to the higher spring constant of triple bond compared to the double bond. A backbone with a triple bond cannot as easily make the necessary geometric rearrangements (relaxations) into the excited state.⁹² There is no indication that this polymer system would be a good conductor.

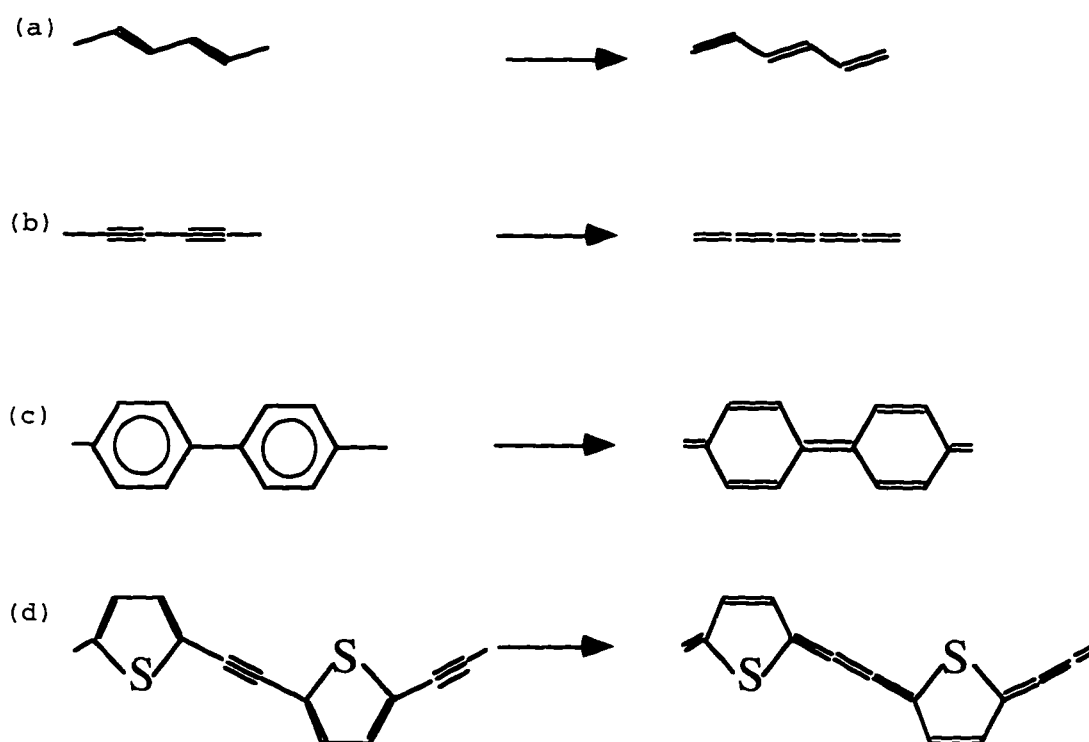


Figure 2.4.1 Excited state structure for (a) PA, (b) polyyne, (c) PPP, and (d) PTE.

§ 2.5 Summary and Conclusion

In this chapter, we have reviewed the source of conjugation in polymeric systems. The effects of monomer and substituents on the electronic properties of the polymer were described. The simple band structure model was applied to bulk film devices with success, but it failed on the single-chain level due to the strong electron phonon interaction in these systems. The VEH pseudopotential method was used to predict the electronic properties of a variety of homopolymers, and diblock copolymers constructed from them. The success of the VEH method was seen to be somewhat surprising given its lack of excited state geometry input.

Optical absorption data and theoretical calculations indicate the scenario of a thiophene ethynylene with phenyl thioacetate endgroups transporting a charge from a gold contact through the endgroup along the chain through a second endgroup to another gold contact is unlikely: the backbone wavefunction is not delocalized over the endgroup; $E_{\text{max}}=2.6$ eV, characterizing the system as an intrinsic semiconductor; attempts to dope TE oligomers have yielded no noticeable change in conductivity;⁹³ the experimentally determined bandwidth is 0.8 eV, indicative of poor mobility even if the chain were to be ionized. Unfortunately, the choice of experimental system for this thesis work was predetermined. The time scale for synthetic changes exceeded a graduate student's tenure. Not only were redesigns of the available systems impossible, but the originally conceived ultimate system, a difunctionalized 16-mer, was never realized. These limitations stem from the oligomers' difficult and time-consuming syntheses. Despite the improbability of conductivity in these systems, the development of a process to implement a molecular device from a conjugated oligomer self-assembling across a nanofabricated gap includes opportunities to develop the necessary infrastructure for a more suitable organic system, yet to be identified and synthesized.

Table 2.1. Electronic parameters for homo-, heteropolymers. The first line for every entry is the theoretical prediction, E_g ; if data were quoted (E_{\max}), they are provided in parenthesis on the second line.

polymer	IP (eV)	E_g (eV)	BW (eV)	σ_i (S/cm)	σ_d (S/cm)	ref [†]
polymethylene	vacuum	9 eV				[9]
		(9)		10^{-8}		[6]
PA	4.7	1.34	6.0			VEH
		(1.8)		10^{-8}	10^3	[10, 11]
polyyne	5.5	2.5-2.7	7.3			[47]
	(8.5 \pm .18)	(2.17 \pm .03)	(4.6)	10^{-8}	10^{-8}	[48,49]
PDA	5.1	2.1	3.9			VEH
	5.2	2.1		10^{-16} - 10^{-12}	$\leq 10^{-5}$	[18, 92]
PPP	5.5	3.9	3.2			VEH
	(5.5)	(3.4 \pm 0.2)				
PT	5.0	1.6	2.6			VEH
		(2.26)				[50]
PPV	5.1	2.3-2.5	2.3-2.8			VEH
		(2.5)				
PTV	4.9	1.6	2.5			VEH
		2.2				[18]
PPE						
PTE	6.8	1.9	< 2.6			VEH
		(2.7)	(0.8)			data

[†] VEH calculations are summarized in reference [18].

Table 2.2. Experimental optical absorption results on α,ω -phenyl thioacetate, β -ethyl thiophene ethynylenes.

Compound	E_g (eV)	BW(eV)	λ_{max} (nm)
TE1SAc	3.92	0.72 ± 0.08	316
TE1S	3.92	0.90 ± 0.30	316
AcSTE1SAc			
STE1S	3.66	1.13 ± 0.19	339
TE2	3.59	0.76 ± 0.16	345
TE2SAc	3.39	0.66 ± 0.12	366
TE2S	3.42	1.03 ± 0.39	363
AcSTE2SAc	3.20	0.87 ± 0.23	387
STE2S			
TE4	3.15	0.94 ± 0.30	395
TE4SAc	3.08	0.88 ± 0.26	403
TE4S	3.10	0.98 ± 0.32	401
AcSTE4SAc			
STE4S			
TE8	2.90	0.97 ± 0.32	427
TE8S	2.92	0.87 ± 0.23	424
STE8S	2.93	0.93 ± 0.31	423
TE16	2.85	0.79 ± 0.20	435
STE17S	2.91	0.86 ± 0.22	426

References

- ¹ W. Feast, in Handbook of Conducting Polymers, T.A. Skotheim, Ed. (Dekker, New York, 1986) p.1.
- ² J.M. Tour, *Chem. Rev.* **96**, 1 (1996).
- ³ J.L. Brédas, R. Silbey, D.S. Boudreaux, R.R. Chance, *J. Amer. Chem. Soc.* **105**, 6555-6559 (1983).
- ⁴ A.R. Brown, D.D.C. Bradley, J.H. Burroughs, R.H. Friend, N.C. Greenham, P.L. Burns, A.B. Holmes, A. Kraft, *Appl. Phys. Lett.* **61**, 2793-95 (1992).
- ⁵ J.L. Brédas, R.R. Chance, R.H. Baughman, *J. Chem. Phys.* **76**, 3673-3678 (1982).
- ⁶ C. Boulas, J.V. Davidovits, F. Rondelez, D. Vuillaume. *Phys. Rev. B* **76**, 4797-4800 (1996).
- ⁷ J.L. Brédas, R.R. Chance, Baughman, Silbey. *J. Chem. Phys.* **76**, 3673 (1982).
- ⁸ J. Brandrup, E.H. Immergut, Eds. Polymer Handbook (Wiley, New York, 1974)
- ⁹ M. Schott, M. Nechtschein, in Organic Conductors, J.-P. Farges, Ed. (1994, Dekker, NY) p. 495.
- ¹⁰ A.J. Epstein, in Handbook of Conducting Polymers, T.A. Skotheim, Ed. (Dekker, New York, 1986) p. 1041.
- ¹¹ S. Pekker, A. Jánosy, in Handbook of Conducting Polymers, T.A. Skotheim, Ed. (Dekker, New York, 1986) p. 45.
- ¹² K. Akagi, M. Nishiguchi, H. Shirakawa, Y. Furukawa, I. Harada, *Synth. Met.* **17**, 557-562 (1987).
- ¹³ Note that when four bonds are not explicit for a C atom, H atoms are understood to complete the set and may not be explicitly drawn. The C atoms at the junctions of the bonds are often "understood" as well. This notation will be used from §2.2.
- ¹⁴ For an introduction to quantum chemical calculations, see A.C. Wahl, *Sci. Am.* April 1970, p. 54.
- ¹⁵ G. Nicolas, P. Durand, *J. Chem. Phys.* **70**, 2020 (1979); **72**, 453 (1980).
- ¹⁶ J.M. André, L.A. Burke, J. Delhalle, G. Nicolas, and P. Durand, *Int. J. Quantum Chem. Symp.* **13**, 283 (1979).
- ¹⁷ J.L. Brédas, R.R. Chance, R.H. Baughman, R. Silbey, *J. Chem. Phys.* **76**, 3673-3678 (1982) .

- 18 J.L. Brédas, in Handbook of Conducting Polymers, T.A. Skotheim, Ed. (Dekker, New York, 1986) p. 859.
- 19 M.J.S. Dewar, E.G. Zoebish, R.F. Healy, J.J.P. Stewart, *J. Amer. Chem. Soc.* **107**, 3902 (1985).
- 20 The presence of other chains in the solid state makes it easier to extract an electron from a given chain than in the gas phase. Experimentally, the difference is 1.5-2.0 eV in hydrocarbon compounds. [see ref 30.]
- 21 M. Logdlund, W.R. Saleneck, F. Meyers, J.L. Brédas, G.A. Arbuckle, R.H. Friend, A.B. Holmes, G. Froyer, *Macromolecules* **26**, 3815-20 (1993).
- 22 M. Logdlund, W.R. Saleneck, F. Meyers, J.L. Brédas, G.A. Arbuckle, R.H. Friend, A.B. Holmes, G. Froyer, *Macromolecules* **26**, 3815-20 (1993).
- 23 J.L. Brédas, R.R. Chance, R. Silbey, G. Nicolas, Ph. Durand, *J. Chem. Phys.* **75**, 255-267 (1981).
- 24 M. Schott, M. Nechtschein, in Organic Conductors, J.-P. Farges, Ed. (1994, Dekker, NY) p. 502.
- 25 For heterocycles, α coupling refers to a bond to the C nearest the heteroatom (in thiophene, the S). β coupling then, refers to the C between 2 other C.
- 26 For disubstituted phenyl rings, substitutions opposite each other (separated by 2 C) are denoted *para*; those separated by a single C are denoted *meta*, and neighboring substituents are *ortho*.
- 27 J.L. Brédas, *J. Chem. Phys.* **82**, 3808-3811 (1985).
- 28 Hartough, Ed. Heterocyclic Compounds: Thiophene and its Derivatives (1952) and references therein.
- 29 Z. Shuai, J.L. Brédas, *Phys. Rev. B* **46**, 4395 (1992).
- 30 J.L. Brédas, G.B. Street; B. Thémans, J.M. André, *J. Chem. Phys.* **83**, 1323-1329 (1985).
- 31 J.L. Brédas, G.B. Street; B. Thémans, J.M. André, *J. Chem. Phys.* **83**, 1323-1329 (1985).
- 32 L.W. Shacklette, H. Eckhardt, R.R. Chance, G.G. Miller, D.M. Ivory, R.H. Baughman, *J. Chem. Phys.* **73**: 4098 (1980); L.W. Shacklette, R.R. Chance, D.M. Ivory, G.G. Miller, R.H. Baughman, *Synth. Met.* **1**, 307 (1980).
- 33 G.E. Wnek, in Handbook of Conducting Polymers, T.A. Skotheim, Ed. (Dekker, New York, 1986) p. 205; also, extracted from data presented in ref 3.

- 34 J.L. Brédas, G.B. Street; B. Thémans, J.M. André, *J. Chem. Phys.* **83**, 1323-1329 (1985).
- 35 D. Beljonne, Z. Shuai, J.L. Brédas, *J. Chem. Phys.* **99**, 8819-8828 (1993) and references therein.
- 36 J.L. Bredas, M. Dory, B Themans, J Delhalle, JM Andre, *Synth. Met.* **28**, D533-542 (1989); R. Ruckh, E. Sigmund, C. Kollmar, H. Sixl, *J. Chem. Phys.* **85**, 2797-801 (1986).
- 37 M. Logdlund, W.R. Saleneck, F. Meyers, J.L. Bredas, G.A. Arbuckle, R.H. Friend, A.B. Holmes, G. Froyer, *Macromolecules* **26**, 3815-20 (1993).
- 38 Z.-F. Ding, C.-R. Wu, Y.-M. Sun, J.-Z. Liu, *Chem. Phys.* **175**, 283-288 (1993).
- 39 J.L. Brédas, M. Dory, B. Thémans, J. Delhalle, J.M. Andre, *Synth. Met.* **28**, D533-542 (1989).
- 40 J.L. Brédas, R.L. Elsenbaumer, R.R. Chance, R. Silbey, *J. Chem. Phys.* **78**, 5656-5662 (1983).
- 41 Barzoukas, *Chem. Phys.* **153**, 457 (1991).
- 42 D. Ofer, T.M. Swager, M.S. Wrighton, *Chem. Mater.* **7**, 418-425 (1995) and references therein.
- 43 J.L. Bredas, R. Silbey, D.S. Boudreaux, R.R. Chance. *J. Amer. Chem. Soc.* **105**, 6555-6559 (1983).
- 44 C. Dehu, F. Meyers, J.L. Bredas, *J. Amer. Chem. Soc.* **115**, 6198-6206 (1993).
- 45 E.M. Graham, V.M. Miskowski, J.W. Perry, D.R. Coulter, A.E. Steigman, W.P. Schaefer, R.M. Marsh, *J. Amer. Chem. Soc.* **111**, 8771-8779 (1989).
- 46 Q. Zhou, T.M. Swager, *J. Org. Chem.* **60**, 7096-7100 (1995).
- 47 J.L. Brédas, R.R. Chance, R.H. Baughman, *J. Chem. Phys.* **76**, 3673-3678 (1982).
- 48 R. Eastmond, T.R. Johnson, D.R.M. Walton, *Tetrahedron* **28**, 4601-4616 (1972).
- 49 M. Allan, E. Heilbronner, E. Kloster-Jensen, J.P. Maier, *Chem. Phys. Lett.* **41**, 228-230 (1976).
- 50 T. Geisler, J.C. Petersen, T. Bjornholm, E. Fischer, J. Larsen, C. Dehu, J.L. Brédas, G.V. Tormos, P.N. Nugara, M.P. Cava, R.M. Metzger, *J. Phys. Chem.* **98**, 10102-10111 (1994).
- 51 J.L. Brédas, in Handbook of Conducting Polymers, T.A. Skotheim, Ed. (Dekker, New York, 1986) p. 859.

- 52 J.L. Brédas, A.J. Heeger, *Macromolecules* **23**, 1150-1156 (1990).
- 53 R. Ruckh, E. Sigmund, C. Kollmar, H. Sixl, *J. Chem. Phys.* **85**, 2797-2801 (1986).
- 54 J.M. Tour, private communication.
- 55 For a discussion of the methods for tailoring polymer properties including backbone and side chain choices, see H.R. Allcock, *Science* **255**, 1106-1112 (1992).
- 56 G. Tourillon, in Handbook of Conducting Polymers, T.A. Skotheim, Ed. (Dekker, New York, 1986) p. 298.
- 57 expt.: J. Cornil, D.A. dos Santos, D. Beljonne, J.L. Brédas, *J. Phys. Chem.* **99**, 5604-5611 (1995); theory: ref 3.
- 58 J. Bargon, S. Mohmand, R.J. Waltman, *IBM J. Res. Develop.* **27**, 330-341 (1983).
- 59 F. Meyers, A.J. Heeger, J.L. Brédas, *J. Chem. Phys.* **97**, 2750-2758 (1992).
- 60 Martens, *Synth. Met.* **41**, 301 (1991).
- 61 G. Tourillon, in Handbook of Conducting Polymers, T.A. Skotheim, Ed. (Dekker, New York, 1986) p. 306, 313, 315.
- 62 J. Cornil, D.A. dos Santos, D. Beljonne, J.L. Brédas, *J. Phys. Chem.* **99**, 5604-5611 (1995).
- 63 J.L. Brédas, M. Dory, B. Thémans, J. Delhalle, JM André, *Synth. Met.* **28**, D533-542 (1989).
- 64 R. Ruckh, E. Sigmund, C. Kollmar, H. Sixl, *J. Chem. Phys.* **85**, 2797-801 (1986).
- 65 F. Meyers, A.J. Heeger, J.L. Brédas, *J. Chem. Phys.* **97**, 2750-2758 (1992).
- 66 P.L. Burn, A.B. Holmes, A. Kraff, D.D.C. Bradley, A.R. Brown, R.H. Friend, R.W. Gymer, *Nature* **356**, 47 (1992).
- 67 D.A. dos Santos, C. Quattrocchi, R.H. Friend, J.L. Brédas, *J. Chem Phys.* **100**, 3301-3306 (1994); T. Yoshimura, S. Tatsuura, W. Sotoyama, A. Matsuura, T. Hayano, *Appl. Phys. Lett.* **60**, 268-270 (1992).
- 68 For example, T. Shimidzu, in Molecular Electronics-Science and Technology, A. Aviram, Ed. (AIP, 1992) p. 129.
- 69 Y. Ohmori, A. Fujii, M. Uchida, C. Morishima, K. Yoshino, *Appl. Phys. Lett.* **62**, 3250-3252 (1993).

- 70 T. Shimidzu, in Molecular Electronics-Science and Technology, A. Aviram , Ed.(AIP, 1192) p. 129.
- 71 up to 50Å: D.L. Pearson, J.S. Schumm, L. Jones II. J.M. Tour, *Polym. Prepr.* **35**, 202-203 (1994).
- 72 G. Tourillon, in Handbook of Conducting Polymers, T.A. Skotheim, Ed. (Dekker, New York, 1986) p.306.
- 73 T. Geisler, J.C. Petersen, T. Bjornholm, E. Fischer, J. Larsen, C. Dehu, J.L. Brédas, G.V. Tormos, P.N. Nugara, M.P. Cava, R.M. Metzger, *J. Phys. Chem.* **98**, 10102-10111 (1994).
- 74 G.V. Tormos, P.N. Nugara, M.V. Lakshmikantham, M.P. Cava. *Synth. Met.* **53**, 271-281 (1993).
- 75 M. Kemp, V. Mujica, M.A. Ratner, *J. Chem. Phys.* **101**, 5172-5178 (1994).
- 76 C. Dehu, F. Meyers, J.L. Brédas, *J. Amer. Chem. Soc.* **115**, 6198-6206 (1993).
- 77 J.W. Evenson, M. Karplus, *J. Chem. Phys.* **96**, 5272-78 (1992).
- 78 V. Mujica, M. Kemp, M.A. Ratner, *J. Chem. Phys.* **101**, 6856-6864 (1994).
- 79 J. Shi, B. Hong, A.N. Parikh, R.W. Collins, D.L. Allara, *Chem. Phys. Lett.* **246**, 90-94 (1995).
- 80 V.M. Hallmark, S. Chiang, K.-P. Meinhardt, K. Hafner, *Phys. Rev. Lett.* **70**, 3740-3743 (1993); J. Tersoff, D.R. Hamann, *Phys. Rev. B* **31**, 805-813 (1985).
- 81 N.D. Lang, *Phys. Rev. B* **36**, 8173-8175 (1987).
- 82 J.K. Gimzewski, R. Möller, *Phys. Rev. B* **36**, 1284 (1987).
- 83 J.L. Brédas, R.R. Chance, R. Silbey, *Phys. Rev. B* **26**, 5843 5854 (1982).
- 84 J.L. Brédas, R.R. Chance, R. Silbey, *Phys. Rev. B* **26**, 5843-5854 (1982).
- 85 A. Karpfen, *J. Phys. C* **12**, 3227-37 (1979).
- 86 D. Beljonne, Z. Shuai, J.L. Brédas, *J. Chem. Phys.* **98**, 8819-8828 (1993).
- 87 J.L. Brédas, R.R. Chance, R. Silbey, *Phys. Rev. B* **26**, 5843-5854 (1982).
- 88 J.L. Brédas, R.R. Chance, R. Silbey, *Phys. Rev. B* **26**, 5843-5854 (1982).
- 89 J.L. Brédas, *Phys. Rev. B* **30**, 1023-1025 (1984).

- ⁹⁰ J.L. Brédas, R.R. Chance, R. Silbey, *J. Phys. Chem.* **85**, 756-758 (1981).
- ⁹¹ B. Paulson, K. Pramod, P. Eaton, G. Closs, J.R. Miller, *J. Phys. Chem.* **97**, 13042-13045 (1993); A. Osuka, N. Tanabe, S. Kawabata, I. Yamazaki, Y. Nishimura, *J. Org. Chem.* **60**, 7177-7185 (1995).
- ⁹² K. Tanaka, M. Okada, T. Koike, T. Yamabe, *Synth. Met.* **31**, 181-190 (1989).
- ⁹³ G.V. Tormos, P.N. Nugara, M.V. Lakshmikantham, M.P. Cava, *Synth. Met.* **53**, 271-281 (1993).

Chapter Three. Self Assembly of Thiolated, Conjugated Rigid Rod Oligomers

The ultimate goal of this project is to achieve the configuration of a single molecule connected between two electrodes. Once a suitable molecule is designed and fabricated,¹ its surface arrangement properties must be determined to enable its controlled placement between the small electrodes.² In an ideal world, the engineer could prefabricate electrodes on a substrate and submerge it into a beaker of solvent containing the molecules; upon removing the substrate and rinsing, *voila!*, molecules would have placed *themselves* across the electrodes *in* the appropriate orientation *and* firmly attached. Are we asking too much?

The "spontaneous association of molecules under equilibrium conditions into stable, structurally well-defined aggregates joined by non-covalent bonds",³ a process known as molecular self assembly, is quite common in biological systems. Self assembly is a thermodynamically driven process relying on molecular recognition. In this experiment, we deal with the spontaneous adsorption of molecules onto a surface from solution. In particular, there is an extensive knowledge base that has been developed on *n*-alkanethiols, which are known to spontaneously assemble to form densely packed oriented monolayer films on gold.⁴ The driving forces for the formation of a self assembled monolayer (SAM) of *n*-alkanethiols on gold are covalent and non-covalent: the S-Au bond (44 kcal/mol) and the van der Waals interactions between alkyl chains (1.5-2 kcal/mol/CH₂). As the alkane chain lengthens, the coverage and film order increase due to increased chain to chain interaction.⁵ Appending a functional group to the end of the alkane chain has been shown to affect chain packing through steric and electrostatic interactions.⁶ While the specific driving interaction of sulfur-gold bonding is preserved in our

experimental system (see §2.3), there are many differences between our long conjugated rigid rod molecules and the shorter, more labile alkanethiols that may lead to significant differences in their self assembly.

The assembly of long conjugated molecules has not been well characterized. We may expect the same factors to be relevant to their packing as to the alkanethiols: gold-endgroup bonding, and interchain interactions including bonding and steric hindrance. The van der Waals interaction between alkyl chains contributes to the driving force for the formation of the *n*-alkanethiol SAM; this interaction may be missing with the thiophene ethynylene (TE) oligomers. An additional concern with the TE system is the presence of sulfur in the backbone, which may provide a competing assembly mechanism to the sulfur in the endgroup. A family of TE oligomers has been synthesized with a variety of functional endgroups (as discussed in the previous chapter) and self assembled onto gold surfaces. Although the TE systems were not ideal for transport, they are reasonable to use for surface experiments. The rigid rod nature, length, and backbone are properties that are different from alkanethiols; we therefore must determine which, if any, of the characteristics of the well known *n*-alkanethiol system remain applicable and which must be determined anew for this conjugated system. Grazing angle infrared (GAIR) spectroscopy, ellipsometry, Auger electron spectroscopy (AES), and X-ray photoelectron spectroscopy (XPS) were used to study their assembly.

The gold substrates used in the following experiments were prepared as follows. Silicon substrates were sonicated in chloroform for 10 minutes, rinsed with ethanol (EtOH) and Millipore water. Substrates were then submerged in piranha etch (sulfuric acid and peroxide) at 90°C for 10 minutes and rinsed with Millipore water and EtOH. Wafers were loaded into a Varian thermal deposition chamber (base pressure 8×10^{-8} torr), and a 10 nm chromium adhesion layer was deposited, followed by 200 nm of gold. Film thicknesses were controlled using a calibrated quartz crystal oscillator monitor. Baseline ellipsometry

measurements were taken on the wafers promptly upon their removal from the deposition chamber. Monolayer thicknesses were later determined from the changes in ellipsometric angles measured before and after molecular depositions. After ellipsometry, the wafers were submerged into solutions of the TE molecules in freshly distilled tetrahydrofuran (THF). Solutions of approximate concentration 0.1mM were used whenever possible – due to shortages of molecules, some solutions were of lower concentration. After a few days, the wafers were removed from solution, rinsed with THF, acetone (ACE) and EtOH, and spun dry. Ellipsometry readings were taken at 4 points on the wafer, and GAIR spectra were obtained. All depositions discussed here were done in a nitrogen atmosphere, with the exception of the thioacetates and the unfunctionalized oligomers, some of which were deposited under ambient conditions.

Ellipsometry is a nonperturbative technique used to determine the thickness and refractive index of thin films. Linearly or circularly polarized light (with equal parts s and p polarization) is reflected at an oblique angle from the sample. The elliptically polarized reflected light is sent through a phase compensator and polarizer to determine the ellipsometric angles Δ and ψ . These values are determined by the relative complex reflection coefficients for the s- and p- polarized components of the outgoing light. They are related as follows:

$$r_p/r_s = e^{i\Delta} \tan \psi.^7$$

The index of refraction and film thickness are then determined from the Δ and ψ data. The following approximate refractive index values were used: 1.55 for aromatic compounds, and 1.50 for alkanethiols. The uncertainty in assigning the appropriate value of refractive index corresponds to an uncertainty of $\pm 2 \text{ \AA}$ in film thickness.

Infrared spectroscopy is a photons in - photons out detection technique. IR spectroscopy probes the molecular vibrational states. The sensitivity of the chemical bonds

to their local environment manifests itself in frequency shifts of the vibrational modes (in effect, a change in the spring constant of the bond). Thus, information may be gleaned regarding the bonding state of the vibration being probed, as well as the local intermolecular interactions. For instance, in a well-ordered $C_{17}H_{35}SH$ alkanethiol monolayer (ML) on gold, the methylenes (CH_2) in the backbone have a symmetric stretch at 2850 cm^{-1} and an asymmetric stretch at 2917 cm^{-1} . The methyl groups (CH_3) show up at 2878 and 2965 cm^{-1} . The $C_7H_{15}SH$ ML on gold does not attain the crystalline packing of the $C_{17}H_{35}SH$, and a commensurate shift in the energy and FWHM of these stretches is seen: the symmetric stretch shifts up 2 wavenumbers to 2852 cm^{-1} , and the asymmetric stretch shifts up 4 wavenumbers to 2921 cm^{-1} . A shift to higher wavenumber is indicative of increased disorder; it is generally accompanied by feature broadening. The methyl groups shift by only one wavenumber, to 2879 and 2966 cm^{-1} , as they are in basically the same environment.⁸

IR radiation is absorbed when the oscillating dipole moment of the molecular stretch interacts with the oscillating electric vector of the infrared beam. In a molecule with a center of symmetry, those vibrations symmetrical about the center of symmetry will be inactive in the IR.⁹ Most functional groups are not centrosymmetric. When IR spectroscopy is performed on a metal like gold, an additional selection rule becomes relevant. Gold is a strong absorber in the IR; the signal from any molecular stretches that are parallel to the Au surface is canceled by the response of the Au to the oscillating dipole. If the molecular dipole subtends an angle θ with the normal, the IR signal will be attenuated to $\cos^2\theta$ of its full intensity.¹⁰ These selection rules are valuable for deducing structural information regarding the orientation of the molecules on the surface. In order to determine which vibrations were influenced by the Au substrate, comparison is made to an isotropic solid state spectrum. The reference sample is obtained by dispersing a small amount of oligomer in potassium bromide (KBr) salt and forming the mixture into a pellet using a hydraulic press. Transmission IR spectra are taken on those pellets. The KBr spectra

provide an isotropic reference spectrum for comparison with the GAIR data. In addition, solution IR spectra were taken for each compound by D. Pearson, the student who synthesized the compounds. However, in solution, the molecules have rotational freedom that they do not have in the solid state, and may not have in a self assembled film. The result of this freedom is the averaging out of certain information in the spectra. Generally, more features are resolved in solid state spectra. Therefore, whenever sufficient oligomer was available, the additional KBr transmission measurement was done.

§ 3.1 Unfunctionalized TE_n Assembly

Given that the as-designed molecule specifically relies on the endgroup thiol self assembling to gold, why attempt to self assemble the unfunctionalized TE_n backbone? Alkanethiols self assemble via the sulfur to Au, Ag, Cu, Pt, Zn, and GaAs with varying degrees of efficiency.¹¹ While no discussion of the chemisorption of thiophenes to gold was found in the literature, thiophenes have been known to spontaneously assemble on Ag(111), Cu(111), Ni(111) and Pt(111).^{12,13} The mechanism by which thiophene adsorbs to the metal is not yet established. At low coverage, the thiophene molecule is thought to lie flat, interacting through its π -electron cloud and/or the sulfur lone pair of electrons. At higher coverages, the rings tilt away from the surface to interact with the surface via the sulfur lone pair electrons. For quaterthiophene on Ag, at higher coverages, the molecule adopts a twisted conformation, attributed to the competing forces of intermolecular interaction, p_z electron delocalization, and steric hindrance. It is logical to suspect that thiophene may also assemble on Au. There is substantial evidence that a backbone-substrate interaction may occur with a thiophene containing system, and may therefore provide a competing interaction to the desired endgroup thiol-Au assembly mechanism.

The unfunctionalized dimer, tetramer, octamer, and hexadecamer were self assembled onto clean gold surfaces for 1.5–6 days (see Table 3.1.1). After the molecular deposition, the substrates were rinsed in solvents, spun dry, and ellipsometric measurements were taken. In all cases, a molecular film was formed; the film was not removed upon repeated sonication in solvents. These compounds stick tenaciously to the gold surface, standing up to the normal cleaning procedure used for the thiol terminated oligomers including sonication. Ellipsometric thicknesses of the unfunctionalized molecules—TE₂, TE₄, TE₈, and TE₁₆—were 8.6, 8.4, 14.3, and 22.0 Å respectively (see Figure 3.1.1). If the rings in the TE_n backbones were lying flat on the gold substrate, and

if the solvent cleaning removed any oligomers physisorbed to the film surface, then one may expect the same film thickness regardless of the number of rings in the molecule. The experimental trend in thickness is consistent with the proposed mechanism of assembly for multi-ring molecules at high surface coverage previously discussed: the molecules interact with the gold surface through the sulfur lone pair of electrons; as the molecule gets longer with more thiophene rings, fewer consecutive sites will be available for the longer molecules to satisfy all of their binding sites simultaneously. The competing interactions will cause greater conformational changes to occur along the molecule's backbone, with more expansion into the third dimension, leading to thicker films.

	dep (hrs)	L (Å)	ellips (Å)	τ 1382 (min)	τ acet (min)	%C8	AES λ (Å)	n
TE ₂	144	13	8	97±26%	150±12%	67±1	10.0	9.3
TE ₄	36	25	8	290	270	44	10.4	4.3
TE ₈	36	50	14	330±37%	3300±99%	45±1	11.6	1.9
TE ₁₆	70	100	22	8400±37%	4300±88%	55±3	11.2	≅1.0

Table 3.1.1 Results for the unfunctionalized TE_n. Modeled molecular length (L), and experimental ellipsometric ML results are in Å. Time constants derived from C8 displacement experiments are also given: 1382 cm⁻¹ is characteristic of the C8 coming onto the surface, and the acetylene is associated with the TE_n oligomer of the original film. Attenuation length as determined from AES data is shown, with the effective density scaled to the largest oligomer. The % spreads are wafer to wafer differences.

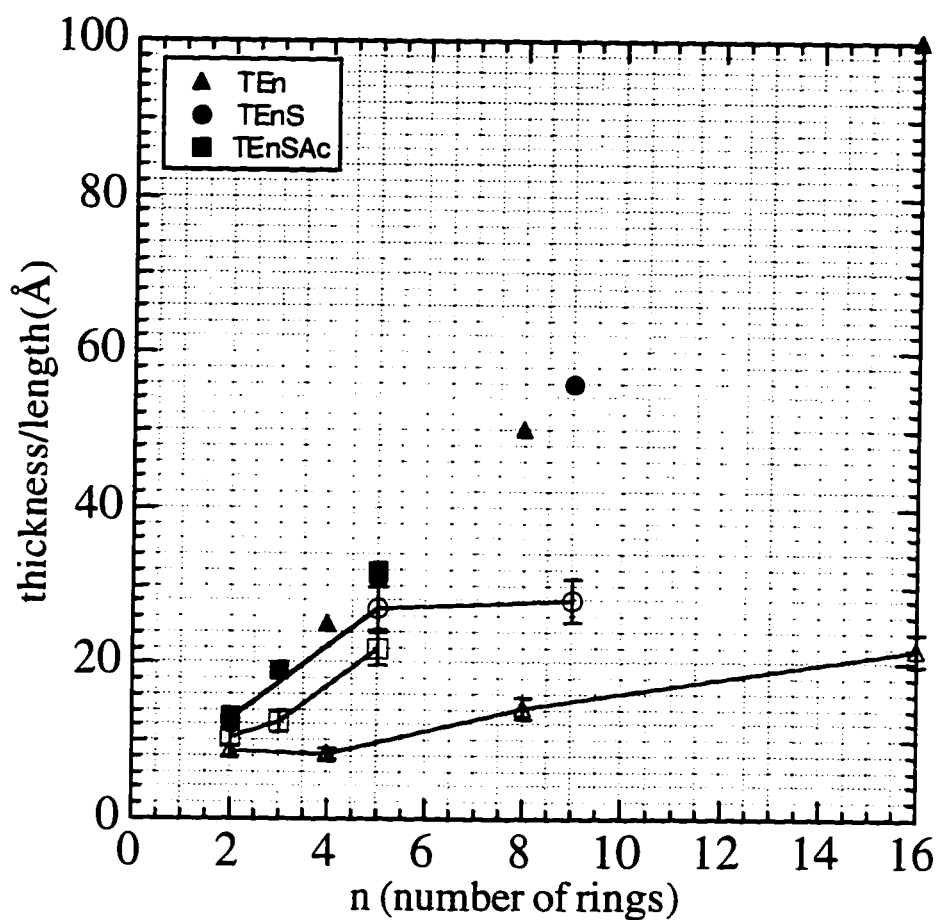


Figure 3.1.1 Modeled molecular length (solid markers, no lines) and experimental ellipsometric ML thickness (open markers with lines) are plotted versus the number of rings (thiophenes and phenyls) in the oligomer. Oligomers are distinguished by functionalization. The functionalized oligomers form films of a thickness close to the modeled length up to the tetramers, then saturate; the thioacetate terminated oligomers are consistently 2.5 - 5 Å thinner than the thiolates; the unfunctionalized oligomers' film thicknesses increase with n at a slower rate than the functionalized oligomers'.

Preliminary XPS data were taken on these ML. XPS is a photon in- electron out detection technique. It is particularly suited to elemental and chemical bonding identification. The data collected on the unfunctionalized TE_n show some indication of two distinct sulfur peaks separated by approximately 2 eV, corresponding to two distinct binding energies. There is only one kind of sulfur in the molecule, in the thiophene ring. The thiophene S 2p is expected at 164.2 eV.¹⁴ The measured shift is consistent in direction and approximate magnitude with the shift in binding energy seen by XPS for free thiols to gold-bound thiolate.¹⁵ A possible interpretation of this result is that the thiophene sulfur gains energy by chemisorbing to the gold substrate. However, due to steric hindrance, not all of the sulfurs can orient themselves to take advantage of this binding, hence the two separate states. Unfortunately, due to the low signal to noise ratio, it was not possible to clearly establish the peak positions and areas for the various compounds. If such data could be obtained, one might expect to see the ratio of high to low binding energy S change with chain length, as the number (fraction) of thiophene rings capable of chemisorbing saturates (decreases) due to the interactions described previously.

A full discussion of the analysis done on the AES results is presented in §3.4. In summary, a model is constructed to relate the intensity of the gold signal from the various films. An effective density is extracted from the attenuation of the gold signal generated by the gold substrate layer. These effective densities decrease with increasing chain length in proportion to the number of monomers in the molecule. In other words, the model says that there are 9.3 times more TE₂ molecules on the surface than there are TE₁₆ – roughly proportional to the difference in the number of binding sites required for each molecule. The general 1:2:4:8 trend is well reproduced for the unfunctionalized oligomer series, but the experimental numbers are consistently higher than the expected ratio. This result correlates well with the intuitive picture that as the oligomers get longer, there will be fewer sites available that allow the molecules to satisfy their binding sites while still packing

together densely. The resulting film will have fewer molecules with more unclaimed spaces as the oligomer gets longer.

IR spectra were taken on all films. Similar features were evident for all films, although a few sharp features stand out in the low frequency region. The high frequency region shows broad C-H stretches corresponding to methyl (2874 and 2965 cm^{-1}), methylene (2932 cm^{-1}), and sometimes the aromatic (around 3070 and 3100 cm^{-1}) C-H stretches. Figure 3.1.2 shows an isotropic spectrum derived from the transmission data taken on the KBr pellet, and the reflectance spectrum taken on the TE₄ film. There are two distinct acetylenes in TE₄: one between two thiophene rings, the other with a thiophene ring on one side and a trimethylsilane (TMS) on the other (see Figure 3.1.3a). The acetylene stretches show up at 2145 and 2190 cm^{-1} (see Figure 3.1.3b). The Si atom of the TMS adds mass to the TMS-acetylene spring relative to the thiophene-acetylene spring. The TMS group also adds electron density to the acetylene, as does the thiophene. Apparently, the charge transfer effect of the thiophene dominates, because the thiophene acetylene stretch is shifted to a higher frequency than the TMS-acetylene. Both stretches are evident in the isotropic spectrum; the presence of the higher energy peak in the GAIR is somewhat less obvious. Structural information is deduced from IR through comparisons of this type.

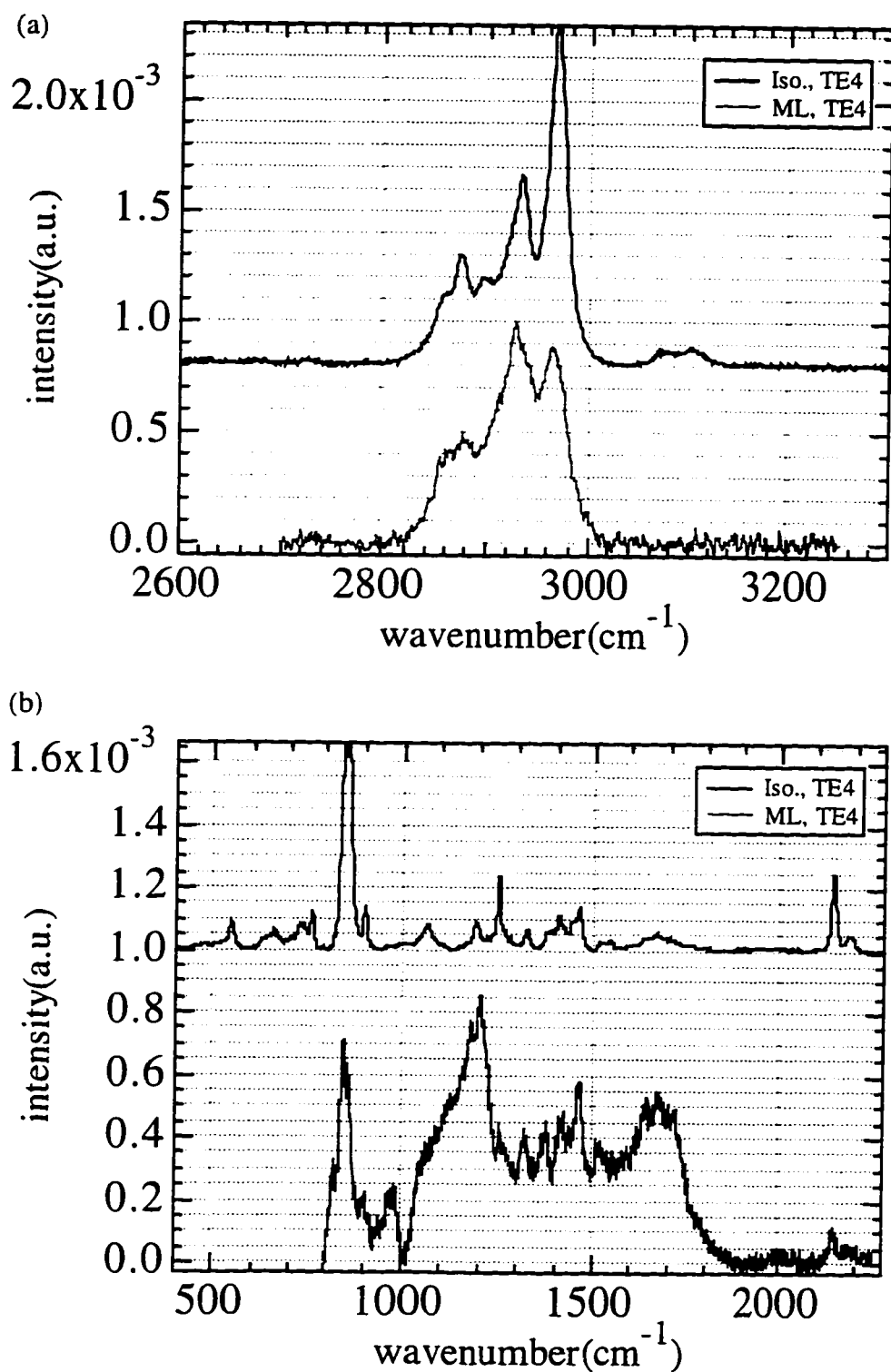


Figure 3.1.2 IR spectra from isotropic TE₄ and TE₄ ML. (a) High frequency region showing C-H stretches. (b) Low frequency "fingerprint" region. Scaling and offset of isotropic data are arbitrary.

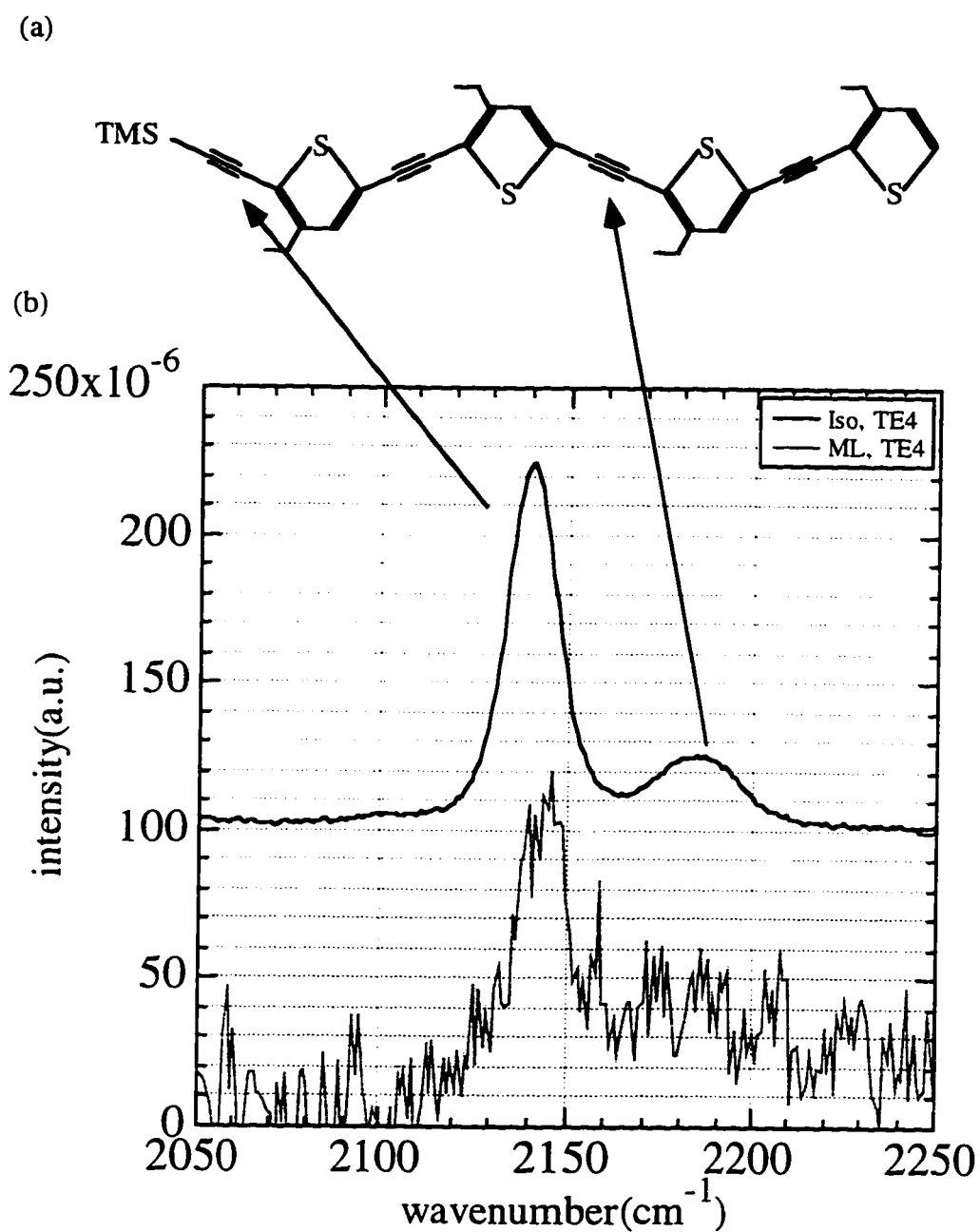


Figure 3.1.3 (a) Schematic of TE₄ showing the two different acetylene environments.

(b) Isotropic and ML spectra of acetylene stretches from TE₄ at 2145 and 2190 cm⁻¹.

It is not clear why the relative intensities do not scale with the number of oscillators.

The absolute scaling of the isotropic spectrum is arbitrary.

The evidence so far suggests that the unfunctionalized molecules form a strongly adsorbed ML, presumably via discrete S-Au interactions. The XPS results were inconclusive regarding the chemisorption of the thiophene. One way to check the strength of the TE_n-Au bonding is by replacing the molecules on the surface with an alkanethiol. A kinetics study was done on these ML to get a relative measure of the ease of displacement of the TE_n molecule by C₈H₁₇SH (*n*-octanethiol, herein C8). The analysis consists of tracking the peak area from the IR spectra of a stretch specific to each of the molecules: the 1381-2 cm⁻¹ for the C8 and the acetylenes for the TE_n. For such an analysis to be rigorously correct, the orientation of the oscillators must not change. It is not known if the oscillators reorient; the TE_n oligomers may adjust their angle with respect to the surface upon C8 insertion. We do not presume to extract such precise rates from this study; the results presented are strictly a relative measure amongst oligomers. The peak area is plotted versus time in solution, and the curve is fit with an exponential. A summary of the time constants associated with the displacements is given in Table 3.1.1.

Amongst the unfunctionalized molecules, the surface with the shortest molecule (TE₂) showed the fastest uptake of C8, and the highest level of C8 incorporation as $t \rightarrow \infty$, approximately 67%, based on the relative peak heights of the mixed ML to the average of ten pure C8 ML. It also showed the most rapid loss of acetylene stretch. The TE₁₆ followed with an intermediate value of C8 incorporation, 55%, but the slowest rate of loss of acetylene and rate of C8 incorporation. The TE₁₆ may be an inefficient packer, leaving many empty spots accessible to the small C8, but not leaving the surface itself. The TE₄ and TE₈ ML surfaces showed comparable values for C8 uptake time and incorporation plateau of approximately 45%. The similarity in C8 uptake rate and percent incorporation for TE₄ and TE₈, together with the increase in ellipsometric thickness from TE₄ to TE₈, may be interpreted in the following manner. If the same number of binding sites are active (possibly due to steric hindrance preventing the remaining sites for the TE₈ from binding to the surface), then the C8 would face in effect the same barrier to incorporation, n sites at x

eV per site. This would lead to the similar values for C8 time constant and plateau value. The fact that TE₄ and TE₈ are smaller than TE₁₆ may permit them to pack together more efficiently on the surface, allowing less C8 into the film than does TE₁₆. The acetylene rate of loss increases with increasing oligomer length (within experimental error, TE₂≈TE₄ < TE₈≈TE₁₆), consistent with molecule binding energy proportional to the number of thiophene rings in the backbone.

In summary, there is evidence for the strong assembly of the unfunctionalized TE_n oligomers to Au, indicative of a competing assembly mechanism to the endgroup thiol-Au interaction. Comparison of the isotropic spectrum and the GAIR results leads to an approximate tilt of 80-90° between the molecular axis and surface normal; i.e., the molecules are basically lying down on the surface, although not necessarily flat. The apparent behavior of the TE_n is consistent with the mechanism proposed for assembly of quaterthiophene at high coverage: the molecules interact with the surface through the sulfur lone pair of electrons and the rings are tilted away from the surface. The molecules adopt a twisted conformation leading to a thicker film for longer molecules. As the molecular length increases, the efficiency of the packing first increases and then decreases, as evidenced by C8 insertion rates and equilibrium incorporation, and effective density deduced from AES data. Increased steric hindrance and energy cost of conformational changes for the longer oligomers would lead to this result.

§ 3.2 Monofunctionalized TE_nS Assembly

For the monofunctionalized oligomers, the desired assembly mechanism is the same as the well-characterized alkanethiol system: S-Au. Yet the systems were not fabricated with the SH endgroup of the alkanethiol, because thiols oxidize in air to form disulfides. Disulfides will still form a well ordered ML on Au, at a rate somewhat slower than thiols;¹⁶ the steric hindrance of the larger molecule may account for the difference in rate.¹⁷ For our system, difunctionalization is necessary to adhere both ends of the molecules to the electrodes. If such large molecules were to be difunctionalized with thiols and exposed to air, they would polymerize, forming aggregates too large to find their way to the substrate in an ordered fashion, assuming they could stay in solution at all. To address this concern, the molecules were fabricated with protected thiols in the form of thioacetates. The thioacetates are much more stable than the thiols in air; they may be cleaved to form thiolates by exposure to a base. NH₄OH was selected for its compatibility with microfabrication process constraints on heavy metal contamination. For monofunctionalized TE_nS MLs, ~6 µl of NH₄OH per mg of oligomer was added to the THF to cleave the thioacetate in situ and allow the formation of a free thiol in solution.

The endgroup of the TE_nS-deprotected oligomer is a phenyl ring with a thiol. The self assembly of phenylthiols on Au has been studied.¹⁸ Experimental and theoretical evidence indicate the phenylthiol assembles via the thiol with the phenyl ring normal to the Au surface. The hybridization of the S is expected to be sp, leading to the Au-S-C axis being straight. This configuration is predicted to occur at an energy only slightly lower than the sp³ hybridization, which would lead to the S-C bond being nearly parallel to the Au surface. GAIR analysis of a phenylthiol in this configuration would indicate suppression of a phenyl ring stretch with a dipole moment in the plane of the ring; the

stretch at 1012 cm^{-1} is such a mode. The sp configuration would be conducive to the desired geometry for electrode assembly, while the sp^3 configuration would not.

Monolayers were formed from the monofunctionalized monomer, dimer, tetramer and octamer. All appear to have formed strongly adsorbed MLs; the IR features and the ellipsometric thicknesses remain essentially unchanged on repeated sonication in THF. Ellipsometric results show distinct differences between the TE_n and TE_nS films; the endgroup apparently has some effect on the assembly. Ellipsometric thicknesses of the monofunctionalized TE_nS MLs are plotted versus their monomer content in Figure 3.1.1. The thickness initially increases with molecule length, then saturates. Experimentally determined thicknesses of TE_1S and TE_2S are approximately equal to their modeled length, L ; TE_4S film thickness is $0.87\ L$; TE_8S film thickness is $0.5\ L$. A simple picture of the assembly may be that the endgroup-Au interaction energy is indeed higher than the thiophene-Au interaction energy; as long as the endgroup can find the surface, the endgroup interaction dominates, and the molecule essentially stands up (at some tilt angle from the normal). As the molecule gets longer, the interaction energies summed from the various thiophene-Au interactions may approach the energy of interaction of the thiol. In addition, it becomes less statistically likely that the molecule-Au interaction will be via the endgroup as the molecule first comes into contact with the surface. If the backbone interacts first, the molecule may or may not come off the surface again to readjust its position to interact via the endgroup, as alkanethiols do.¹⁹ Even if the same number of oligomers were lying down for the TE_1S as for the TE_8S , those TE_1S lying down would occupy substantially less surface area, leaving a larger fraction of the molecules on the surface standing up. The trend in the ellipsometric data is consistent with this hypothesis.

	dep (hrs)	L (Å)	ellips (Å)	τ 1382 (min)	τ acet (min)	τ 1012 (min)	%C8	AES λ (Å)	n
TE ₁ S	36	12	13	270±1%	57±25%	430±12%	75±1	9.1	9.2
TE ₂ S	70	18	17	1080±11%	820±28%	800±22%	47±1	9.9	6.2
TE ₄ S	112	31	27	730±11%	170±4%	430±8%	37	10.7	3.3
TE ₈ S	111	56	28	–	–	–	–	19.6	≅1.0

Table 3.2.1 Results for the monofunctionalized TE_nS ML. Modeled molecular length (L), and experimental ellipsometric ML results are in Å. Time constants derived from C8 displacement experiments are also given: 1382 cm⁻¹ is characteristic of the C8 coming into the film and the acetylene and 1012 cm⁻¹ are associated with the TE_nS oligomer of the original film. Attenuation length as determined from AES data is shown, with the effective density scaled to the largest oligomer. The % spreads are wafer to wafer differences.

The effective densities extracted from the AES data show a similar trend with oligomer length as for the unfunctionalized oligomers. There, the trend was easily interpreted as reflecting the relative surface areas covered by the oligomers. If a simplistic view of the assembly were taken, endgroup down, chain standing up at some angle to normal, then attenuation would be expected to increase with increased film thickness. The opposite attenuation trend is seen in the AES data for TE_nS . As with the unfunctionalized ML, the shorter oligomer still stops more electrons than the longer one. We may conclude that there are fewer long TE_nS per unit area than there are short ones. Otherwise, from a simple mass density argument, the longer TE_nS would stop more, or at least the same number of, Auger electrons. The behavior is consistent with the assembly mechanism proposed above: as the TE_nS gets longer, the occurrence of thiol-Au interaction decreases and more molecules are lying down on the surface (though not necessarily flat), leading to a less dense film with increasing oligomer length.

GAIR spectra were taken on all TE_nS MLs. Similar features were evident in all spectra (see Figure 3.2.1 for a representative spectrum). The acetylene peak at 2190 cm^{-1} is much more intense than for TE_n , consistent with (some of) the molecules standing closer to normal (the dipole of the $\text{C}\equiv\text{C}$ stretch is basically in line with the long axis of the molecule). Ring C-H modes near $1450\text{-}1500\text{ cm}^{-1}$ also sharpen up in the TE_nS film spectra, indicating somewhat less disorder in the TE_nS films than in the TE_n films. A phenyl mode shows up clearly at 1012 cm^{-1} . This mode arises from the phenyl C-H bending, giving rise to a dipole parallel to the molecule's axis.²⁰ Transmission IR measurements were done on an isotropic distribution of the TE_4SAC molecule dispersed in KBr. Comparison of experimental (GAIR) to modeled intensity deduced from the transmission spectrum predicts the average molecular axis tilt to be $20\text{-}30^\circ$ for TE_1S , $\sim 40^\circ$ for TE_4S , and $\sim 60^\circ$ for TE_8S .

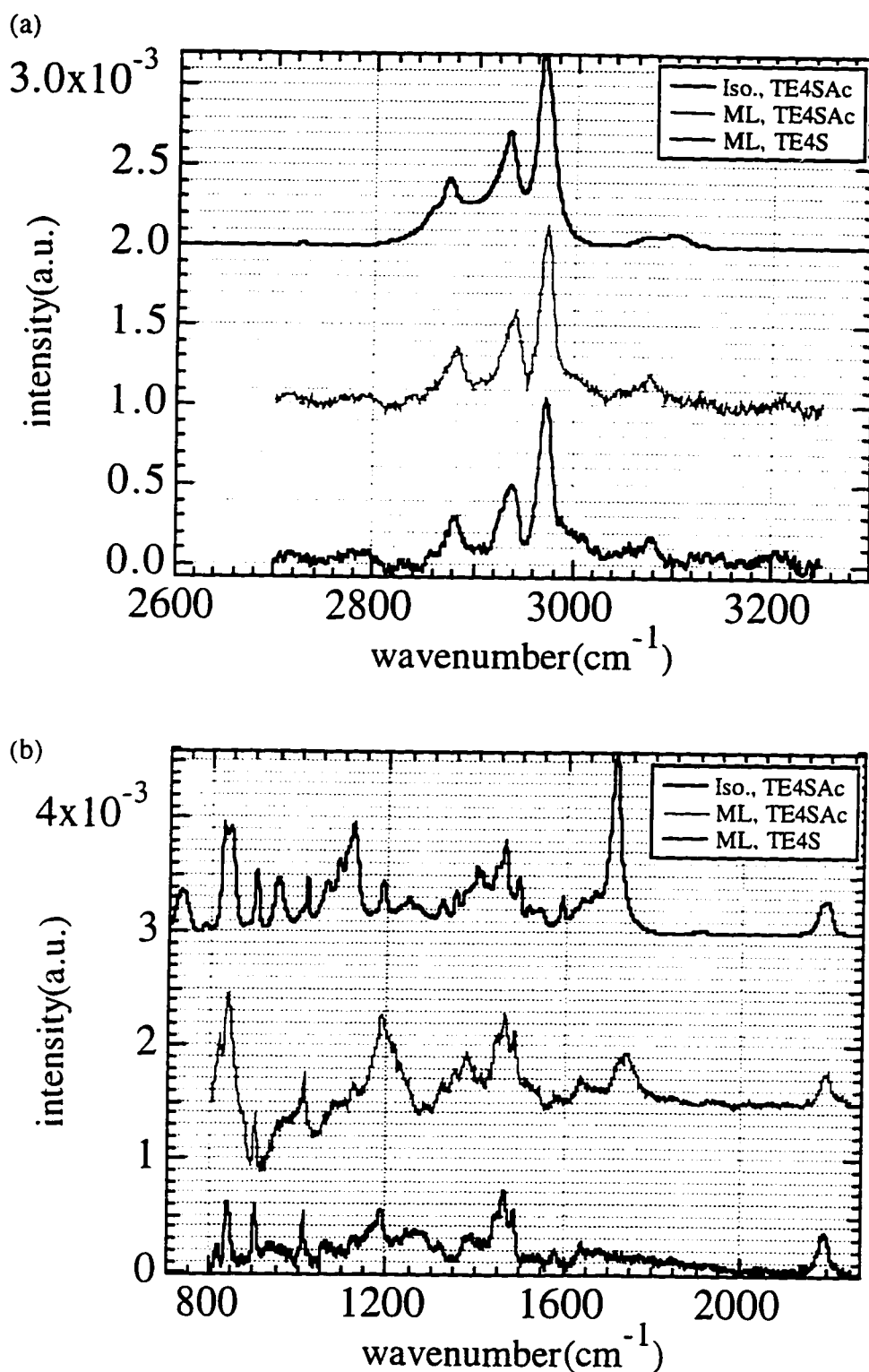


Figure 3.2.1 IR spectra from isotropic TE₄SAc (KBr) and ML of TE₄SAc, TE₄S.

(a) High frequency region showing C-H stretching. (b) Low frequency "finger-print" region. Scaling of isotropic data is arbitrary. Spectra are offset for clarity.

The evidence so far suggests that the monofunctionalized molecules form a disordered, but strongly adsorbed, ML. It is likely that the thiol endgroup is favored for attachment to Au, at least for the shorter molecules, as evidenced by the difference in ellipsometric thickness for TE_n versus TE_nS ML. A kinetics study was done on these ML to get a relative measure of the ease of displacement of the TE_nS molecule by C8. The analysis here includes tracking the peak area of the IR mode at 1012 cm^{-1} . A summary of the time constants associated with the displacements is given in Table 3.2.1. TE_1S shows the highest incorporation of C8, followed by TE_2S then TE_4S . The displacement rates do not track the % incorporation as they did with the TE_n . The loss of phenyl stretch is essentially the same for all compounds tested. TE_2S is the slowest to take up C8, and the slowest to lose acetylene. We do not have a model for this behavior at this time. Comparing the unfunctionalized oligomers with their functionalized counterparts, the C8 rate and % incorporation are higher for the TE_n than for the TE_nS , $n=2, 4$. The maximum number of thiophene rings that could be adsorbed to the Au surface in these cases is 4; a limit to the relative measure of the strength of thiophene-Au versus thiol-Au may be estimated *assuming no chain-to-chain interaction for the TE_nS* . If all 4 thiophenes are interacting with the Au surface, then their total energetic contribution is less than a single thiol-Au bond.

The monofunctionalized TE_nS oligomers form strongly adsorbed, possibly disordered, anisotropic ML. The presence of a single functional endgroup has a distinct effect on the IR spectra and the ellipsometry, leading to the conclusion that the assembly of at least some of the molecules is dominated by the endgroup-gold interaction. The phenylthiols-Au may not be a dominant effect for the longer molecules that are relevant to the ultimate experiment of self assembling a long difunctionalized oligomer across electrodes. Depositions of three difunctionalized oligomers (STE_1S , STE_2S and STE_8S) were attempted, but failed due to equipment and operator errors. A critical question remains to be answered regarding the assembly of such a molecule. Theoretical treatments

have predicted a low energy barrier between the S sp^3 and sp hybridizations. If a difunctionalized oligomer were to assemble from a dilute solution onto a Au surface, it might interact first with the endgroup thiol, but if the energy difference to the sp^3 hybridization is less than the energetic contribution from the thiophene-Au interactions, and there is enough energy to surmount the barrier between the conformations, the thiol-Au bond may assume the sp^3 hybridization such that both thiols and some thiophenes could assemble to the Au. The resulting configuration would not allow for the oligomer to bridge two electrodes.

§ 3.3 Monofunctionalized TE_nSAc Assembly

Evidence for the persistent presence of thioacetate was provided by nuclear magnetic resonance analysis of a deposition solution of THF + NH₄OH + functionalized TE_nS(Ac) after 4 and 7 days. Since the thioacetates apparently did not all cleave to the thiol, the possibility of an additional competitive assembly mechanism exists. It has been suggested that the thioacetate-terminated molecules would form surface bound thiolates similar to the cleaved species.²¹ For the monofunctionalized monomer, dimer and tetramer, depositions were done without deprotection to study the assembly of the thioacetates.

Self assembled monolayers were formed without base promoted cleaving of the thioacetate for the thioacetate terminated oligomers: monomer, dimer, and tetramer. Ellipsometry and IR spectroscopy results indicate that the final product is very similar with and without base promoted cleaving. The thioacetate MLs are consistently 2.5-5Å thinner than the thiol MLs. The molecule itself is a few angstroms longer; if the thioacetate had cleaved, one would expect the same film thickness if the packing were the same. Ellipsometry is a bulk measurement; we cannot distinguish the same density packing of the same length molecules from lower density packing of longer molecules. The spectra from the thioacetate MLs show the presence of acetate in the 1675-1715 cm⁻¹ region, dominant in the TE₄SAc (see Figure 3.2.1). The high frequency regions of methyl and methylene stretches are very similar.

The effective densities derived from AES data of thiol and thioacetate MLs are compared in Table 3.3.1. For the monomers, the results are similar, but as *n* increases, the TE_nSAc films become less effective attenuators. This may be consistent with fewer molecules on the surface for the thioacetates. Lower packing density could be due to kinetics – the larger headgroup may take longer to find its way, so to speak. However, the tetramer depositions were continued for 4.5 days for TE₄S and 11.5 days for TE₄SAc.

Slower kinetics does not seem to be a reasonable explanation. An interpretation of this result is that the acetate does not cleave as expected, but bends out of the way, allowing the S to interact directly with the gold surface. The acetate would effectively occupy one binding site for every one occupied by a S, leading to half as many thioacetate-terminated molecules on the surface per unit area as for the base-promoted cleaved thiol-terminated oligomers.

A C8 displacement comparison was done between the thiol (TE_nS) and the thioacetate (TE_nSAc) of the monomer, dimer and tetramer. The dilute packing of the thioacetate predicted by the AES model is consistent with the faster uptake of C8 seen for the thioacetate terminated oligomer films. The surfaces with thioacetate terminated tetramer (TE_4SAc) MLs show a factor of 5 faster uptake of C8 than those with thiol terminated tetramers (TE_4S), as determined from the rate of increase of the 1382 cm^{-1} stretch in the IR spectra. The level of C8 incorporation into the ML of TE_4SAc as $t \rightarrow \infty$ is approximately 46%, based on the relative peak heights of the mixed ML to the average of ten pure C8 ML. The limiting values of % C8 incorporation do not show the same length dependence as the AES attenuation data: the values are the same for $n=1$, and differ by 80% for $n=2$ and 4. However for $n=2$, the TE_2S incorporated more C8 than the acetate, while for $n=4$, the acetate incorporated more. The variations in rate of uptake and total incorporation are inconsistent with the hypothesis that the thioacetates end up as thiolates. If the thioacetates formed a less dense film with the same binding mechanism, one might expect a much greater initial uptake of C8, but the same limit at infinity. If the kinetics of getting to the surface and cleaving were slower for the thioacetates, but the final chemistry were the same, then the bound oligomers should exhibit the same rate of displacement as the thiols.

	dep (hrs)	L (Å)	ellips (Å)	τ 1382 (min)	τ acet (min)	τ 1012 (min)	%C8	AES λ (Å)	n	SAc/ S
TE ₁ SAc	91	13	10.5	57 \pm 16%	13 \pm 31%	128 \pm 13%	76 \pm 3	9.5	.0583	97%
TE ₁ S	36	12	13	270 \pm 1%	57 \pm 25%	430 \pm 12%	75	9.1	.0601	
TE ₂ SAc	70	19	12.5	268	370 \pm 11%	330 \pm 89%	53	10.7	.0354	88%
TE ₂ S	70	18	17	2000 \pm 11%	930 \pm 20%	580 \pm 20%	66	9.9	.0404	
TE ₄ SAc	278	32	22	510 \pm 29%	2900 \pm 74%	1200 \pm 53%	46 \pm 3	18.9	.0119	55%
TE ₄ S	112	31	27	730 \pm 11%	170 \pm 4%	430 \pm 8%	37	10.7	.0216	

Table 3.3.1 Results for the monofunctionalized TE_nSAc. The data for the TE_nS films are included for easy reference. Modeled molecular length (L), and experimental ellipsometric ML results are in Å. Time constants derived from C8 displacement experiments are also given: 1382 cm⁻¹ is characteristic of the C8 coming into the film and the acetylene and 1012 cm⁻¹ are associated with the TE_nSAc oligomer of the original film. Attenuation length as determined from AES data is shown, with the unscaled effective density. The ratio of effective densities for the TE_nSAc and analogous TE_nS oligomer are given in the last column (SAc/S). The $\pm\%$ correspond to wafer-to-wafer spreads.

The assembly mechanism for the thioacetate is not clear at this point, but the ellipsometry on the ML showed a similar value for the thiol and thioacetate. AES data indicate a difference in effective attenuation length; the difference increases as the length of the oligomer increases. There is also a significant difference in the displacement time constant measured. These variations are inconsistent with the hypothesis that the thioacetates end up as thiolates. It is not clear what effect the thioacetates remaining in the base-treated deposition solutions of TE_nS oligomers will have on the eventual electrical characterization of an oligomer across electrodes.

§ 3.4 Auger Electron Spectroscopy Data Analysis

Our TE films on Au may be modeled as a two layer system. The top layer, the oligomer, is approximated as a uniform mix of C, S and H, with a thickness corresponding to the depth measured by ellipsometry. The bottom layer is the gold, which for these purposes may be considered to be semi-infinite. All of the C and S signals are generated in the top layer, while the Au signal is generated in the bottom. Figure 3.4.1 shows the experimental values of atomic percent S, C and Au, and the atomic percent S and C obtained by counting atoms for the various TE oligomers (the element H does not have enough electrons to participate in the Auger process, so it is not counted). The At % are plotted against ellipsometrically determined film thicknesses. The data are in good agreement for S and C. The Au signal may be expected to decay exponentially with film thickness; it does not. In this section, a construct is presented that explores the observed trend in At % Au with thickness.

For an Auger electron signal to be detected, the incoming electron must interact with the species of interest and generate an Auger electron, and that electron must escape from the sample and be detected. The incoming beam flux is exponentially attenuated with a characteristic depth corresponding to 3 keV electrons. The proportion of the incoming electrons that generate Auger electrons from a given species is related to the number of interaction sites and the cross section of interaction (or sensitivity factor). Once the Auger electrons are generated, they will be exponentially attenuated as they travel through the sample. The amount of signal escaping will be exponential in the thickness of the film d , and the effective attenuation length, λ :

$$I = I_0 \exp (d / \lambda).$$

To be rigorously correct, I_0 is the value of the signal that would be measured off a clean gold film; it should be a constant for all samples. Since this analysis is strictly comparative, the actual value of I_0 is not relevant. I/I_0 gives the proportion of the beam that interacts with a given element, and creates an Auger electron which escapes the sample to be detected. We set I/I_0 equal to the atomic percent Au, and d to the ellipsometric thickness of the film. Solving for λ for each compound, we find results varying from 9.1 to 19.6 Å. To first approximation, the attenuation length should depend on the energy of the incoming excitation electron as:²²

$$\lambda_0 \text{ (nm)} = 0.087 \sqrt{E_0 \text{ (eV)}}.$$

in which case, $\lambda_0=7.2$ Å for all 68 eV electrons in organic compounds, distinctly shorter than all of our experimental results. More importantly, it does not account for our range of experimental values. Hidden in this relation is the assumption of a uniform density for the oligomer films. We expect a range of densities for our samples due to the varying assembly mechanisms at work: thiol-Au, thioacetate-Au, thiophene-Au, interchain interactions. The relationship of experimental λ amongst the oligomers should be indicative of these interactions.

There are three properties of the molecules in our films that are relevant to the film's effective stopping power: the number of molecules in the film per unit area; the length of each molecule, L (related to its mass); and the manner in which the molecules pack – do they form a crystalline lattice like alkanethiols, or leave many open spaces in the films, as TE₁₆ seems to do?²³ We assume these properties to be independent of energy. Together, they describe the mass per unit volume as well as the uniformity of coverage. The following relation is proposed for an effective density:

$$n = \lambda_0 / \lambda L.$$

The effect of the mass of the oligomer is factored out through L ; the remaining information describes the number of molecules per unit area and their packing. An independent measurement is required to separate this information.

	$\lambda(\text{\AA})$	$(\lambda/\lambda_0)^{-1}/L$	rel. n
TE ₁ S	9.1	.0651	9.2
TE ₂ S	9.9	.0374	6.2
TE ₄ S	10.7	.0216	3.3
TE ₈ S	19.6	.00654	$\equiv 1$
TE ₂	10.0	.00643	9.3
TE ₄	10.4	.0123	4.3
TE ₈	11.6	.0276	1.9
TE ₁₆	11.2	.0599	$\equiv 1$
TE ₁ SAc	9.5	.0583	4.9
TE ₂ SAc	10.7	.0354	3.0
TE ₄ SAc	18.9	.0119	$\equiv 1$

Table 3.4.1 Experimentally determined attenuation length λ for Auger Au electrons (68 eV) are listed for all compounds tested. The attenuation length is normalized to $\lambda_0=7.2 \text{ \AA}$, then length is factored out. The final column relates the normalized attenuation length among the families by functional group.

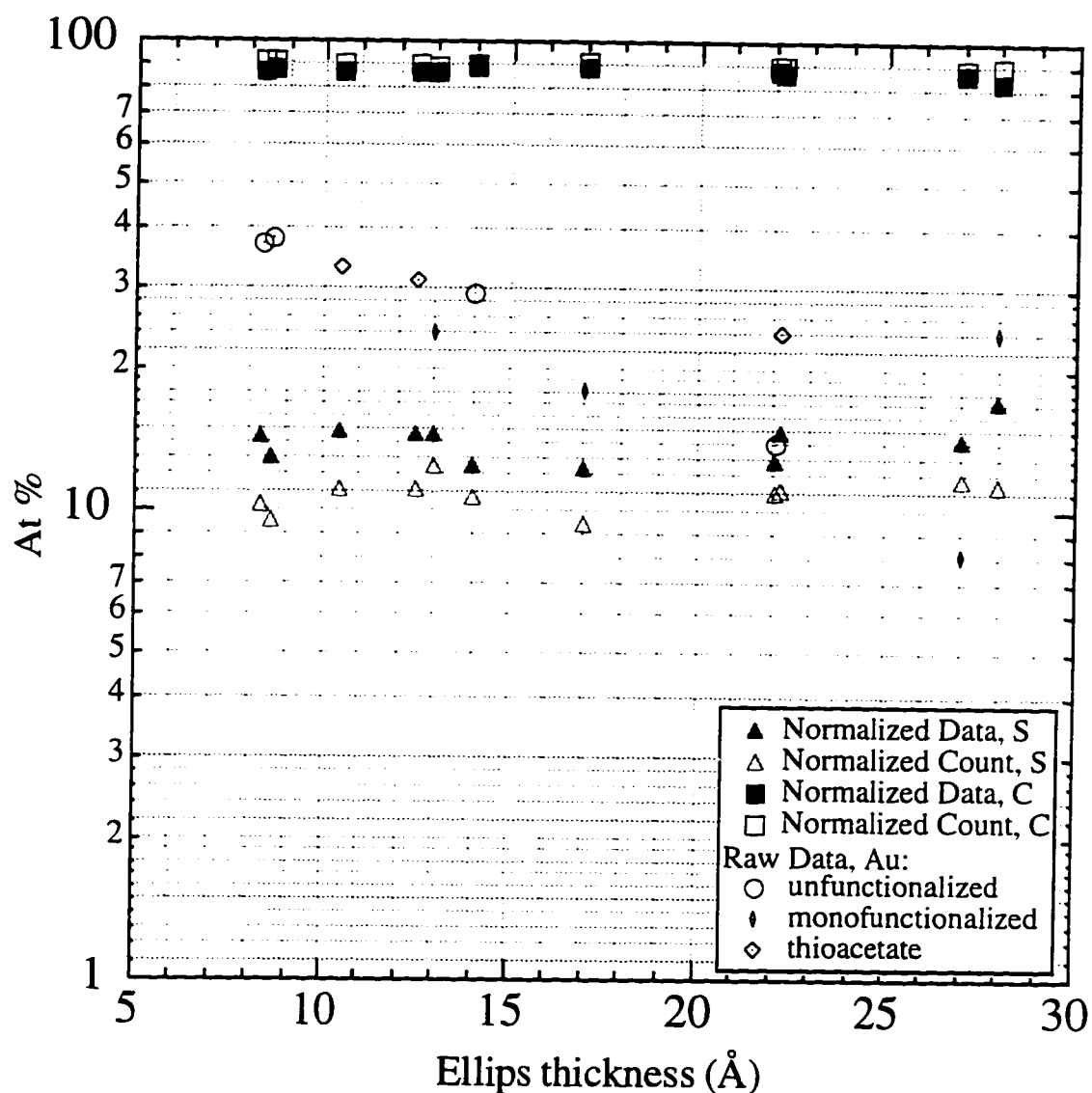


Figure 3.4.1 Experimental AES data (solid markers) and actual (open markers) atomic percent of S and C in TE films versus film ellipsometric thickness. Normalized count for atomic percents are determined by counting atoms in the molecule, excluding H, and normalizing S and C contributions to 100%. Experimental results for Au are also plotted, normalized to 100% for S and C. Data for S and C agree within a few percent. The raw data for Au is also plotted; the various functionalizations are distinguished by marker (see legend). The Au signal does not decay uniformly with thickness due to the variations in film density.

§ 3.5 TE insertion into C8

A concern with the gaps experiment for measuring the conduction through a single molecule is the availability of many (of order 10^4) sites for parallel adsorption. By filling the majority of these sites with a different (inert) molecule, it may be possible to limit the number of conjugated oligomers actually crossing the gap to of order 1-10 oligomers. The inert molecule must be electrically inactive, and short enough not to hinder the assembly of the long conjugated oligomers. If the inert molecule were assembled first, this process would have the added advantage of inhibiting any backbone-substrate interactions (as is suspected for the longer TE oligomers) by blocking the additional binding sites. If the neighboring sites were already occupied, the TE_nS oligomers may be forced to assemble via the endgroup.

Full MLs of C8 were formed, and put into solutions of TE_2S , TE_4S , TE_8S and TE_8 . Again, the behavior of the 1382 cm^{-1} peak specific to C8 was monitored as a function of time in solution. The 1012 cm^{-1} and acetylene peaks were not large enough for analysis. Peak area was plotted as a function of time and fit with an exponential function; time constants were extracted. In essence, the reverse of the C8 displacement experiment was performed. The TE molecules selected for this experiment were the three longest monofunctionalized (being the closest to relevant to the gaps experiment) and one unfunctionalized as a control. Two additional control wafers were "displaced" in pure THF. The C8 molecules in the film will try to maintain an equilibrium with the C8 in solution; they will be constantly coming off of and going back onto the surface. There are no C8 molecules in the TE solutions to start, so the net result of this flux is a decrease of the C8 on the surface. The THF control wafer data quantified this trend.

The time constant for the 1382 cm^{-1} mode of the THF control wafers was very rapid: 6.6 minutes. The ellipsometric thickness of the THF controls equilibrated at 50%

their original value. The TE₈ samples equilibrated at 107% of their initial values. This may be attributed to the TE₈ coating the ML and inhibiting diffusion of the C8 from the surface. If the TE₈ had found its way to the gold surface and assembled lying down as in the pure ML, the net effect on the ellipsometric thickness should have been a decrease. It is possible that the TE₈ also inserted itself into the film end-first, but there is no obvious driving force for this configuration. The films exposed to the TE_nS solutions continued increasing in thickness for the 16 hours analyzed. The monofunctionalized molecules apparently incorporated into the monolayers.

More characterization is needed to apply the insertion technique to self assembling oligomers across electrodes: the spatial distribution of substitutions; the orientation of the guest oligomers in the alkane matrix. STM experiments are being done to address these issues.²⁴

	τ 1382 (min)	%C8 $t \rightarrow \infty$	% Δ ellips
TE ₂ S	28 \pm 7%	30 \pm 2	+60
TE ₄ S	53 \pm 32%	50 \pm 1	+21
TE ₈ S	134 \pm 67%	49 \pm 10	+129
TE ₈	99 \pm 1%	41 \pm 4	+7
control	3.7 \pm 38%	40 \pm 3	-49

Table 3.5.1 Results for the TE_n(S) insertion into C8 ML. τ 1382 is the time constant derived from the 1382 cm⁻¹ IR mode characteristic of the original C8 film. %C8 incorporation corresponds to the $t \rightarrow \infty$ limit of the fit to the 1382 data. % Δ is the change in ellipsometric thickness as a percent of the film's original thickness. The \pm spreads are wafer to wafer differences.

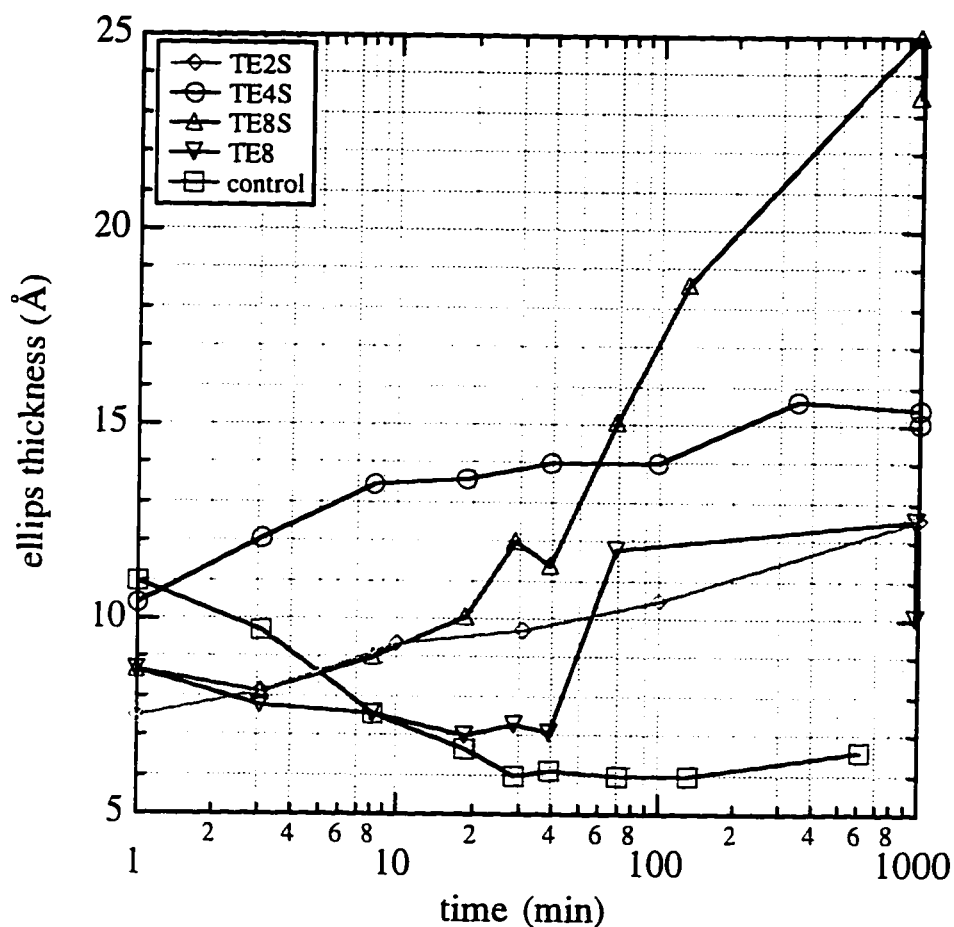


Figure 3.5.1 Ellipsometric thickness of C8 ML as a function of time in $TE_n(S)$ solution. The longest inserted molecules resulted in the largest change in ellipsometric thickness. A representative C8 control wafer is also shown.

§ 3.6 Summary and Conclusions

The surface assembly properties of ethyl β -substituted thiophene ethynylene oligomers to a gold surface were studied by ellipsometry, GAIR, AES, and XPS. The unfunctionalized oligomers strongly adsorb to gold. The thiophene rings may be responsible for this interaction. If a phenylthiol endgroup is attached to the molecule, the endgroup-surface interaction dominates for shorter oligomer lengths. IR results indicate that the films of TE_nS are anisotropic but disordered. As the monofunctionalized molecule length exceeds 30Å, the film thickness saturates; the average angle subtended by the monofunctionalized molecule increases with length. AES and ellipsometric results are consistent with the hypothesis that some oligomers are self assembling via the backbone despite the presence of the endgroup. The phenylthioacetate terminated molecules seem to self assemble via a different mechanism than the phenylthiols, as indicated by AES and displacement experiments. The persistent presence of thioacetate in deposition solutions indicates caution is necessary in interpreting results of TE_nS MLs. The TE_nS Ac systems studied are susceptible to a variety of competing assembly mechanisms: thiol-Au, thioacetate-Au, thiophene-gold.

Is it possible to induce the molecules to do the engineer's work? The error checking and materials selectivity of self assembly are powerful tools, attractive for building nanostructures. It is not clear what role the long rigid rod nature of the backbone plays independent of the thiophene interaction. The monofunctionalized tetramer of a related system – base-cleaved phenylthiolate terminated, dodecane β -substituted phenylene ethynylene (PE) – was self assembled in a deposition procedure similar to TE_4S . IR results indicate a comparable average tilt angle and disorder; the larger sidechain of the PE oligomer may be partly responsible for the disorder. The preliminary experiments on TE_nS

insertion into C8 MLs indicate that this technique may address the backbone assembly competition with the added advantage of allowing control of the density of oligomers.

References

- ¹ The design and synthesis of molecules for electronic properties are discussed in Chapter Two.
- ² The design and fabrication of electrodes are discussed in Chapter Four.
- ³ G.M. Whitesides, J.P. Mathias, C.T. Seto, *Science* **254**, 1312 (1991).
- ⁴ R.G. Nuzzo, D.L. Allara, *J. Amer. Chem. Soc.* **105**, 4481-83 (1983); R.G. Nuzzo, F.A. Fusco, D.L. Allara, *J. Amer. Chem. Soc.* **109**, 2358-68 (1987). For a comprehensive overview of SAMs, see: G.M. Whitesides, C. Gorman, "Self-Assembled Monolayers: Models for Organic Surface Chemistry" submitted to Handbook of Surface Imaging and Visualization, A.T. Hubbard, Ed. (CRC Press, Boca Raton Fla.).
- ⁵ M.D. Porter, T.B. Bright, D.L. Allara, C.E.D. Chidsey, *J. Amer. Chem. Soc.* **109**, 3559-3568 (1987).
- ⁶ C.E.D. Chidsey, D.N. Loiacono, *Lang.* **6**, 682-691 (1990).
- ⁷ P. Yeh, Optical Waves in Layered Media (John Wiley & Sons, 1988).
- ⁸ M.D. Porter, T.B. Bright, D.L. Allara, C.E.D. Chidsey, *J. Amer. Chem. Soc.* **109**, 3559-3568 (1987).
- ⁹ Raman spectroscopy relies on the oscillating dipole of the electric field interacting with the molecule's polarizability. The selection rules for the Raman effect require molecular centrosymmetry. IR and Raman are complementary detection techniques.
- ¹⁰ W.S.V. Kwan, L. Atanasoska, L.L. Miller, *Lang.* **7**, 1419-1425 (1991) and references therein.
- ¹¹ G. Lopez, private communication.
- ¹² References on (111) nature of thermally deposited gold: C.A. Alves, E.L. Smith, M.D. Porter, *J. Amer. Chem. Soc.* **114**, 1222 (1992); C.A. Widrig, C. Chung, M.D. Porter, *Electroanal. Chem. Interfacial Electrochem.* **310**, 335 (1991); K. Reichelt, H.O. Lutz, *J. Cryst. Growth* **10**, 103-107 (1971).
- ¹³ X. Chen, E.R. Frank, R.J. Hamers, *J. Vac. Sci. Technol. B* **14**, 1136-1140 (1996) and references therein; E.R. Frank, X.X. Chen, R.J. Hamers, *Surf. Sci.* **334**, L709-L714 (1995) and references therein; R. Li, P. Bäuerle, E. Umbach, *Surf. Sci.* **331-333**, 100-104 (1995).
- ¹⁴ Handbook of X-Ray Photoelectron Spectroscopy, C.D. Wagner, W.M. Riggs, L.E. Davis, J.F. Moulder, G.E. Muilenberg, Ed. (Perkin Elmer, 1979).

- ¹⁵ R.G. Nuzzo, B.R. Zegarski, L.H. Dubois, *J. Amer. Chem. Soc.* **109**, 733-740 (1987).
- ¹⁶ J.J. Hickman, D. Ofer, C. Zou, M.S. Wrighton, P.E. Laibinis, G.M. Whitesides *J. Amer. Chem. Soc.* **113**, 1128-1132 (1991).
- ¹⁷ C.D. Bain, H.A. Biebuyck, G.M. Whitesides, *Lang.* **5**, 723-727 (1989).
- ¹⁸ G. Xue, M. Ma, J. Zhang, Y. Lu, K.T. Carron, *J. Coll. Interf. Sci.* **150**, 1-6 (1992); J.T. Young, F.J. Boerio, Z. Zhang, T.L. Beck, *Lang.* **12**, 1219-1226 (1996); Z. Zhang, T.L. Beck, J.T. Young, F.J. Boerio, *Lang.* **12**, 1227-1234 (1996); E. Sabatani, J. Cohen-Boulakia, M. Bruening, I. Rubinstein, *Lang.* **9**, 2974 (1993).
- ¹⁹ G.E. Poirier, E.D. Pylant, *Science* **272**, 1145-1148 (1996).
- ²⁰ G. Varsányi, Assignments for Vibrational Spectra of Seven Hundred Benzene Derivatives (Akadémiai Kiadó, Budapest, 1974).
- ²¹ J.M. Tour, L. Jones II, D.L. Pearson, J.J.S. Lamba, T.P. Burgin, G.M. Whitesides, D.L. Allara, A.N. Parikh, S.V. Atre, *J. Amer. Chem. Soc.* **117**, 9529-9534 (1995).
- ²² M.P. Seah, W.A. Dench, *Surf. and Interf. Anal.* **1**, 2 (1979).
- ²³ This difference is important due to the exponential nature of attenuation. An area of gold A covered by a film of thickness d will attenuate more than the sum of an area A/2 that is bare plus A/2 that is covered by a film of thickness 2d.
- ²⁴ L.A. Bumm, J.J. Arnold, M.T. Cygan, T.D. Dunbar, T.P. Burgin, L. Jones II, D.L. Allara, J.M. Tour, P.S. Weiss, *Science* **271**, 1705-1707 (1996).

Chapter Four. Device Fabrication

Once we have obtained a conjugated difunctionalized oligomer with known assembly properties, the next step toward accomplishing our goal of controlled oligomer placement across electrodes is to design and fabricate the metallic contacts down to the length scale of the oligomer. The goal of 10 nm gaps was approached in two ways. A vertical process was pursued that took advantage of the nanometer-scale vertical control of microfabrication processing. Metal-insulator-metal (MIM) stacks were fabricated with sub-10 nm insulator spacers between the two metal contacts, then cleaved to show the MIM face. This process had many distinct fabrication advantages, especially flexibility: independent choice of metals for top and bottom contact, easy integration of a gate, reliable access to sub 10-nm gaps. The ultimate limitation of this process was inconsistent electrode interfaces at the gap from the metal tearing at the cleave. The alternative was a planar gap process which relied on electron beam lithography to define sub 10-nm gaps in 100 nm wide gold lines. The planar gap process came about as a natural extension of the vertical process. With careful mask design, creative metal deposition, and optimization of the electron beam lithography, sub 10 nm gaps have been consistently achieved. To confirm that the gaps microfabrication processing was not incompatible with the oligomer self assembly mechanism, a series of surface analysis experiments similar to those described in Chapter 3 were performed. Although certain fabrication processes were problematic, the processing history of the gaps did not inhibit self assembly in the gaps region.

§ 4.1 Vertical Process for <10 nm Gaps

The vertical process was designed to take advantage of the tight vertical control of microelectronics fabrication processes; thickness control down to angstroms for metal and insulator deposition is standard. A stacked metal-insulator-metal (MIM) wire was fabricated with metal on top and bottom of a thin insulator, then cleaved in half to expose the inside (see Figure 4.1.1). The bottom electrode is buried in insulator so that the "junction" is only created when the wire is cleaved. The oligomers were to be assembled across this exposed face.

The processing for the initial MIM stack entailed four photolithography steps (see Figure 4.1.2).¹ The first lithographic step defined the bottom metal layer, or electrode; the second distinguished regions of thick and thin insulator; and the third defined the top metal electrode. The final lithographic step opened vias to the contact pads for the deposition of additional metal to facilitate bonding. The first three layers are shown in Figure 4.1.2 as they overlay each other – this set of 5 multilayer lines with their corresponding bonding pads are referred to as a die.

The substrates were silicon wafers, oxidized to 100 nm to prevent substrate leakage. The bottom electrode was defined as five parallel lines, each 4 μm wide separated by 16 μm , extending 100 μm across the center of the chip between two contact pads, one on either side of the intended cleave plane. This electrode was ~20 nm of thermally deposited gold with a thin layer of titanium used to enhance adhesion to the oxidized substrate. The gold thickness was kept to a minimum to reduce the number of possible oligomer binding sites at the electrode interface after cleaving.

A thin oxide separated the electrodes in the region of the cleave. The anticipated length of the oligomers limited the oxide thickness to less than 10 nm thick. The thin oxide

was not used everywhere due to a concern about leakage paths between top and bottom electrodes. The oxide provided a conduction path parallel to the oligomers; assuming the oligomers were one-dimensional wires with a resistance of $25\text{k}\Omega$, a leakage path of greater than $10\text{M}\Omega$ was deemed suitable. A field insulator of 200 nm silicon nitride was deposited, then a central region was opened for deposition of the thin device oxide. The preferred mask for the thin oxide opened a central $100\text{ }\mu\text{m} \times 100\text{ }\mu\text{m}$ window (see Figure 4.1.2b). An alternative mask defined smaller regions of thin device oxide: windows ($2\text{ }\mu\text{m} \times 5\text{ }\mu\text{m}$) were opened on top of the bottom electrode lines in a staggered array (see Figure 4.1.2c). This arrangement was designed to increase the probability of a cleave intersecting a region of thin oxide while minimizing device leakage by reducing the direct overlap of top and bottom electrodes in regions of thin oxide. When experimental results indicated that leakage was not a problem, further processing was done with the large window mask, greatly increasing the yield of the physical cleave.

A variety of thin insulators were characterized electrically and by atomic force microscopy; best electrical results were obtained with aluminum oxide. Two oxide processes were tested: electron beam deposition of AlO_x , and post deposition oxidation of thin layers of Al. Thin oxides were characterized by atomic force microscopy (AFM). The grain size was of concern due to the oxide thickness constraint and proximity of the two electrodes. If the surface roughness were too great, a high resistance path would not be achieved simply due to the thickness of the layer not allowing for multiple grain build up to close off all parallel paths. AFM data of a nominally $85\text{ }\text{\AA}$ AlO_x film deposited by electron beam evaporation show surface average roughness on the order of $20\text{ }\text{\AA}$ across a $0.5\text{ }\mu\text{m}$ size field (see Figure 4.1.3a). Electrical measurements on MIM structures yielded resistances of order ohms for these thicknesses. The alternative method for aluminum oxide deposition was to sequentially evaporate 1.0 - 1.5 nm of aluminum by resistive heating, and oxidize in air 12-24 hours. The deposition was repeated as necessary to achieve the desired AlO_x thickness. AFM data of these films indicated an average

roughness of 10Å (see Figure 4.1.3b); electrical resistance of these oxides was 10^6 times greater than those deposited by electron beam evaporation.

The top metal electrode layer was defined by the third photolithography step; five parallel lines, widths ranging from 2 to 4 μm and separated by 16 to 18 μm , extended 100 μm across the center of the chip aligned directly above the bottom electrode (see Figure 4.1.2b). Unlike the bottom electrode, each of these lines was individually addressable. This electrode was ~25 nm of gold with a thin layer of titanium to enhance adhesion. The final lithographic step opened windows on the contact pads for the deposition of additional metal to facilitate bonding.

The resulting die surface showed gold bonding pads and lines, and silicon nitride insulation. It would be undesirable to have the molecules self assemble everywhere on the die, providing parasitic conduction paths, for instance, between bonding pads. The materials selected alleviated this concern: the selectivity of thiols for gold over nitride has been shown to be better than 100:1.²

Typically one quarter of a two-inch silicon wafer was processed at a time, producing an array of 10 rows \times 8 columns of die with the possibility of ten junctions per die (two sets of 5 each). The columns were cleaved perpendicular to the electrode lines; chips with fortuitous breaks in the critical region of thin oxide were reserved for electrical measurement and scanning electron microscopy (SEM). Electrical measurements were performed on a probe station with a Hewlett Packard 4145B Semiconductor Parameter Analyzer, with maximum current resolution 0.05 pA. Current versus voltage measurements were done with the sample at room and liquid nitrogen temperatures. The resistance between top and bottom electrodes was frequently 100 M Ω or higher, tested before cleaving. However, the scanning electron micrograph of a cleaved junction depicted in Figure 4.1.4a shows that the metals did not reliably cleave at the junction. Rather than

cleave, the malleable gold tore in an irregular fashion. Some devices had no top electrode metal up to the junction edge, while others had flaps of metal hanging over. This behavior appeared to be more pronounced at lower temperatures (see Figure 4.1.5). Other materials may cleave more uniformly and reliably; however, we were limited to certain materials dictated by the self-assembly process. For example, titanium is brittle when cold³ and may cleave as desired; however, there is no evidence for self assembly of thiols on titanium, so the entire electrode could not be made out of titanium. Samples were fabricated with electrodes of thick titanium and a thin gold top layer. These depositions were done by electron beam evaporation, the only method we have available to reliably deposit 50 nm of titanium in a single vacuum cycle. It is possible that the titanium arrived at the substrate hot enough to hardbake the photoresist; liftoff consistently failed on these samples. An alternative would be to fabricate electrodes of a two-element alloy, containing one metal appropriate for self assembly, and another with the mechanical properties more suitable for reliable cleaving. Increasing alloy composition for gold, silver and copper (three metals known to self-assemble thiols⁴) can decrease the metal grain size⁵ which should make a better cleave. An additional concern with such alloys, however, would be the possibility of forming simultaneous metal-thiolate bonds on two or more metals, or a hybrid metal 1–oligomer–metal 2 bridge. Each bond should be characterized by its own barrier height; such a possibility would complicate analysis of electrical characteristics.

Ideally the multilayers would have been individually characterized, and an analysis of the junction could have been done before and after oligomer self-assembly. The individual metal layers were not resolved by SEM due to their extreme thinness. The sample shown in Figure 4.1.5 is a gold-insulator-gold multilayer, but the bottom electrode layer is barely resolvable. AFM has better lateral resolution than SEM, as well as the capability for obtaining vertical information; the completed structures were also analyzed using AFM. The sample was mounted for AFM such that the cleaved edge faced up. The tip rastered across the cleaved substrate and MIM sandwich, then "fell off" the sample. An

AFM image obtained in this manner is shown in Figure 4.1.6. The top and bottom electrode are distinguishable in this image, however the image is distorted due to the size of the cantilever tip and possibly the lateral force between the tip and the sample. Regardless, the electrode tearing is observable here as it was in the SEM analysis.

An advantage of the cleave process is the facility of independently changing metals for the individual electrodes. Since the top and bottom electrodes are formed by distinct lithographic and deposition steps, they need not be the same element. Although the TE oligomer systems are symmetric, designed to be conducting wires, it has long been proposed to synthesize a molecular rectifier, with an electron-donating group at one end separated from an acceptor group at the other by a σ bridge.⁶ It would be desirable to measure such a molecule in a controlled orientation. If the electrodes were fabricated with different metals, the molecule could be self-assembled in an oriented fashion by having the different functional groups self-select for different metals.⁷ It may become advantageous for such a molecule to be gated, thereby controlling the energy barrier between the donor and acceptor; a third metal contact may be easily incorporated into the cleave process as a gate (see Figure 4.1.7). Aluminum may be suitable since the surface would provide its own gate oxide upon cleaving.

The eventual goal of this project was to measure conduction through a single oligomer chain self-assembled across a small gap. A limitation of the cleave process is the relatively large number of equivalent sites available for a chain to self-assemble across the gap. Thiol terminated alkane chains adsorb onto gold (111) at a third of a monolayer coverage, one thiolate to three gold atoms.⁸ The coverage for conjugated oligomers is not known; alkanethiolate packing should provide a reasonable lower estimate. Assume that a 1 μm wide gold line cleaves to show a perfect (111) face of fcc gold 10 nm thick; there are about 10^5 sites available for binding. Of these, only the sites closest to the insulator will allow the bound chain to extend across the gap. Excluding any externally applied sources

of anisotropy, the chains will bind in all directions. Conservatively, on order 10^4 chains may bridge the gap. To increase the chances of measuring a junction with only one oligomer chain, one may use a dilute solution of oligomer and monitor the gap conductance; the device would be removed from the solution upon detecting a change. Another possibility to limit the available sites would be to define the top electrode using electron beam lithography; for example, simply reducing the width of the top electrode line from $1\text{ }\mu\text{m}$ to $0.1\text{ }\mu\text{m}$ reduces these available sites by at least an order of magnitude. A mask was designed for this process, and electron-beam defined electrodes were written on test samples (see Figure 4.1.8) but the fabrication was not pursued on device structures due to the materials problems discussed.

In summary, the cleave process was designed to take advantage of the tight vertical control available in microelectronics fabrication. Junctions of an appropriate size and electrical resistance were fabricated with a high yield process, and the device lent itself well to future applications. However the limitation of the process was the materials' behavior upon cleaving. Use of an alloy may address the tearing of the electrodes, but would introduce additional complexity into the electrical analysis, presuming that stage were reached. The electron beam written final embodiment of the vertical cleave process led to the next device structure explored, the lateral gaps device.

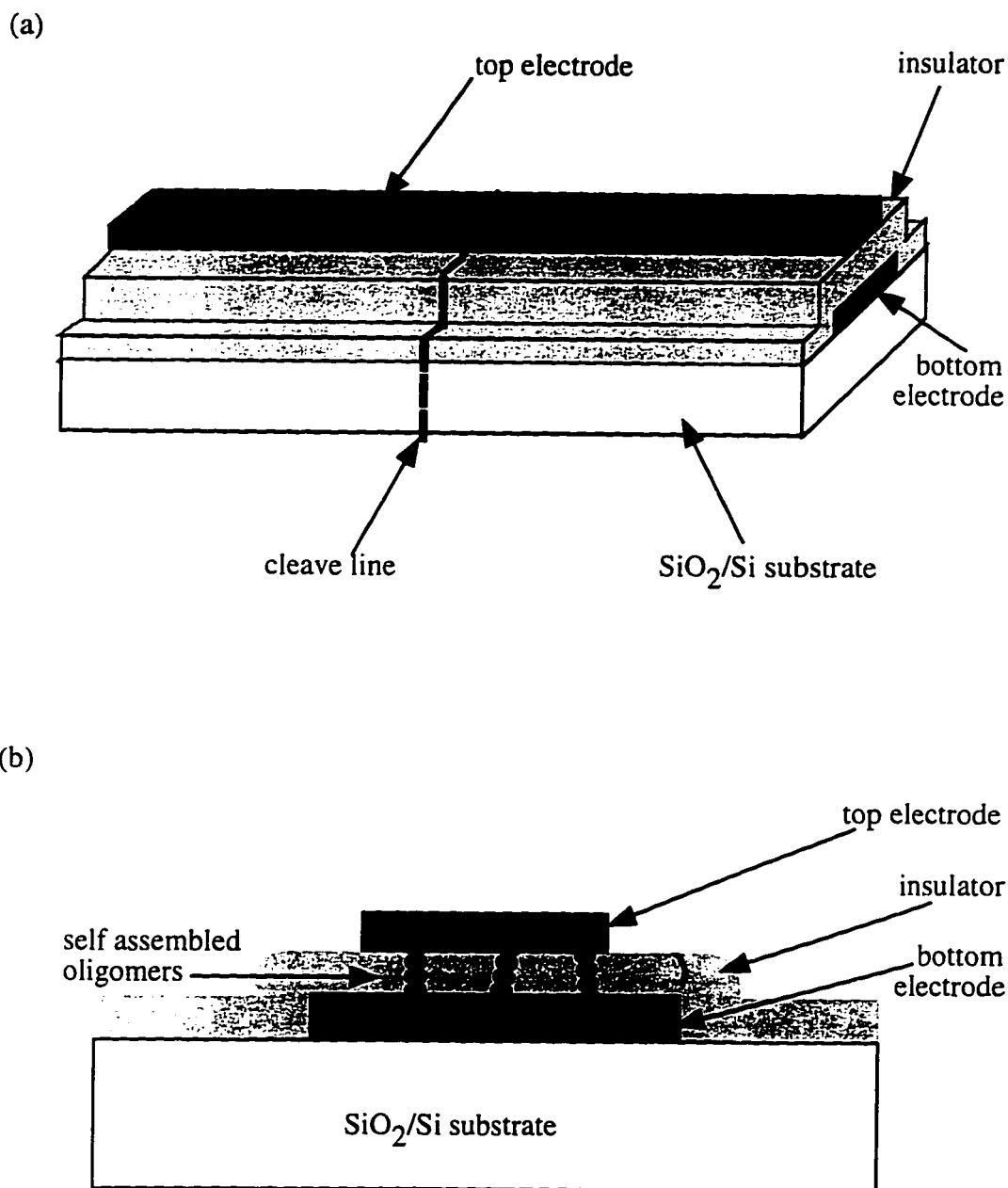


Figure 4.1.1 Schematic views of a metal-insulator-metal multilayer wire for the cleave process. (a) Side view of the multilayer before cleaving. The bottom electrode is buried in insulator. The dashed line indicates the cleave plane. (b) End view of the cleaved face of the multilayer with oligomers bridging the gap.

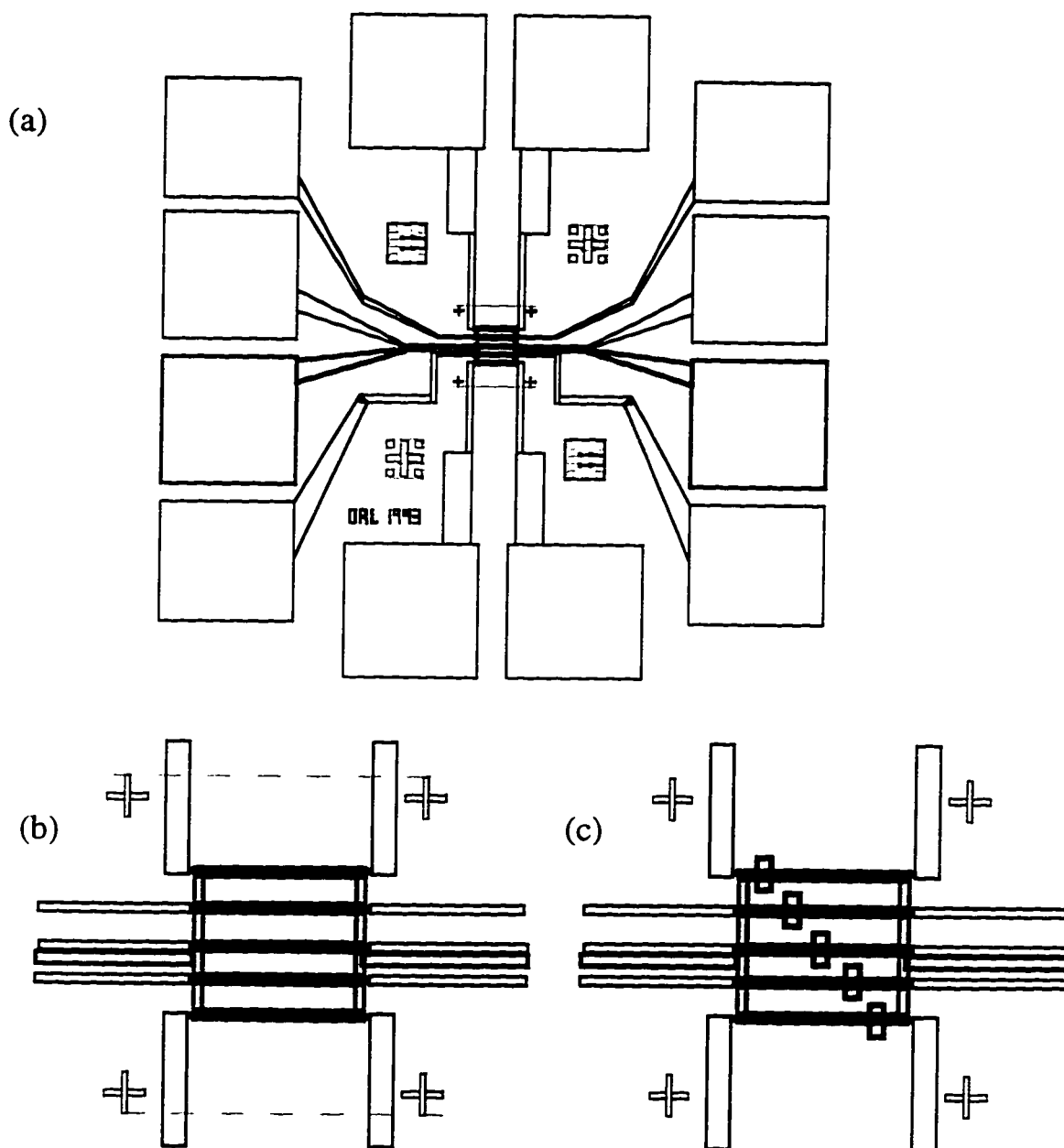


Figure 4.1.2. Photolithography masks for fabricating cleave structures. The top electrode is outlined in black, and the bottom is in gray. (a) Entire die with bonding pads, measuring about 1mm on a side. (b) Closeup of the central $100\mu \times 100\mu$ region of thin oxide, delineated by a dashed line. The cleave would intersect all 5 lines in this region, creating two sets of 5 parallel devices. (c) Closeup of central region showing mask for small windows of thin oxide. The cleave would hopefully intersect at least 1 of the small thin oxide windows.

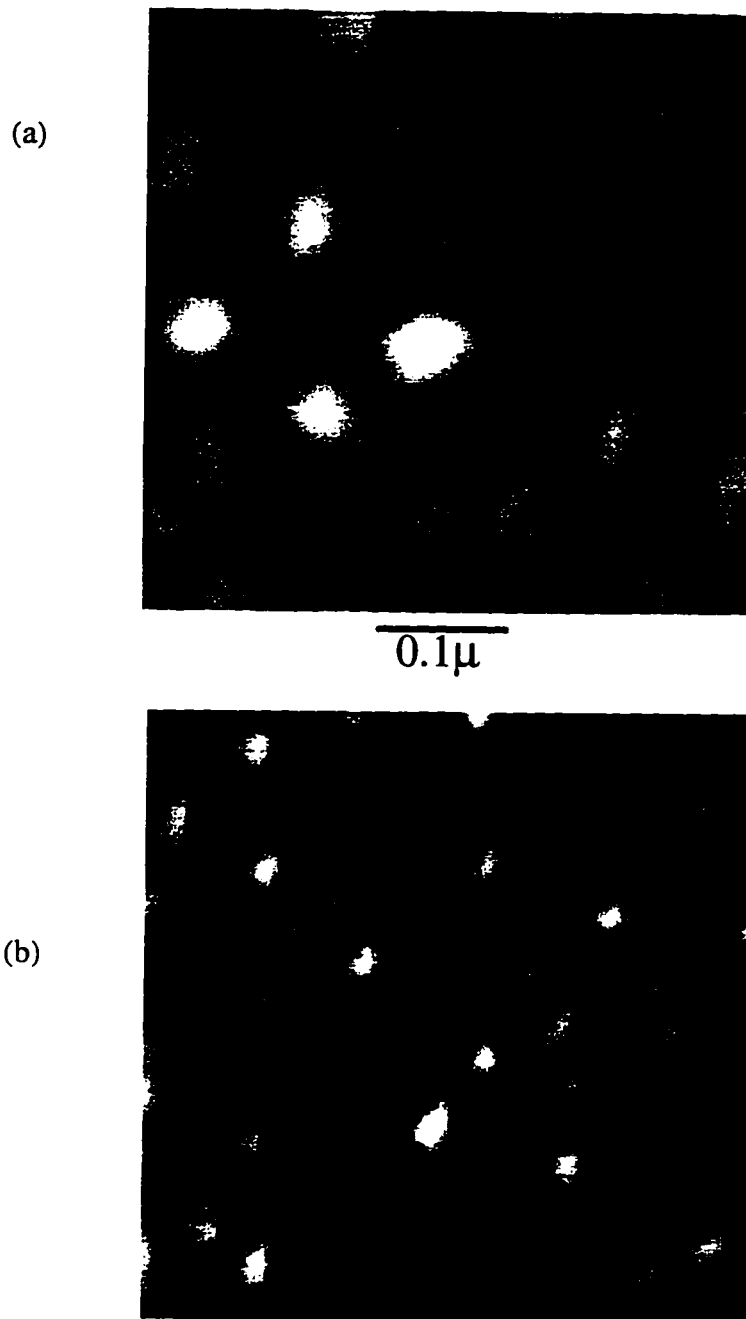


Figure 4.1.3 AFM images of AlO_x deposited by (a) electron beam evaporation of AlO_x and (b) resistance heating evaporation and oxidation of Al. The average roughness of the film in (a) is 20\AA , and the electrical resistance is of order ohms. The average roughness of the film in (b) is 10\AA and the electrical resistance is of order $\text{M}\Omega$.

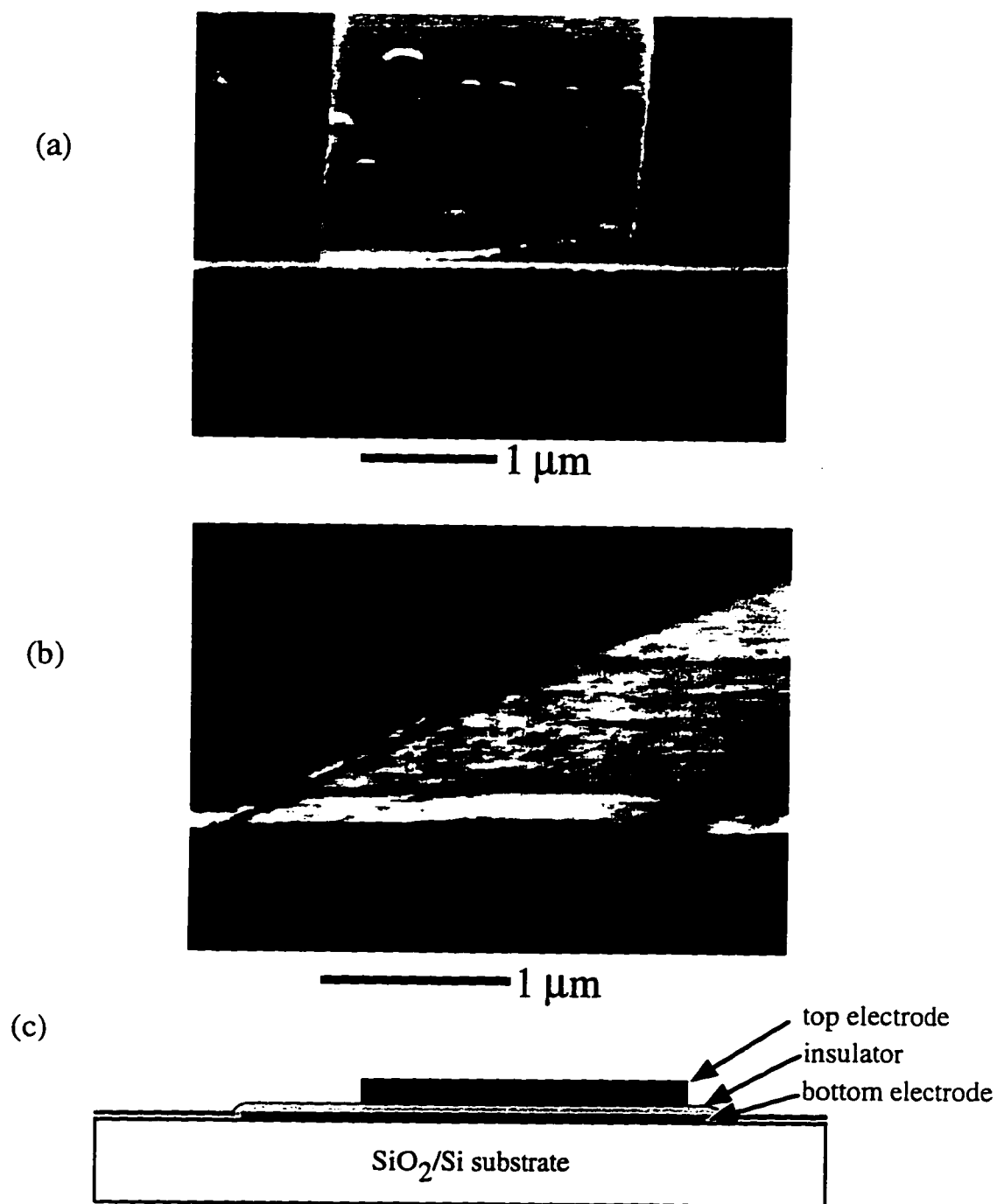


Figure 4.1.4 (a) Scanning electron micrograph (SEM) of a cleaved junction viewed edge on showing gold tearing. The top electrode does not extend uniformly to the cleave plane. (b) SEM of a junction cleaved through small oxide window viewed edge on. (c) Schematic of the fabricated structure shown in (a).

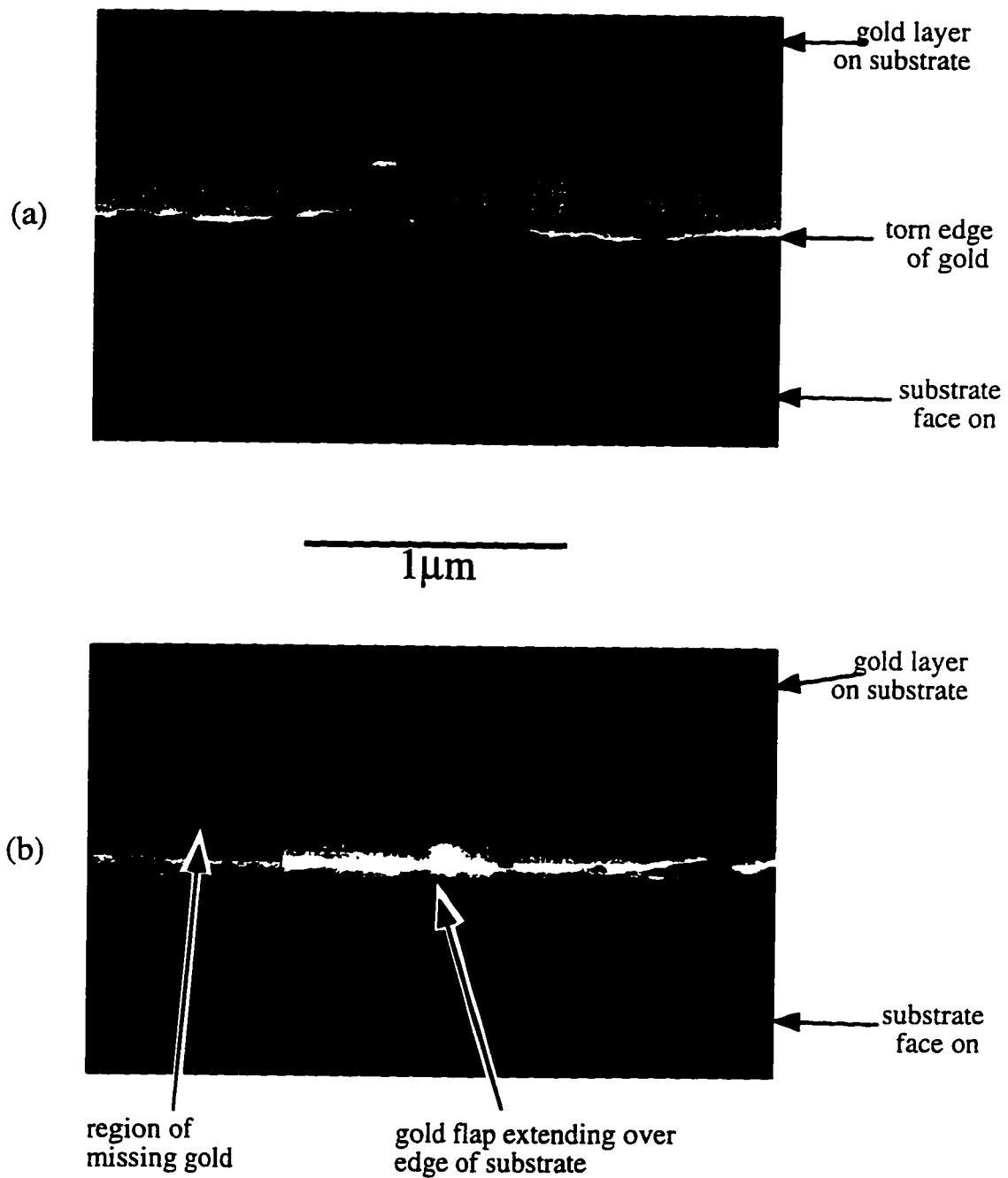


Figure 4.1.5 Edge-on scanning electron micrographs of blanket depositions showing irregular tearing of gold at the cleave plane. Samples are viewed at room temperature. (a) Sample cleaved at room temperature. (b) Sample cleaved at liquid nitrogen temperature.

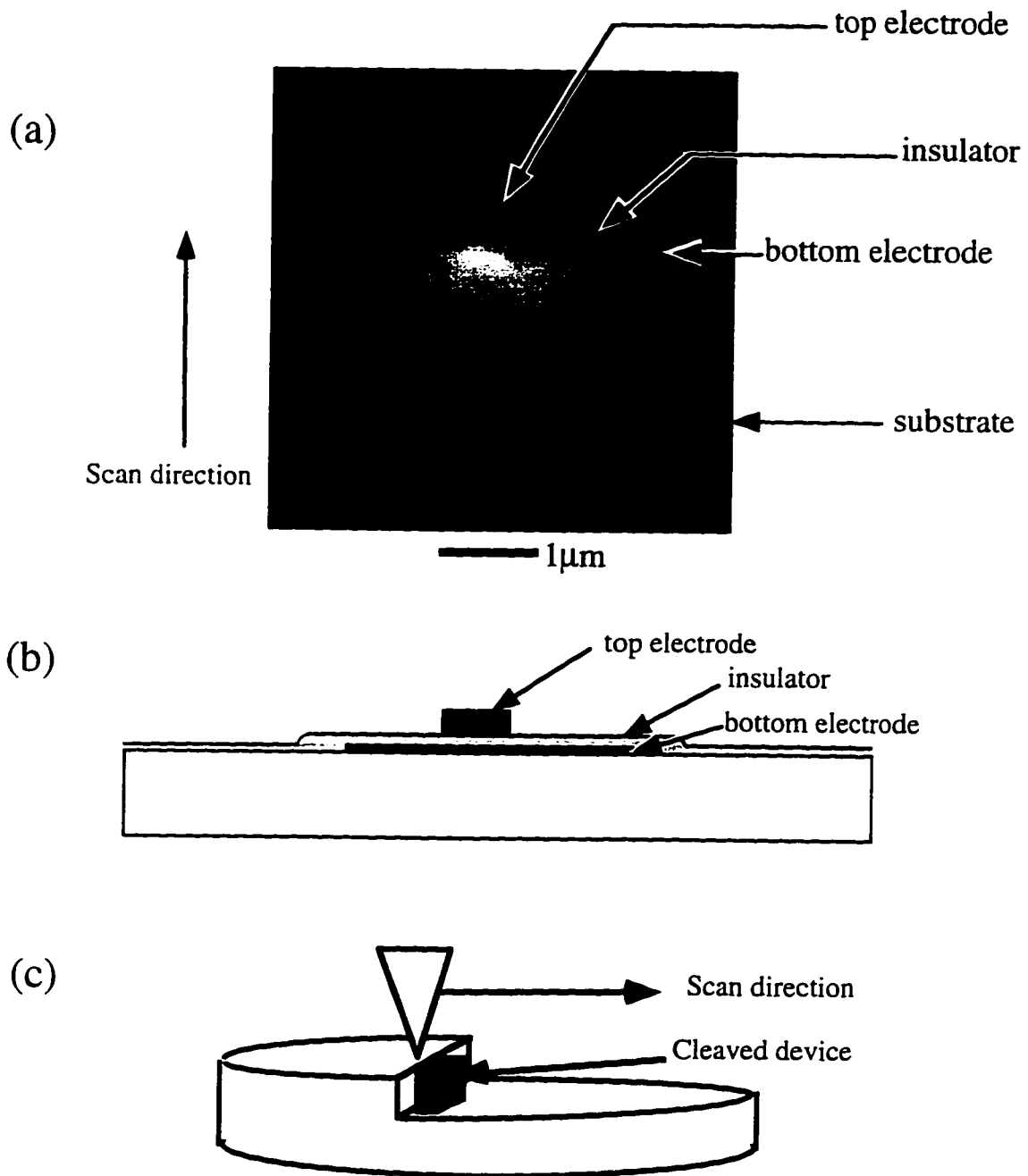


Figure 4.1.6 (a) AFM image of a cleaved junction showing the narrow top electrode, insulator and wider bottom electrode on a cleaved substrate. The torn gold flaps over the substrate. The scan direction is vertical. (b) Schematic of MIM stack scanned. (c) Schematic of sample mounted face-up for scanning. The scan direction as depicted is left to right. [Image courtesy of M. Amman.]

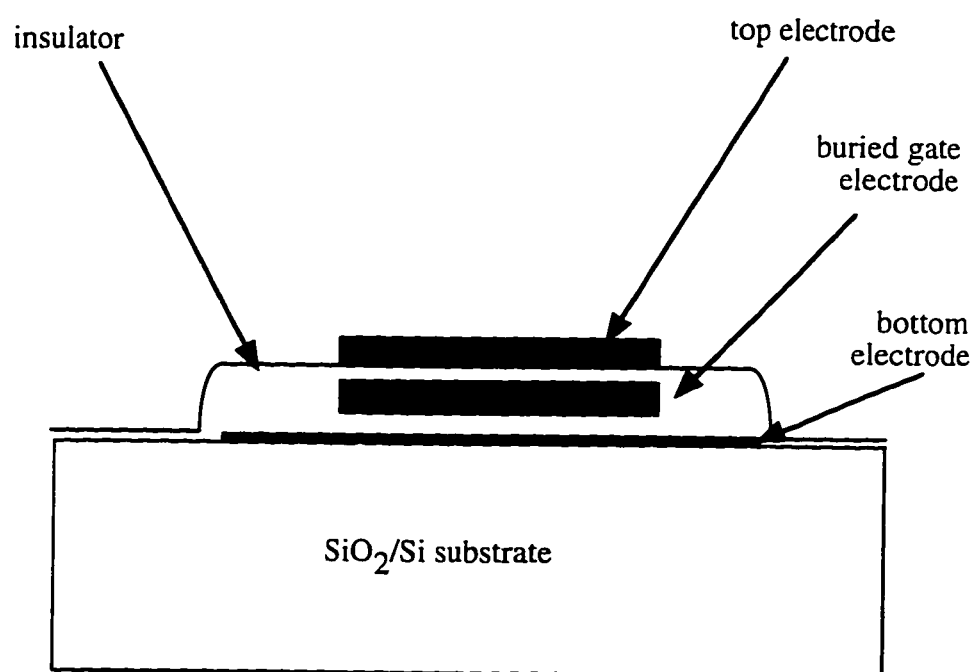


Figure 4.1.7 Schematic of three electrode version of cleave structure for gating oligomers.

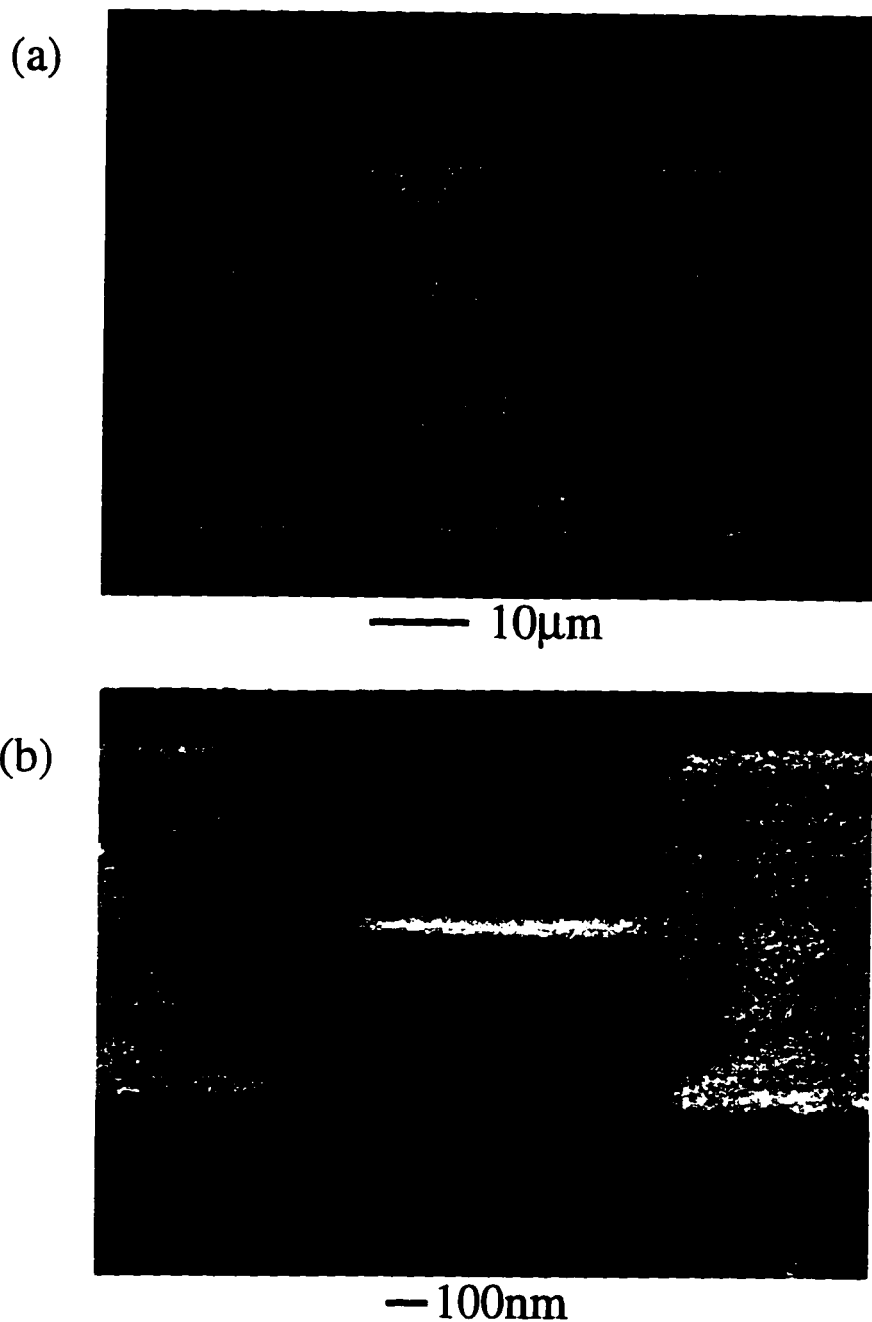


Figure 4.1.8 (a) SEM of e-beam written top electrode for cleave process. The top electrode was displaced from the bottom electrode except in the region of thin oxide to minimize leakage currents. In the region of thin oxide, the electrode width was reduced to 100 nm to reduce the number of equivalent binding sites (see text). (b) Closeup of region to be cleaved.

§ 4.2 Planar Gaps Process

The planar gap process came about as a natural extension of the e-beam written top electrode pattern from the cleave process. Once the fine features were defined for the top electrode as seen in Figure 4.1.8, an attempt was made to create a small gap in the e-beam written feature for a single layer, dual electrode. At that time, the resolution limit of our electron beam lithography system was of order 20 nm; it was uncertain what gap size was achievable with this process. With careful mask design, creative metal deposition, and optimization of the e-beam writing, sub-10 nm gaps have been consistently achieved.

Substrates were n-type Si (100) wafers, with resistivity of 1-100 Ω -cm. A 100 nm dry thermal oxide was grown to prevent substrate leakage. In preliminary tests, thinner oxides were tried (20 nm and 74 nm); many of the devices were shorted to the substrate after mounting and bonding. The thicker 100 nm oxide seemed to have an almost 100% yield for insulating devices post bonding. The first photolithography step defined the bonding pads and leads to the central 100 \times 100 μm^2 region, similar to the cleave process. The second photolithography step opened vias for additional metalization on the bonding pads. Typically, the leads were 20 nm gold on a thin layer of titanium for adhesion (deposited by thermal evaporation), and the bonding pads metalization was 200 nm of gold deposited in the electron-beam evaporation chamber. After photolithography, the substrate was prepared for e-beam lithography. A PMMA (poly (methyl methacrylate)) bilayer resist was formed in the following manner: the first layer was a low molecular weight (150k) PMMA, mixed to 5% in MIBK (methyl isobutyl ketone), spun on at 4k rpm for 60 seconds, then baked at 170°C for 1 hour; the second layer was 950k molecular weight mixed to 2% in MIBK. The spin rate was quickly ramped from 3k to 8k rpm, and spun for 60 seconds. The substrate was then baked at 170°C for an additional hour.

Electron beam writing created a pattern of lines and gaps in the central $100 \times 100 \mu\text{m}^2$ region (see Figure 4.2.1). A broad processing window was built into the dose range and the nominal gap size range. For any given sample, a range of doses was used to insure open gaps somewhere on most dies. The e-beam writing was done on a converted JEOL at 8mm working distance. The final process used a 10 nm pixel size, 40 keV electrons, and a current of 3.6pA. Each die took approximately 30 minutes to write. Pattern development was done in 1:3 MIBK: isopropyl alcohol (IPA) for 30 seconds, then rinsed in IPA for 30 seconds, and dried with N_2 . During development of the bilayer resist, the lower molecular weight PMMA (bottom) layer dissolved more readily than the higher molecular weight (top) layer. The resulting structure was a suspended bridge of high molecular weight PMMA. In the preliminary process, the metal deposition was done in the standard fashion, with the evaporation normal to the substrate surface. It was later found that a smaller gap was attainable by tilting the substrate 15° to normal and performing sequential angled evaporations; this was achieved by tilting the substrate holder in the deposition chamber.⁹ This process relied on the suspended PMMA bridge to allow the deposited metal to extend under the bridge from either side. The net result was a smaller gap than the one nominally written and developed. The morphologies of the direct versus angled depositions are shown in Figure 4.2.2. All molecular depositions to be discussed in Chapter 5 were done on angle-evaporated gaps. A similar bilayer resist process has been used to form 25 nm gaps by direct evaporation.¹⁰

Gaps were tested on substrate before cleaving. Initially there were some problems making contact between the e-beam written features and the photolithographically defined leads. AFM of the leads occasionally showed sharp edges. The cause for this was never identified. It was observed, however, that these sharp edges rarely occurred on more than two sides of a structure at a time. For example, if there were sharp edges on the north face and the east face, then the south and west faces were generally smooth. The e-beam mask

was modified to include contacts coming in to the photolithographic leads from three sides. An alternative to these additional contacts would have been to increase the total area of the e-beam written contact to include that of the photolithographic lead; this path was not pursued because it would have added considerably to the e-beam exposure time. The mask redesign alleviated the contact problem.

One of the earliest lessons on handling these small gaps concerned their fuse-like nature. After a large number of gaps melted or vaporized, a SEM study was done to check the gaps' integrity after each of the following steps: testing on substrate, cleaving, mounting, and bonding. No failure pattern emerged from this analysis. Routine handling seemed sufficient to cause the damage, presumably due to electrostatic discharge. Thereafter, handling of the headers was minimized, and the header leads were kept shorted as long as possible. Finally, a mask redesign was incorporated to facilitate electrical verification of die integrity; the largest gap in the e-beam mask was replaced with a solid line to provide an electrical check for damage when it was non-trivial (if not impossible) to use a microscope for optical verification (for instance, while the header was in the deposition chamber– see Chapter Five). It also allowed for an easy check of the photolithographic leads' electrical contact to the e-beam written features as discussed above. The final version of the e-beam mask is shown in Figure 4.2.3.

Background currents for electrical measurements made on the gaps while in solution were of order nanoamps at 1V. (Further discussion of solution measurements will be presented in Chapter Five.) To reduce these currents, all electrode surfaces were insulated except the actual gap region. The insulation needed to be impervious to strong organic solvents; SiO₂ and SiN_x were considered. After the gaps were fabricated, the entire substrate was covered with 350 nm SiN_x by plasma enhanced chemical vapor deposition. This process required the substrate to be held at an elevated temperature for the duration of the deposition (1 hour at 300°C), and another thermal cycle to densify the

nitride (1 hour at 300°C). The integrity of the gaps after the thermal cycles was verified by SEM and electrical characterization. A single layer PMMA resist was spun, and small windows were opened by e-beam lithography over the gaps region. Alignment capabilities of the e-beam lithography system limited the windows to minimum $5 \times 5 \mu\text{m}^2$, to insure overlap with the gaps. The SiN_x was removed by a wet etch process that also attacked the thermal oxide substrate at a slower rate. Partial removal of the underlying substrate in the gaps region alleviated the possibility of steric hindrance from the substrate in the self assembly of the oligomers.

In summary, sub-10 nm gaps were routinely fabricated using electron beam lithography with a bilayer resist and angled metal depositions.¹¹ The final e-beam mask incorporated a multiple contact structure to insure electrical contact between photolithographic and e-beam lithographic features, and a solid line to verify this contact as well as the integrity of the gaps on the die. Precautions were necessary in handling these devices to guard against electrostatic discharge. Finally, an insulation step was integrated into the process to reduce electrode area in solution.

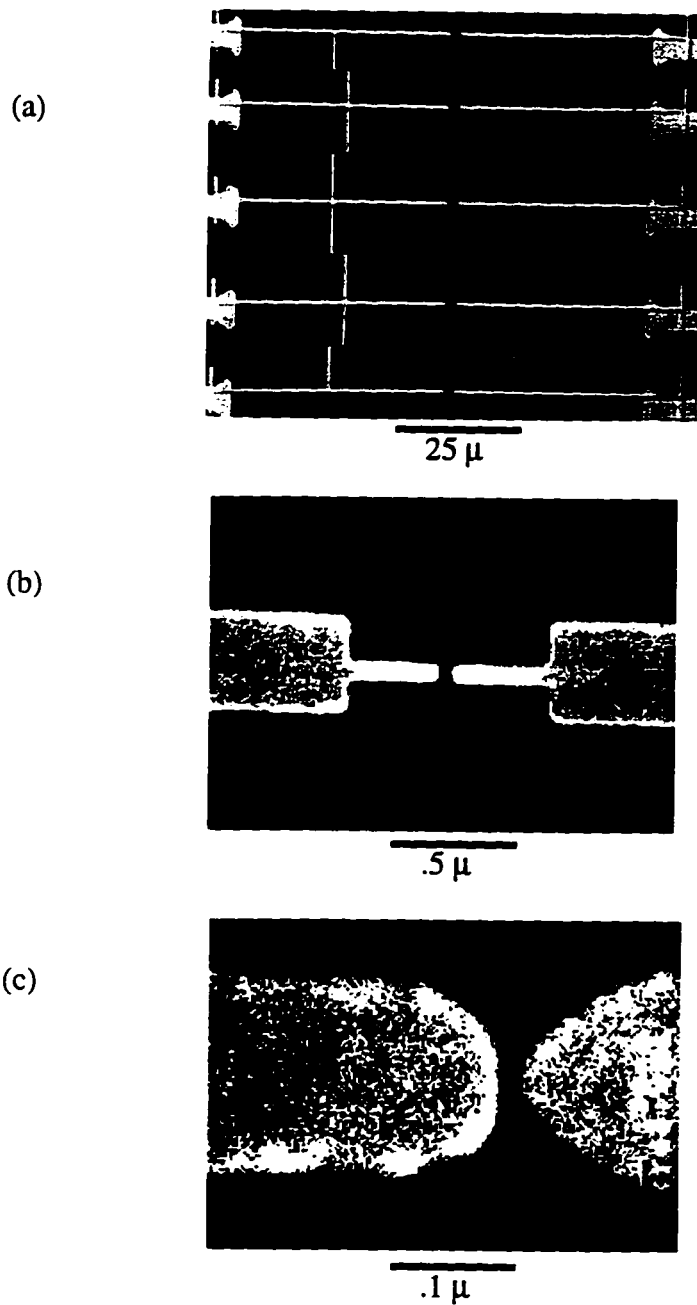


Figure 4.2.1 Scanning electron micrographs of a lateral electron-beam defined gap structure. (a) A closeup of the central $100\mu \times 100\mu$ region of structure.

(b-c) Progressive closeups of the gaps region.

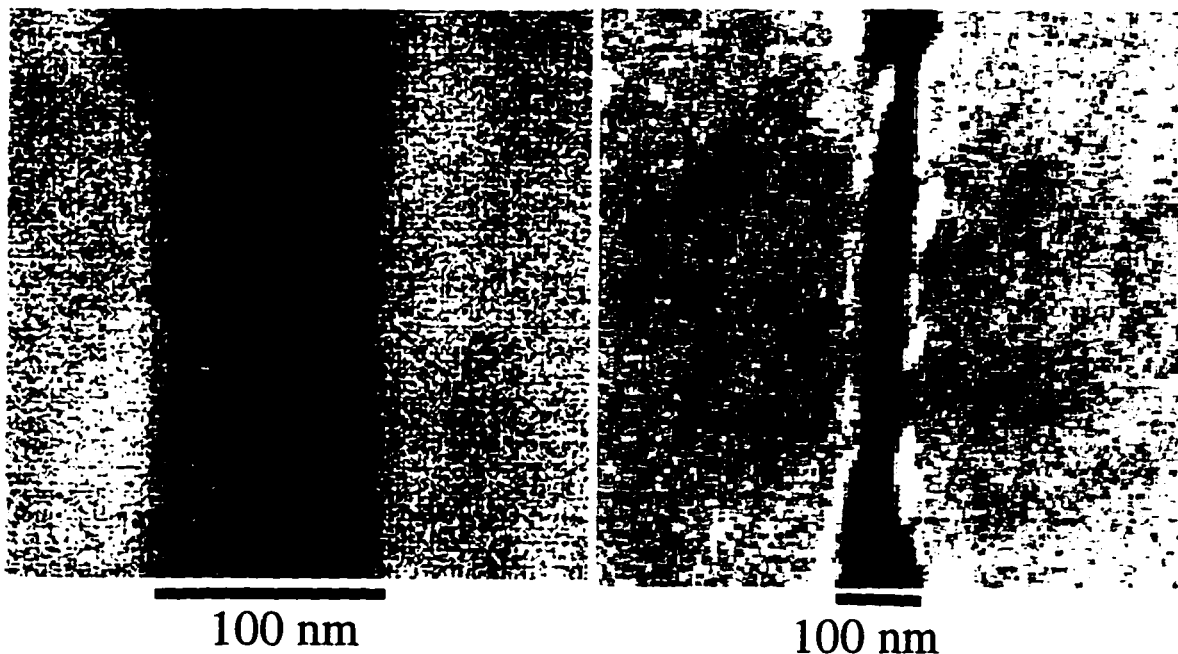
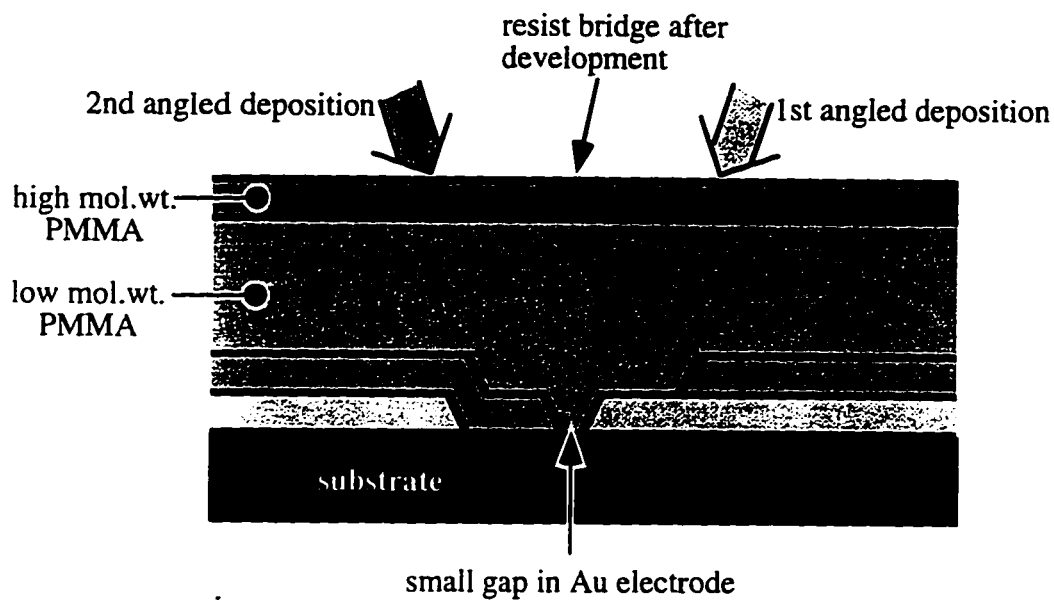


Figure 4.2.2 (a) Schematic of the angled deposition procedure for evaporating gaps smaller than as-written. (b) Scanning electron micrographs of comparable as-written gaps. On the left, a sub-100 nm gap formed by angle evaporation. The resist bridge was of order 100 nm; angle evaporation reduced the gap size by at least a factor of two. On the right, a gap formed by direct evaporation.

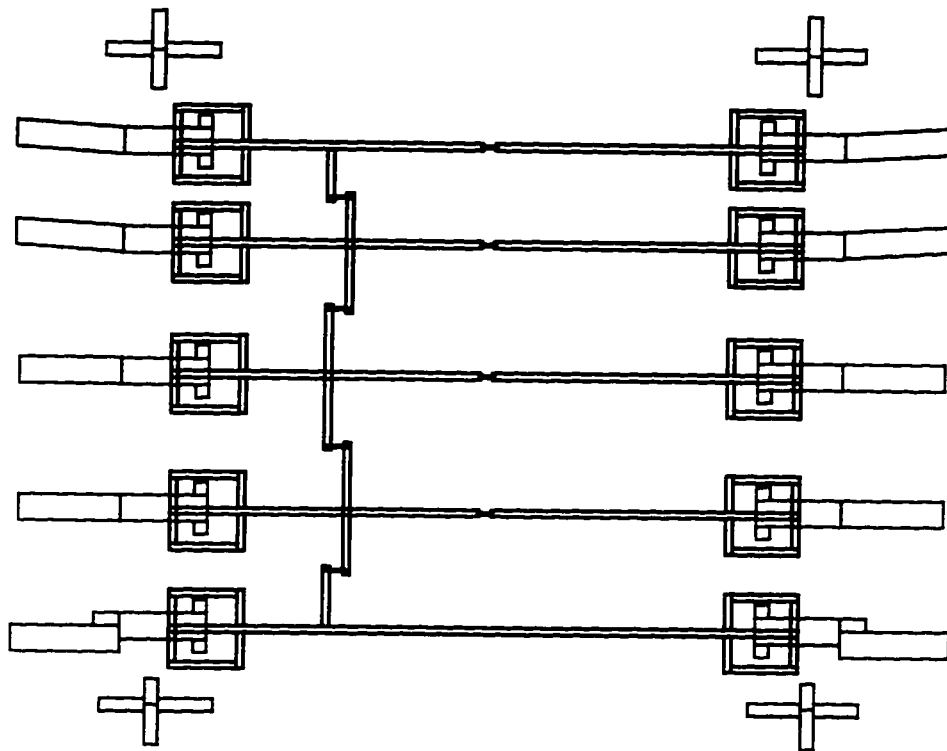


Figure 4.2.3 Electron beam lithography pattern (in black) to define small lateral gaps. The solid line for electrical testing connects the bottom two electrodes, left to right. The e-beam pattern extends 100 μm on a side. Photolithographically defined leads and alignment marks are in grey.

§ 4.3 Compatibility of Microfabrication Processing and Self-Assembly

The eventual goal of this project was the self-assembly of the difunctionalized TE oligomers on microfabricated electrodes to explore their electrical properties. Therefore it was important to verify that the standard microfabrication processes would not inhibit assembly. The self-assembly experiments discussed in Chapter Three were performed on fresh gold substrates. The history of these substrates did not closely mimic the processing history of microfabricated devices, and therefore the surfaces to which we eventually hoped to self-assemble functionalized conjugated oligomers. In particular, the compatibility of self assembly with lithography was a concern. Lithography involves the deposition and selective removal of long chain hydrocarbon polymers. Published results of pyrrole electrodeposition on microfabricated electrodes indicate behavior consistent with the presence of a thick insulating layer on the electrodes, even after an oxygen plasma clean and an extensive electrochemical clean. A possible explanation for this behavior is resist residue coating the electrodes and inhibiting electrochemical response in solution.¹² In other work with microfabricated electrodes, Hickman *et al.*¹³ directly claim that photoresist residue on electrode surfaces is responsible for irreproducible derivatization results. Although their fabrication and molecule attachment processes are not identical to ours, the concern with resist residues was deemed worthy of investigation.

A series of experiments were performed to explore the compatibility of the two resist processes involved with gaps device fabrication: photolithography and electron beam (e-beam) lithography. These processes are performed sequentially in the gaps device fabrication. The first features defined are large ($100 \times 100 \mu\text{m}^2$) bonding pads with 10 μm lines leading from the pads to the central $100 \times 100 \mu\text{m}^2$ region of the chip (see Figure 4.1.2a). The features are formed by photolithography using a liftoff technique. When using liftoff to form structures, the final (metal) pattern is exposed to the resist only during

the solvent dissolution of the resist. The definition of the smaller central lines (and gaps) is accomplished by e-beam lithography. This fabrication sequence means that while the e-beam written features are only exposed to a resist (PMMA) during liftoff, the larger photolithographically defined features have a dual exposure: first to photoresist during liftoff; second to PMMA as it is spun onto the wafer and baked before e-beam exposure. In these experiments, the conditions for both liftoff and resist spin and bake were mimicked, after which the wafers were put through the usual procedure to form a SAM. In some cases, a monofunctionalized TE oligomer (TE₄S) was used; in others, a simple *n*-alkanethiol (hexadecanethiol, C16). Analysis included ellipsometry before and after each step, and grazing angle IR reflectance spectroscopy to determine whether ML formation had proceeded as expected.

Fresh gold substrates were prepared as previously described¹⁴ to provide a known baseline for ellipsometry and IR. To mimic photolithography liftoff exposure, a few ml of Shipley 1400-27 resist were put into 200 ml of acetone. To simulate e-beam lithography, a few ml of each of the PMMA/MIBK solutions used to form a bilayer were put into 200 ml acetone: 5% by weight 150k MWt, and 2% by weight 950k MWt. The fresh gold substrates were left in this solution for 1 minute, then rinsed twice with acetone, once each in methanol and distilled water, and blown dry with N₂. After PMMA liftoff, 10-12 Å of residue remained on the surface as measured by ellipsometry (see Table 4.3.1). ML formation proceeded as expected, as determined by ellipsometry and IR; if a residue had been left after ML formation, the IR spectra should have shown additional disorder in the ML as well as the signature of the resist residue; the ellipsometric values would also have been thicker, reflecting the contributions from both resist residue and ML thicknesses. The wafers exposed to photoresist liftoff also formed ML (no ellipsometric data were available for these samples). We conclude that liftoff residue from either process, photolithography or e-beam lithography, is insufficient to inhibit monolayer formation.

The spin and bake cycle was incorporated for each of the resists. For photoresist, Shipley 1400-27 resist was spun onto 3 day old gold substrates at 4000 rpm for 40 sec. The wafers were then baked at 86°C for 270 seconds. Half of the wafers were flood exposed (2.2 mW/cm^2 at $\lambda_m=315 \text{ nm}$) and developed for 1 minute in Shipley 351 developer diluted 1:4 with deionized water (DI), rinsed in DI and blown dry with N_2 . The other half were stripped in acetone 60 seconds, rinsed with acetone, IPA and DI 60 seconds each, then N_2 blown dry. According to ellipsometry, both the flood expose and develop process and the acetone strip process left a residue of 13-14 Å. In both cases, the C16 SAM gave the expected IR spectrum and ellipsometric thickness (see Figure 4.3.1). For electron beam resist, the standard bilayer was formed by spinning first low molecular weight PMMA at 4000 rpm for 40 sec, baking the wafers at 170°C for 1 hour, spinning the second (high MWt) layer for 40 seconds, ramping the rpm from 3000 to 8000, and baking for an additional hour at 170°C. The resist was stripped 3 days later by soaking the wafers in acetone for 30 minutes. The wafers were then rinsed in acetone (5 min), EtOH (1 min) and DI. Ellipsometric thickness of the residue was over 100Å. The wafers were submerged into a 1 mM solution of C16 in EtOH for 4 days. The surface did not dewet upon removal from the solution, unlike a pure C16 ML. No C16 ML formation was evident by IR (see Figure 4.3.2).

The ellipsometry and IR results indicate that although the liftoff process may leave residue on the gold from both resists, this residue is insufficient to inhibit self assembly. Even the residue left from a baked on photoresist, regardless of the removal process, did not prevent ML formation. However the baked PMMA residue was tenacious, completely resisting sonication in acetone and only somewhat susceptible to sonication in 1,2,4-trichlorobenzene (loss of $\sim 20\text{Å}$ in 20 minutes). Since the active surfaces for the gaps devices are only exposed to PMMA during liftoff, they should be suitable for self-assembly.

To confirm these results on the actual devices of interest, a deposition of monofunctionalized TE₄S was done at Yale with a microfabricated die. Auger Electron Spectroscopy (AES) analysis was used to detect the element sulfur as indicative of the gold-thiol bond as well as the presence of the TE backbone. Data were collected for S, C and Au. The AES spot size was approximately 50 μm . The only suitable features for analysis on the real devices were the photolithographically defined bonding pads; the largest e-beam written structure was 10 μm wide. The e-beam written structures had the relevant surfaces for assembly, so the e-beam patterning was modified for a test piece. A $200 \times 200 \mu\text{m}^2$ square in the central region of the die replaced the usual $< 10 \mu\text{m}$ lines and small gaps. The process history was the same as that of the real devices. AES results are shown in Figure 4.3.3, and summarized in Table 4.3.2. On the large electron-beam written square, a level of sulfur was detected that was consistent with the pure MLs formed on the fresh gold substrates. On the bonding pads, however, only near noise level S was measured. Also note that while the gold signal was strong on the e-beam written sites, where it had only to escape 30 Å of TE₄S, it was near the noise level (2 At %) on the photolithography sites, consistent with the much thicker PMMA residue overlayer attenuating the signal. The results were consistent with the IR study discussed above.

The processing history of the e-beam written gaps is not inconsistent with the self-assembly of thiol functionalized oligomers. This has been confirmed by ellipsometry, IR spectroscopy, and AES.

	PMMA			Photolithography			
pre-process SAM?			19.5Å				19Å
resist spin	✓	✓	✓	✓	✓	✓	✓
resist liftoff & rinse	10-12Å			✓			
resist bake & strip		100Å	100Å		13-14Å		22Å
resist bake, flood exp, dev						15Å	
post process SAM?	✓	✓		✓	✓	✓	
compatible process?	yes	no	no	yes	yes	yes	yes

Table 4.3.1 Matrix of processing variations tested for effect on ML formation. Each column represents a separate experiment; if the step listed at left was done, there is an entry in the corresponding row. Ellipsometric thicknesses are listed where available. The final conclusion of compatibility with SAM formation is given in the last row.

	At % Au	At % S	At % C
photolith. site, TE4S	2.8	2.6	95
e-beam lith. site, TE4S	5.8	9.2	85.
pure ML, TE4S	7.8	13	79

Table 4.3.2 Results of AES on microfabricated die. Data were taken on 3 equivalent sites; results are representative. The photolithographically defined site is a $100 \times 100 \mu\text{m}^2$ bonding pad, the e-beam defined site is $200 \times 200 \mu\text{m}^2$ square in the central region of the die. AES results for a pure ML of TE4S on clean gold are given for comparison. The AES noise level is ~ 2 At %.

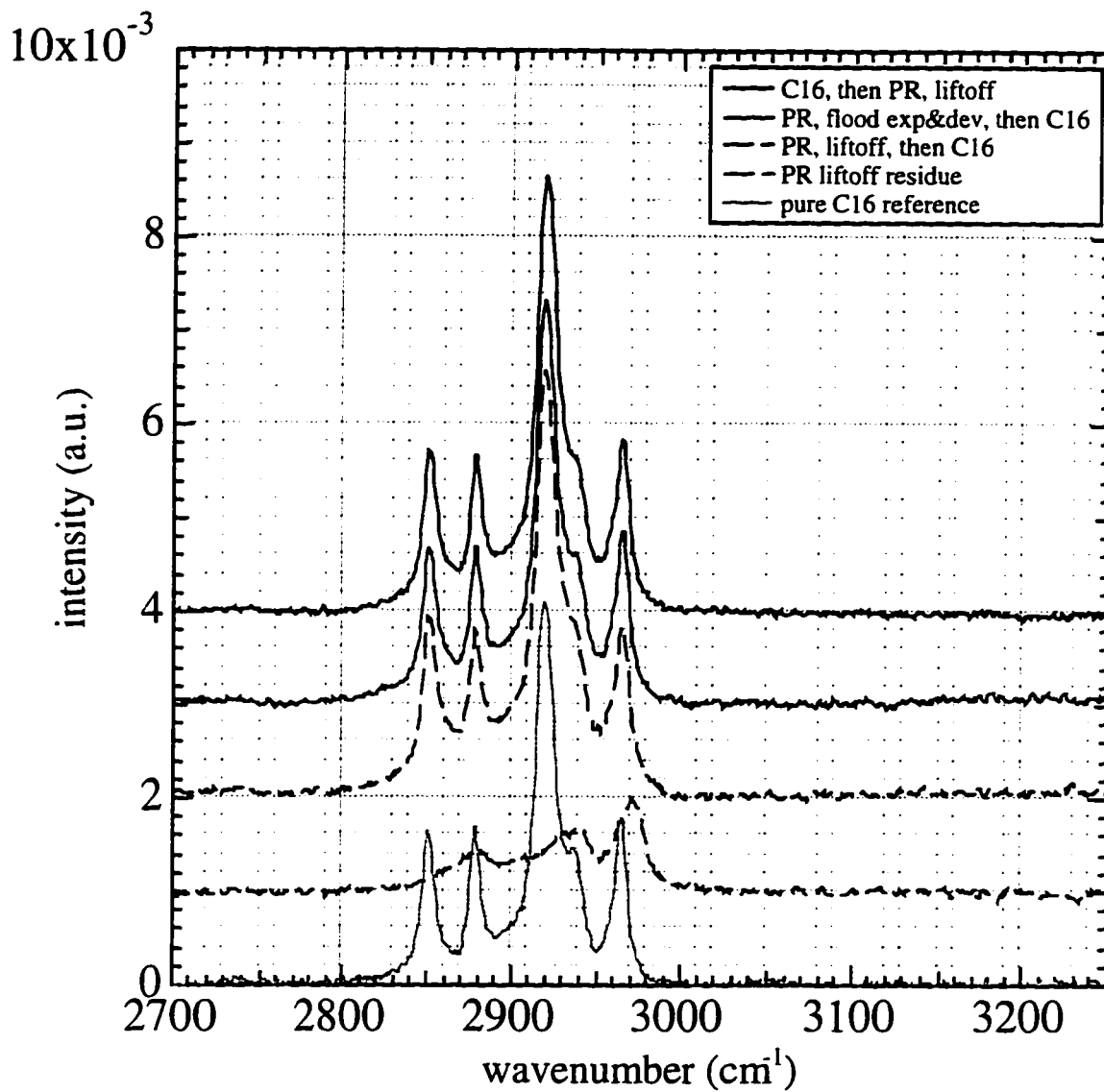


Figure 4.3.1 High frequency region of IR spectra taken on wafers with various exposures to PR and C16. A spectrum from a pure C16 (bottom) and one from PR liftoff residue (second from bottom) are shown for comparison. The wafers processed with PR before C16 SA (2nd, 3rd from top) and after (top) show features characteristic of C16. Spectra are offset by 1×10^{-3} for clarity.

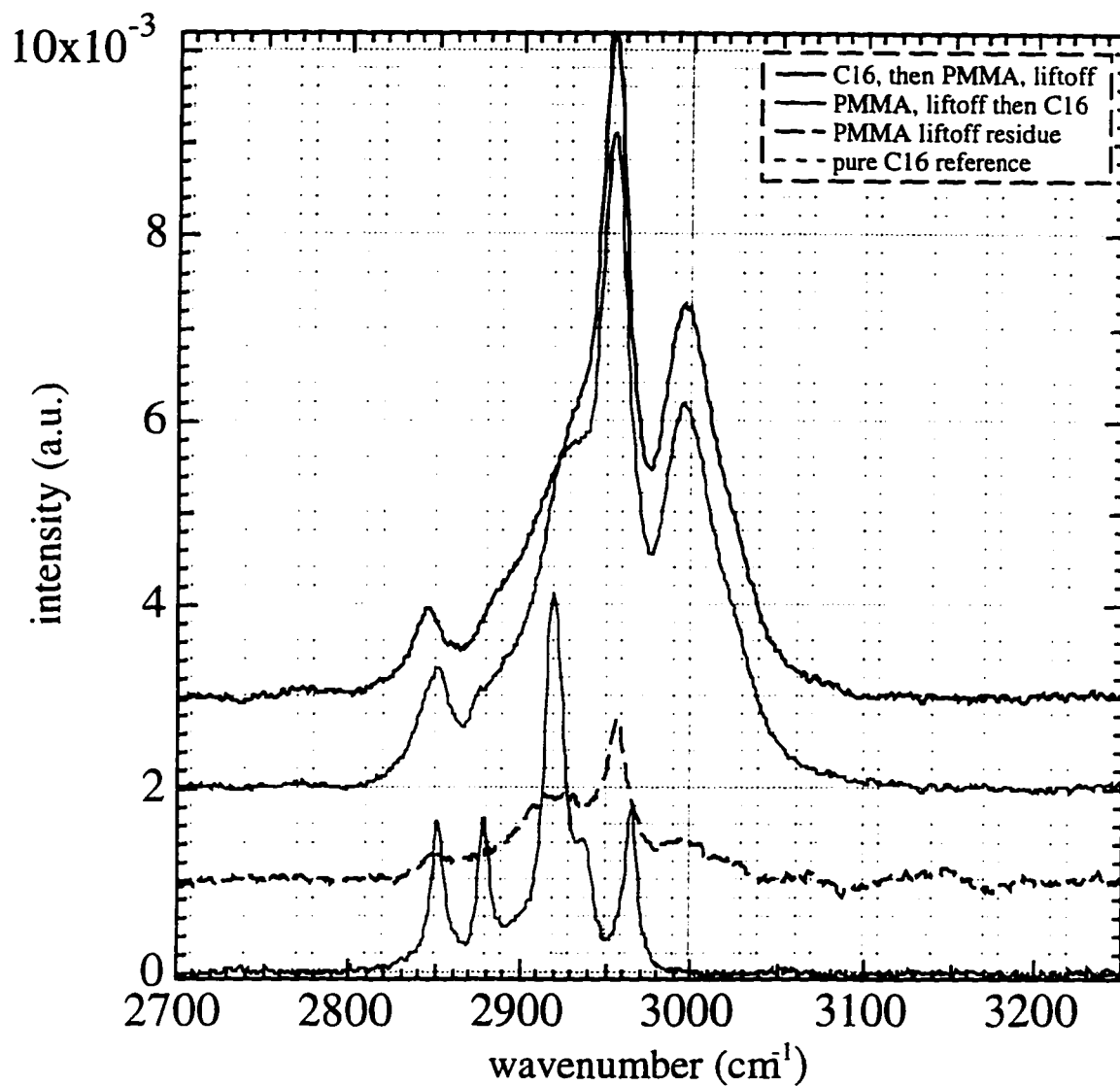


Figure 4.3.2 High frequency IR spectra taken on two wafers with various exposures to PMMA and C16 ML formation. A spectrum from a pure C16 ML (bottom) and one from PMMA liftoff (second from bottom) are shown for comparison. The wafers with C16 before (top) and after (second from top) PMMA bake and liftoff show spectra characteristic of PMMA residue. Spectra are offset by 1e-3 for clarity.

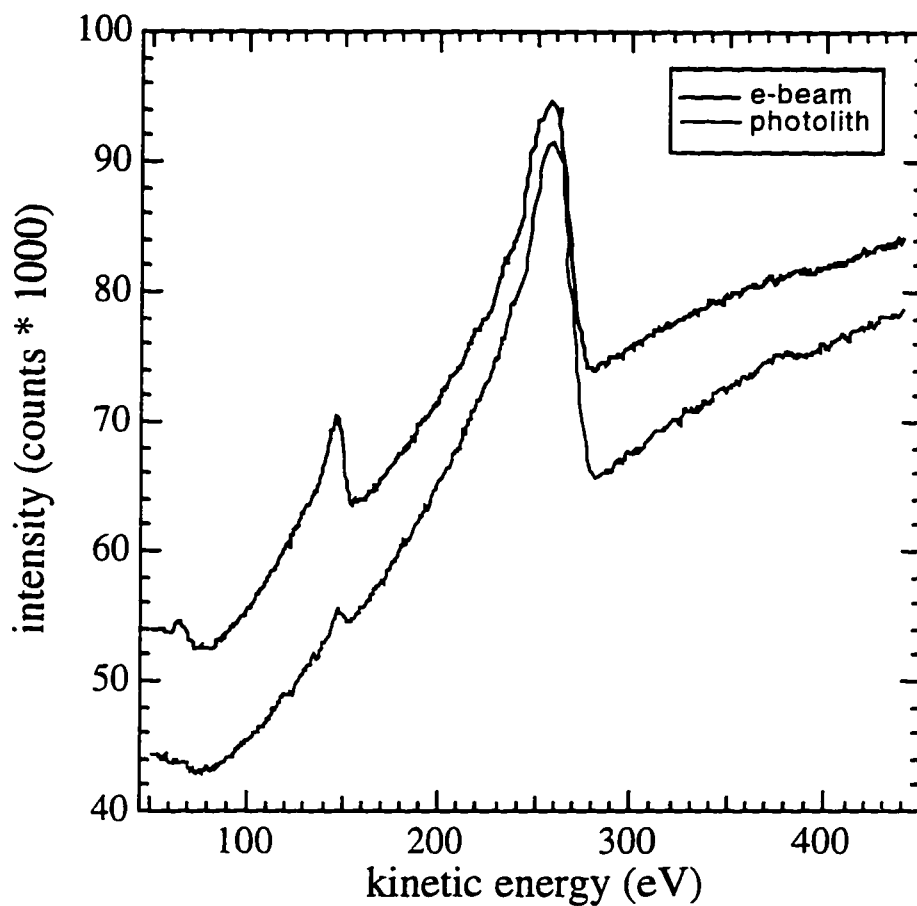


Figure 4.3.3 AES spectra taken on e-beam written (top) and photolithographic (bottom) features after TE4S ML formation. The sulfur peak at 147.50 eV is distinctly higher on the e-beam feature, indicating successful assembly of TE4S. The gold peak at 68 eV is evident in the top (e-beam feature) trace, consistent with the thinner ML on those features.

§ 4.4 Summary and Conclusion

Two fabrication designs for 10 nm gaps have been described in detail. The vertical cleave process has the advantage of flexibility: in electrode and insulator materials choice, gated operation, and insulator thickness. The observed tearing of the gold electrode metal upon cleaving should be addressable; it is the designer's opinion that this process is superior for future work. The planar gaps process has more reliable yield of nanometer-scale gaps – both of the gaps per die, and of dies per substrate. One should be able to independently choose material for each electrode, given the separate angled depositions to create them; there was no point to pursuing this avenue without an established symmetric baseline.

Of more general interest, a surface analysis study was done to establish the compatibility of microfabrication and the gold-thiol self-assembly mechanism. The metal surface exposure to resist liftoff is sufficient to leave a resist residue; this residue is insufficient to inhibit self-assembly of TE4S molecules. The spin and bake process for photolithography leaves 15-20Å of photoresist residue as well, regardless of PR removal process; this residue also did not inhibit the formation of a well-ordered C16 SAM. The only combination tested that left a surface incompatible with self-assembly was the spin and bake cycle of PMMA on metal. Fortunately, this cycle is generally used to define relevant features via e-beam writing and liftoff, as with the planar gaps process.

In summary, a microfabrication process has been developed to reliably produce gold electrodes separated by sub-10 nm gaps on an insulating substrate. The compatibility of the electrode surfaces with Au-S self assembly has been verified.

References

- ¹ Chrome on glass masks for photolithography were fabricated at the National Nanofabrication Facility, Cornell University.
- ² J.J. Hickman, D. Ofer, C. Zou, M.S. Wrighton, P.E. Laibinis, G.M. Whitesides, *J. Am. Chem. Soc.* **113**, 1128-1132 (1991).
- ³ The Merck Index, S. Budavari, M.J. O'Neil, A. Smith, P.E. Heckelman, Eds. (Merck & Co., Rathaway, N.J., 1989), p. 1492.
- ⁴ P.E. Laibinis, G.M. Whitesides, D.L. Allara, Y.T. Tao, A.N. Parikh, R.G. Nuzzo, *J. Am. Chem. Soc.*, **113**, 7152-7167 (1991).
- ⁵ Metals Handbook, (American Society for Metals, Metals Park, Ohio, 1978).
- ⁶ A. Aviram, M. Ratner, *Chem. Phys. Lett.* **29**:277-283 (1974).
- ⁷ For example, orthogonal self-assembly is discussed in: T.J. Gardner, C.D. Frisbie, M.S. Wrighton, *J. Amer. Chem. Soc.*, **117**, 6927-6933 (1995).
- ⁸ L. Strong, G.M. Whitesides, *Langmuir* **4**, 546-558 (1988).
- ⁹ Angled deposition process development by M. Amman.
- ¹⁰ W Chen, H Ahmed, K Nakazoto, *Appl. Phys. Lett.* **66**, 3383-84 (1995).
- ¹¹ See also: A.N. Broers, J.M. Harper, W.W. Molzen, *Appl. Phys. Lett.* **33**, 392 (1978); P.B. Fischer, S.Y. Chou *Appl. Phys. Lett.* **62**, 2989 (1993).
- ¹² G.P. Kittlesen, H.S. White, M.S. Wrighton, *J. Amer. Chem. Soc.* **106**, 7389-7396 (1984).
- ¹³ J.J. Hickman, D. Ofer, C. Zou, M.S. Wrighton, P.E. Laibinis, G.M. Whitesides, *J. Amer. Chem. Soc.* **113**, 1128-1132 (1991).
- ¹⁴ See Chapter 3, Introduction.

Chapter Five. Solution Depositions of Difunctionalized TE Oligomers on Microfabricated Electrodes

As discussed in the Introduction, there are a series of steps which must be accomplished to build a molecular device. In Chapter Two, the theoretical construct for the optimization of the electronic properties of a conjugated oligomer was presented, as was the experimental system used for these experiments. Chapter Three described experiments designed to gain an understanding of the surface assembly properties of these oligomers. The fabrication of small electrodes was described in Chapter Four, with assembly experiments to verify the compatibility of the microfabrication processes with self assembly. The remaining step is the self assembly of difunctionalized oligomers across microfabricated electrodes. Small quantities of two long difunctionalized oligomers were obtained. A series of depositions were performed, all resulting in null electrical results.

In this chapter, the deposition procedure for the difunctionalized 17-mer (STE17S) will be described. The lack of electrical response prompted a number of questions regarding the assembly. The depositions were characterized using Auger electron spectroscopy, Raman spectroscopy and nuclear magnetic resonance, in addition to current-voltage measurements. The results of these analyses prompted the surface experiments described in Chapter Three.

§ 5.1 Solution Deposition of STE17S

Gaps die were diced into single die pieces, a few mm on a side. Die were mounted on 16 pin DIP headers using In metal. The traditional conductive paints and epoxies used to secure die to headers were not suitable for this application; none were impervious to the solvent THF. Aluminum wire bonding made electrical contact between the individual bonding pads on the die and the header leads. Immediately prior to deposition, the leads were clipped, and current-voltage (I-V) measurements were done on all devices to set a baseline. I-Vs were also taken between the electrodes and the substrate to check for leakage paths. All I-Vs were taken with a Hewlett Packard 4145 Semiconductor Parameter Analyzer. Open gaps had a resistance of greater than $10^{12} \Omega$. A switchbox was built to allow testing of the header with any combination of leads shorted, grounded, or open. The switchbox allowed for header insertion inside the switchbox for shielded dry measurements; alternatively, the internal socket could be jumpered to allow for measurement of the header while it was in the deposition cell. The experiment was designed in anticipation of a detectable change in the electrical response of the gap once an oligomer had assembled across it; as soon as a single molecule bridged the gap, the deposition would be stopped. To achieve a single molecule measurement, a dilute solution was to be used.

The first generation deposition cell was a modified Pyrex beaker (see Figure 5.1.1). A teflon insert was machined to include a 16 pin socket in the teflon base. Teflon coated electrical wires were soldered to the bottom of the pins and run out to a 16-pin socket machined in the top of the cell. A ribbon cable mated the deposition cell to the switchbox. A gas inlet and syringe hole were also machined into the top. After a number of depositions, the solder joints, which were submerged in the solution during depositions, showed signs of corrosion. The nature of the corrosion was not determined; there was

concern that the corrosion may contaminate the solution. The cell was redesigned such that only the gold pins of the header socket were in contact with the solution. The second deposition cell was a 2 ounce teflon screwtop container with a 16 pin socket machined into the bottom (see Figure 5.1.2). A gas inlet and syringe hole were machined into the top. After preliminary electrical characterization of the gaps, the header was plugged into the deposition cell and sealed. The cell was purged for 1 hour with argon. Freshly distilled THF was injected into the cell and withdrawn by syringe three times; caution was taken to maintain anaerobic conditions at all stages. A known quantity of THF was injected into the cell.

The difunctionalized 17-mer was delivered in a screwtop vial. The screwcap was replaced with a septum, and the vial was purged with Ar. THF was added to this vial to dissolve all of the oligomer, making a solution of known concentration. Some of this solution was then transferred to the deposition cell by syringe; the rest was evaporated and the remaining oligomer was stored under Ar. NH_4OH was injected directly into the deposition cell to cleave the thioacetate endgroups of the STE17S and allow for self assembly. An overpressure of Ar was maintained in the cell for the duration of the deposition. The deposition continued for 5 days. The same solution was used for a sequential deposition. A second header was electrically characterized, inserted into a second deposition cell, and triple rinsed *in situ* with THF after extensive Ar purging. The deposition solution was transferred by syringe from the first deposition cell to the second. Again, caution was taken to maintain anaerobic conditions at every stage. At the end of the depositions, the gaps showed no change in electrical properties.

The following issues were raised by this null result: Were the oligomers present in solution, and in tact? Were they assembling to the surfaces? If not, were they linking up due to oxidation, which may prevent them from assembling? Was the solution contaminated in some manner that would prevent assembly? After 3 and 7 days, an aliquot

of solution was extracted for analysis by Raman spectroscopy and NMR. The solutions were treated with HCl to stabilize the thiolates. For the NMR samples, the THF was blown off, and the oligomer was resolvated with chloroform. The oligomer and solution integrity were verified by NMR. The treated solution (still in THF) was concentrated and sealed in capillary tubes for Raman analysis. The disulfide that would form if the oligomers were oxidized has a strong Raman signal. No disulfide was detected by Raman (see Figure 5.1.3). To verify assembly, pieces of patterned substrate were included in the deposition cell. Samples were removed from solution after 4 and 7 days, and sent for AES analysis. Separate scans were taken on the photolithographically defined bonding pads and on the SiO₂ (see Figure 5.1.4). No sulfur was detected on the oxide; very low levels of sulfur were detected on the gold pads, inconsistent with the formation of an STE17S monolayer. We now understand this result in terms of the processing history of the bonding pads leading to a resist residue that inhibited self assembly (see §4.3). This result prompted the extensive surface assembly experiments described in Chapter Three.

Figure 5.1.5 shows the behavior of current for the gaps at an applied voltage of 1 V as a function of time in solution with the oligomer and NH₄OH. For all gaps, the current dropped substantially as a function of time in solution. The control experiment performed on a gaps header in THF is also presented. Baseline measurements with gaps in THF established a solution resistance of a few hundred MΩ. Measurement of the gaps in THF shows slight variation of current in time— ±10% the original value. The 50% decrease in current for the gaps in oligomer solution may be attributed to the STE17S assembling on the electrode surfaces and inhibiting current flow. The assembly time may be estimated as reaching a steady state in 6 hours.

Maintaining a potential across the gaps during assembly may affect the assembly. There is evidence that alkanethiols on Au desorb in alkaline solutions; thinner, less dense films are predicted to desorb at less negative potentials. Our deposition solution is alkaline

from the NH_4OH ; based on the ML results discussed in Chapter Three, the STE17S are expected to form thin, loosely packed ML's. Other depositions done without an applied potential also resulted in no change of the gaps' electrical characteristics.

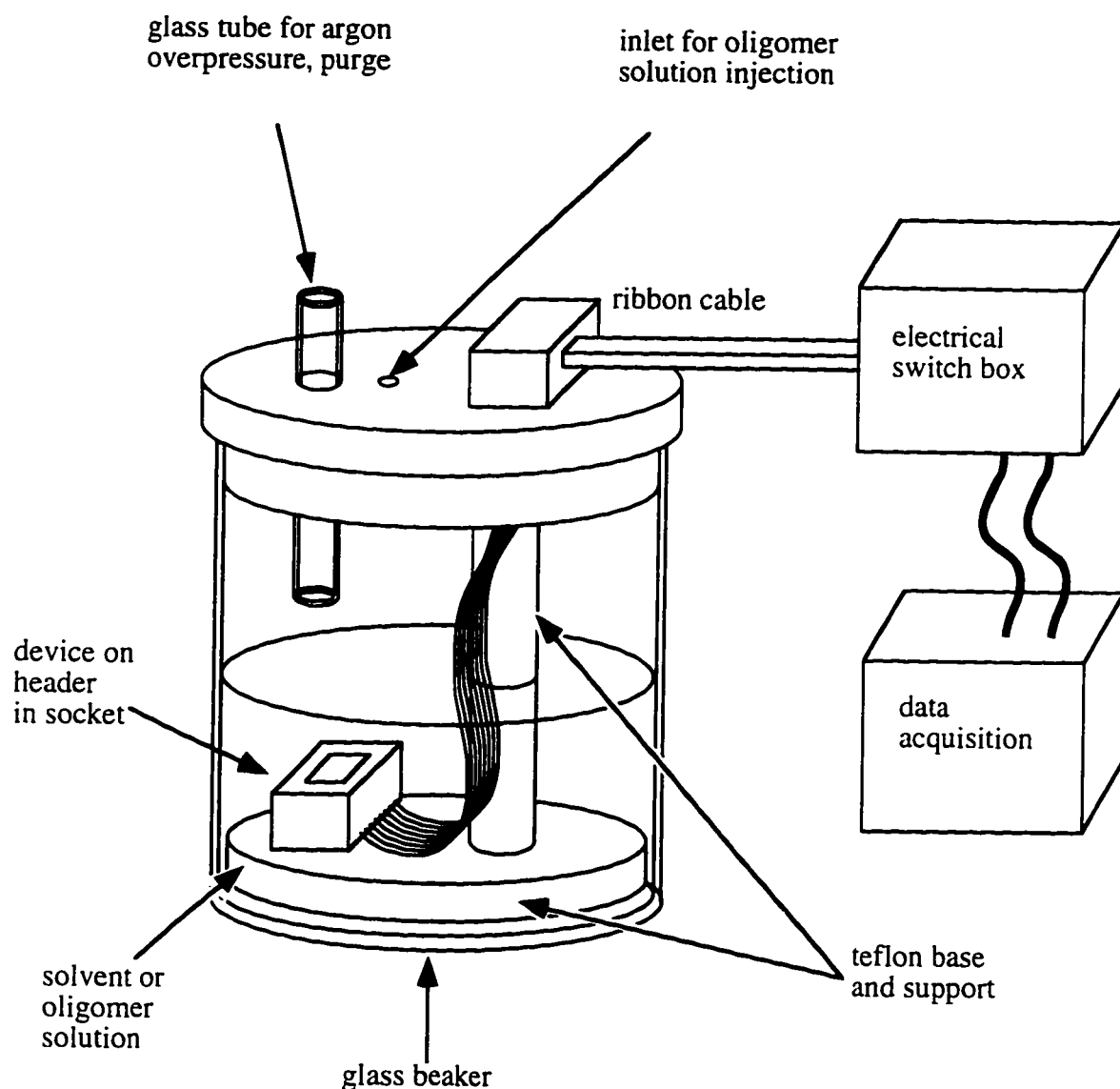


Figure 5.1.1 Original deposition cell for solution measurements. A teflon insert was machined to seat the 16-pin DIP socket. Teflon coated wires ran from the bottom of the teflon base up to the teflon top. The signal was taken from the deposition cell to the switchbox. This design was discontinued due to contamination at the solder joints in the teflon base.

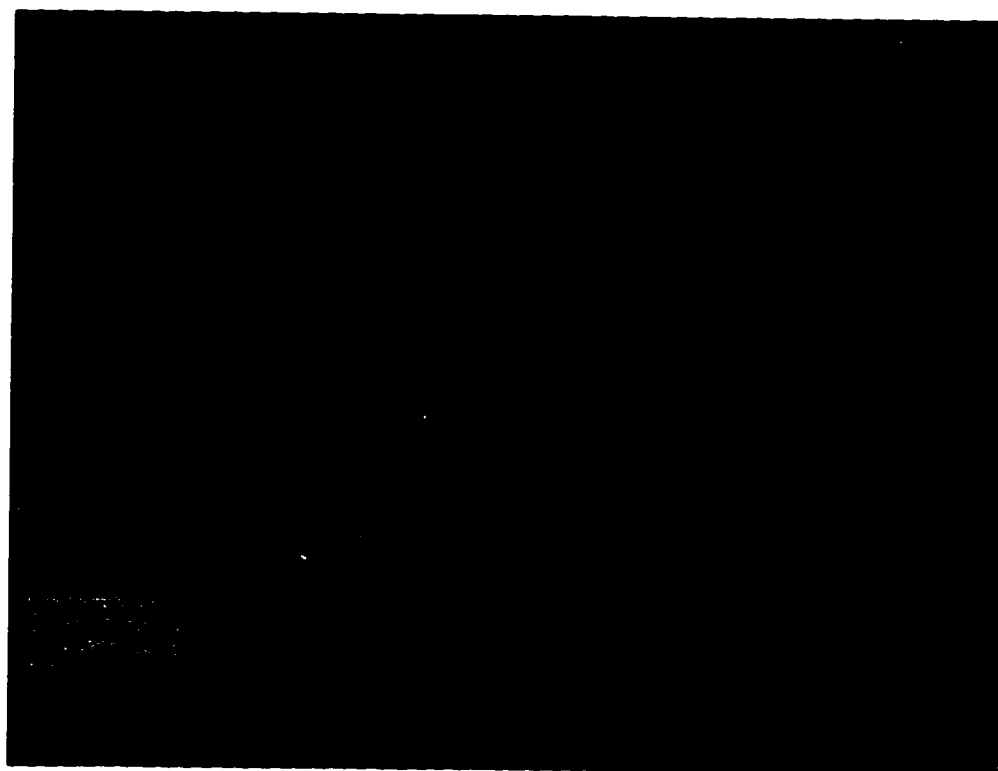


Figure 5.1.2 Final version of the deposition cell used for oligomer depositions. All wiring was removed from contact with the solution. These containers were particularly designed for aggressive solvents.

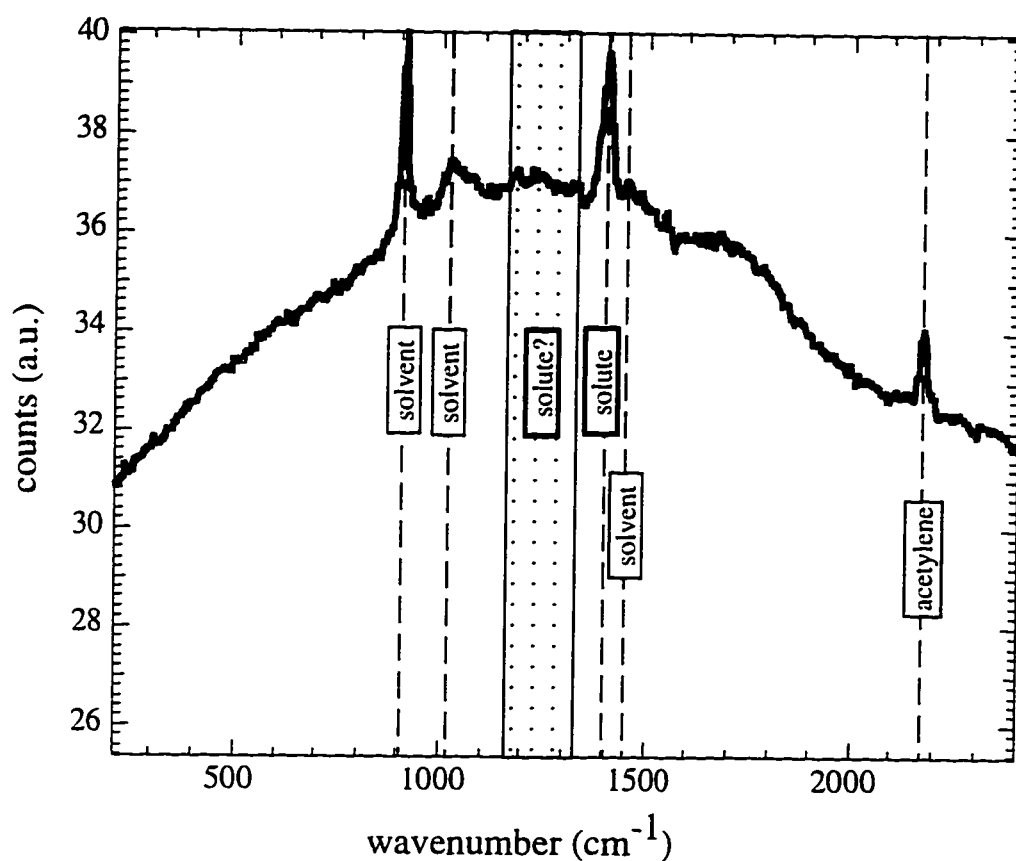


Figure 5.1.3 Results of Raman analysis on solution after 7 days. Peaks characteristic of THF were present, as well as vibrations associated with the thiophene and acetylene of the backbone. The disulfide stretch at 500 cm⁻¹ was not evident, indicating that precautions to maintain anaerobic conditions during the deposition were successful in preventing polymerization of the oligomer.

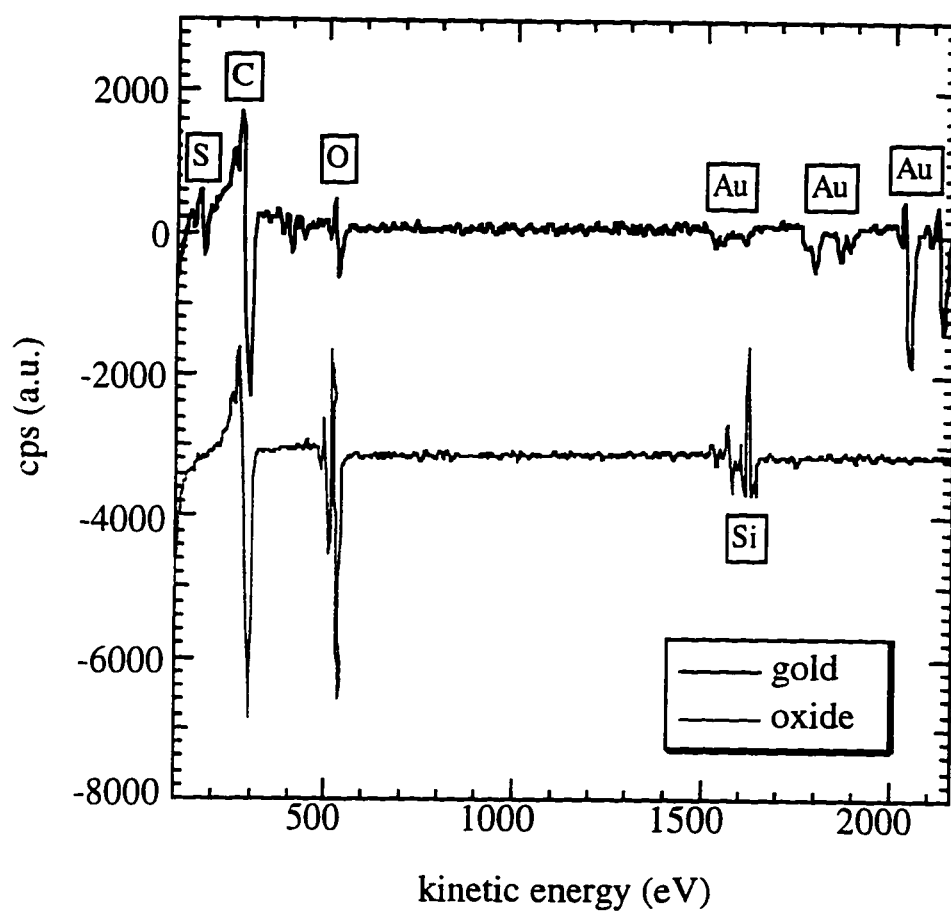


Figure 5.1.4 Results of AES analysis on die pattern after 7 days in solution. Data were taken on the gold photolithographic pattern and on the oxide. S was not detectable on oxide, confirming the selectivity of the self-assembly. Less than 1 atomic percent S detected on gold, consistent with the results described in Chapter Four regarding the resist residue left on these structures. Those results were not known at the time of this deposition.

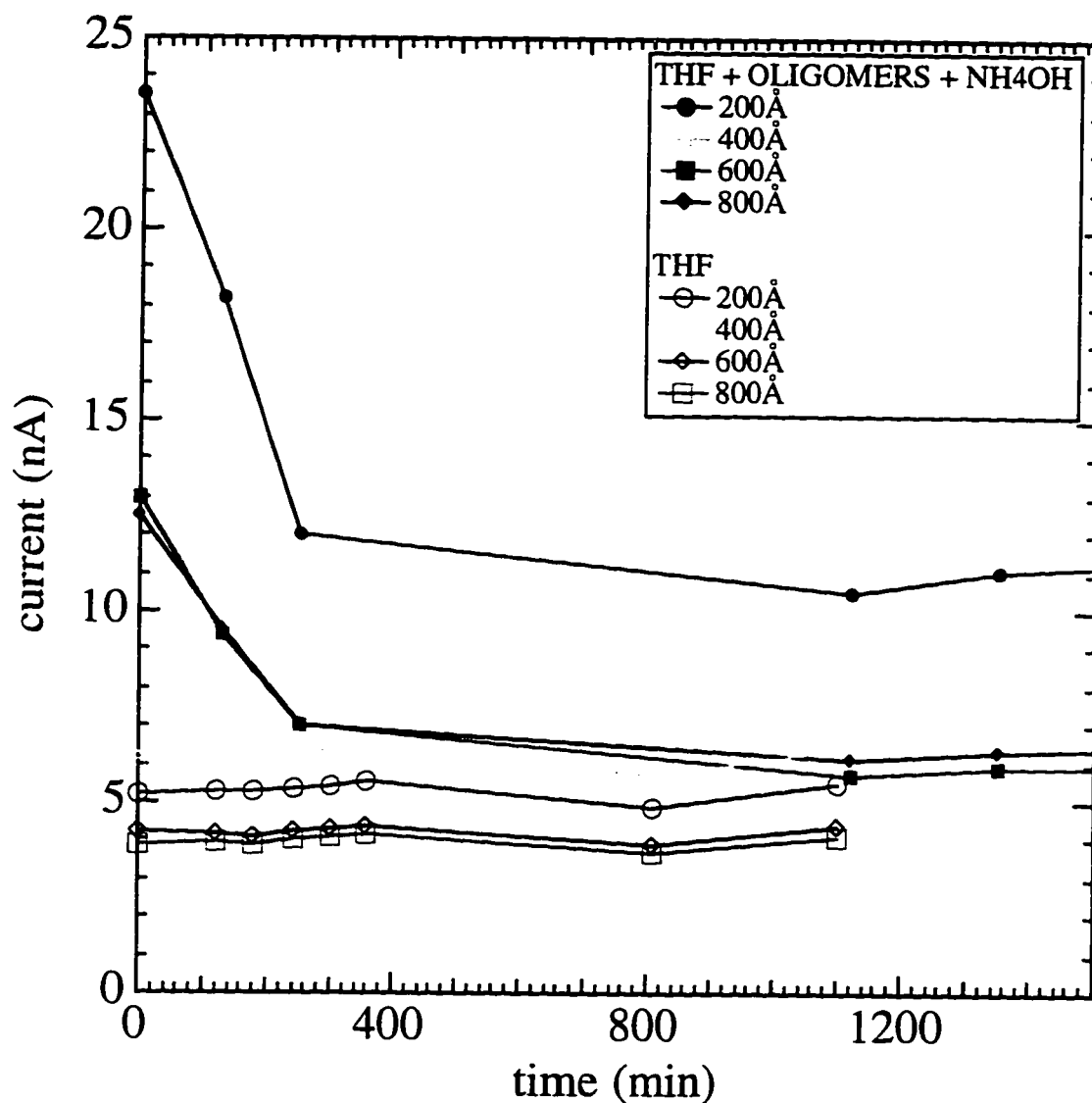


Figure 5.1.5 Current at 1 V applied potential as a function of time is shown for a series of gaps in solution with THF + difunctionalized 17-mer + NH_4OH (solid markers). The current decreases sharply in the first 4-5 hours for all gaps, then plateaus at a value approximately 50% its original value. The same experiment was done on a series of gaps in THF (open markers). The current does not change substantially for the gaps in THF alone.

§ 5.2 Summary and Conclusion

Preliminary solution measurements of oligomer depositions on electrodes were described. Contamination concerns resulted in the redesign of the deposition cell to exclude all materials from solution contact, including teflon coated wires and solder joints. The depositions were characterized by AES, Raman, NMR and current-voltage measurements. Solution background currents were 4-6 nA at 1 V for the various gaps, corresponding to a solvent resistance of a few hundred $M\Omega$. The electrochemistry was not more fully explored at this time because the analyses of the oligomer depositions indicated problems with the self assembly; efforts were directed toward that area.

Reference

¹ M.M. Walczak, D.D. Popenoe, R.S. Deinhammer, B.D. Lamp, C. Chung, M.D. Porter. *Lang.* **7**, 2687-93 (1991).

Chapter Six. Conclusion

This thesis describes the quest for an electronic device where the active element is a single, isolated organic polymer chain. The following stages were identified as necessary to implement this experiment: synthesis and characterization of highly specialized molecules; oriented arrangement of single functional molecules; coupling and attachment of a molecule to the macroscopic world; and electrically addressing a single molecule. The conclusions from each of these stages will now be reviewed.

In Chapter Two, the source of conjugation in polymeric systems was reviewed, and the effects of monomer and substituents on the electronic properties of the polymer were described. The VEH pseudopotential method was used to predict the electronic properties of the experimental system, α,ω -phenylthioacetate, ethyl β -substituted thiophene ethynylenes. A number of characteristics of the system were inconsistent with optimum electronic performance: the backbone wavefunction is not delocalized over the endgroup; $E_{\text{max}}=2.6$ eV, characterizing the system as an intrinsic semiconductor; attempts to dope TE oligomers have yielded no noticeable change in conductivity; the experimentally determined bandwidth is 0.8 eV, indicative of poor mobility even if the chain were to be ionized. Despite the improbability of conductivity in these systems, their self assembly properties were examined for application to a more appropriate system in the future.

The surface assembly properties of the thiophene ethynylene oligomers to a gold surface were studied by ellipsometry, GAIR, AES, and XPS, as described in Chapter Three. The TE systems studied are susceptible to a variety of competing assembly

mechanisms: the unfunctionalized oligomers strongly adsorb to gold, apparently through the thiophene; the phenylthioacetate-terminated molecules seem to self assemble via a different mechanism than the phenylthiols. Some oligomers may be self assembling via the backbone despite the presence of the endgroup. It is not clear what role the long rigid rod nature of the backbone plays independent of the thiophene interaction.

Two fabrication designs for 10 nm gaps were described in Chapter Four. The vertical cleave process has the advantage of flexibility: in electrode and insulator materials choice, gated operation, and insulator thickness. The planar gaps process has more reliable yield of nanometer-scale gaps – both of the gaps per die, and of dies per substrate. One should be able to independently choose material for each electrode, given the separate angled depositions to create them. The compatibility of the electrode surfaces with the Au-S self assembly process was verified.

Preliminary solution measurements of oligomer depositions on electrodes were described in Chapter Five. The depositions were characterized by AES, Raman, NMR and current-voltage measurements. Initial electrical characterization indicated no measurable change in the gap properties before and after deposition, although during the depositions, the resistance of the gaps increased while in solution. The electrochemistry was not more fully explored at this time because the analyses of the oligomer depositions indicated problems with the self assembly; efforts were directed toward that area.

Current cross-disciplinary work of interest to the fabrication engineer includes the use of self assembled monolayers to engineer interface¹ and surface properties.² It would be advantageous, from a microfabrication perspective, to have thermodynamics working for the engineer. In related work, polymer devices are being made by electropolymerizing across prefabricated microelectrodes.³ The resulting structure is still a bulk device.

although the polymerization has been pushed toward the single chain limit.⁴ Another approach is to functionalize small gaps, and put gold clusters in the gaps⁵ for electronic characterization.

Perhaps the most potent application for the infrastructure developed here is in the area of biological and chemical sensors.⁶ It is the author's opinion that organic systems are not well suited to compete with crystalline solids on the grounds of transport alone. The true potential for molecules in electronics lies in their compatibility with biological systems. Patterned self assembled monolayers have been applied to the selective surface attachment of cells and proteins. Such control may be useful for drug screening and genetic or tissue engineering.⁷ A conjugated polymer, PDA, has been synthesized with enzyme ligands. This molecule has been applied to the detection of viruses.⁸ In future applications, the enzyme ligands could be hormonal and immunoreceptors for assessing the toxicity of environmental pollutants. Molecular electronics becomes useful in this arena when the changes induced by a molecular recognition event produce an electron transfer reaction that can be detected.

This project is inherently multi- and interdisciplinary. I have tried to present the chemistry in comprehensible terms to the physicists and engineers, and the physics in intuitive terms for all. Science is, after all, just science— regardless of the language. The critical element to understanding all of the science here is finding the electrons, and evaluating whether they'll share nicely with their neighbors. Organic synthetic chemistry, involved in making the polymer systems, must be appreciated for its variable parameters and its time-intensive process of realizing a design. Synthetic strategies are designed around which element wants electrons more. Quantum chemistry provides the tool to model and interpret the electronic behavior of the various systems, and provides the understanding to iterate on the designs wisely. The transport properties discussed in

Chapter Two basically rely on electron sharing. Surface chemistry experiments study how to selectively assemble these molecules on a surface. The self assembly discussed in Chapter Three relies on electron sharing. The researcher need not become an expert synthetic chemist, or quantum chemistry theorist; she needs only to overcome the language barrier enough to appreciate the issues of the field: why is a 17-mer with an unsubstituted thiophene not desirable? how can a thioacetate be cleaved *in situ* without compromising the integrity of the microfabricated devices? The true advances in molecular electronics will arise from the work of those curious and eager souls willing to communicate in the relevant tongues. The inter- and multidisciplinary parts of this work have been the most challenging and, as one may suspect, the most rewarding. They are also the most essential for the advance of this technology.

References

- ¹ O.S. Nakagawa, S. Ashok, C.W. Sheen, J. Martensson, D.L. Allara, *Jap. J. Appl. Phys.* **30**, 3759 (1991); C.W. Sheen, J.-X. Shi, J. Martensson, A.N. Parikh, D.L. Allara, *J. Amer. Chem. Soc.* **114**, 1514-1515 (1992).
- ² P.E. Laibinis, G.M. Whitesides, D.L. Allara, Y.T. Tao, A.N. Parikh, R.G. Nuzzo, *J. Amer. Chem. Soc.* **113**, 7152-7167 (1991); P.E. Laibinis, G.M. Whitesides, *J. Amer. Chem. Soc.* **114**, 9022-9028 (1991).
- ³ G.P. Kittleson, H.S. White, M.S. Wrighton, *J. Amer. Chem. Soc.* **106**, 7389-7396 (1984).
- ⁴ C.L. Curtis, J.E. Ritchie, M.J. Sailor, *Science* **262**, 2014-2016 (1993).
- ⁵ We return to the 'great luck' method of fabrication mentioned in Chapter One: D.L. Klein, P.L. McEuen, J.E. Bowen Katari, R. Roth, A.P. Alivisatos, *Appl. Phys. Lett.* **68**, 2574-74 (1996).
- ⁶ D.H. Freedman, *Science* **254**, 1308-1310 (1991); J.S. Schultz, *Sci. Am.* (August, 1991) p.64-69.
- ⁷ R. Singhvi, A. Kumar, G.P. Lopez, G.N. Stephanopoulos, D.I.C. Wang, G.M. Whitesides, D.E. Ingbar, *Science* **264**, 696-698 (1994).
- ⁸ D.H. Charych, J.O. Nagy, W. Spevak, M.D. Bednarski, *Science* **261**, 585 (1993).